

**ANALYTICAL AND EXPERIMENTAL INVESTIGATION
OF AN EFFICIENT VISCOUS PUMP**

A THESIS

Presented to

The Academic Faculty

by

Marlene Elise Mainland

In Partial Fulfillment of the

Requirements for the Degree

Master of Science in Mechanical Engineering

Georgia Institute of Technology

June, 1990

19981202 044

REPORT DOCUMENTATION PAGE

AFRL-SR-BL-TR-98-

Public reporting burden for this collection of information is estimated to average 1 hour per response, including the time for reviewing the collection of information, sending comments and maintaining the data needed, and completing and reviewing the collection of information. Send comments regarding this burden estimate or any other aspect of this collection of information, including suggestions for reducing this burden, to Washington Headquarters Services, Directorate for Information Operations and Reports, 1204, Arlington, VA 22202-4302, and to the Office of Management and Budget, Paperwork Reduction Project (0704-

ring
n of
uite

1. AGENCY USE ONLY (Leave Blank)	2. REPORT DATE June 1990	3. REPORT TYPE AND DATES COVERED Final	
4. TITLE AND SUBTITLE Analytical and Experimental Investigation of an Efficient Viscous Pump		5. FUNDING NUMBERS	
6. AUTHORS Marlene Elise Mainland			
7. PERFORMING ORGANIZATION NAME(S) AND ADDRESS(ES) Georgia Institute of Technology		8. PERFORMING ORGANIZATION REPORT NUMBER	
9. SPONSORING/MONITORING AGENCY NAME(S) AND ADDRESS(ES) AFOSR/NI 4040 Fairfax Dr, Suite 500 Arlington, VA 22203-1613		10. SPONSORING/MONITORING AGENCY REPORT NUMBER	
11. SUPPLEMENTARY NOTES			
12a. DISTRIBUTION AVAILABILITY STATEMENT Approved for Public Release		12b. DISTRIBUTION CODE	
13. ABSTRACT (Maximum 200 words) See attachment			
14. SUBJECT TERMS		15. NUMBER OF PAGES	
		16. PRICE CODE	
17. SECURITY CLASSIFICATION OF REPORT Unclassified	18. SECURITY CLASSIFICATION OF THIS PAGE Unclassified	19. SECURITY CLASSIFICATION OF ABSTRACT Unclassified	20. LIMITATION OF ABSTRACT UL

**ANALYTICAL AND EXPERIMENTAL INVESTIGATION
OF AN EFFICIENT VISCOUS PUMP**

Approved:

Dr. Itzhak Green
Chairman

Dr. Izhak Etsion

Dr. Gene Colwell

Dr. Don Giddens

Date Approved By Chairman

ACKNOWLEDGEMENTS

I would like to take this opportunity to express my deepest appreciation for my adviser, Dr. Itzhak Green. Doing research under his guidance has been enjoyable and rewarding. His interest and faith in the project have been a great source of motivation for me. Also, I wish to thank Dr. Izhak Etsion for his special interest in the project and Dr. Gene Colwell and Dr. Don Giddens for being on my reading committee. I would like to thank Gilad Peleg, a visiting scholar from Israel, for his work designing the pump and Ariel Trau for filling in after Gilad. A special thanks goes to Scott Bair for all his help (and patience) in the lab.

This project was supported in part by a Georgia Tech Foundation Grant, E25-549, made by Mr. Gilbert Bachman. This support is gratefully acknowledged. The Department of Defense has supported in part my graduate studies through the National Defense Science and Engineering Graduate Fellowship Program and I would like to recognize the Air Force for sponsoring my fellowship.

Most of all, I would like to thank my parents, Keith and Sandy Mainland, for their constant support and confidence in me. They're the greatest. I would also like to thank the rest of my family for their encouragement. To Randy, there are so many things to say, so I'll just say 'come camping in a cornfield' and hope he knows the rest. Thanks goes to Lisa, for her insanity supply, and Paula, for 24 years. Also, I would like to thank my roommates, Doe and Barb, for supplying entertaining distractions, Mike, for being weird³, and the tribo group, for their support.

TABLE OF CONTENTS

ACKNOWLEDGEMENTS	ii
LIST OF TABLES	vi
LIST OF FIGURES	vii
NOMENCLATURE	xi
SUMMARY	xiv
CHAPTERS	
I INTRODUCTION	1
II LITERATURE SURVEY	7
2.1 Recommendations	10
III ANALYSIS	12
3.1 Introduction	12
3.2 Semicircular Lobe Design	14
3.2.1 Semicircular Lobe Analysis	14
3.2.2 Semicircular Lobe Optimization	20
3.3 Straight Lobes	25
3.3.1 Introduction	25
3.3.2 Symmetric V-lobe Design	28
3.3.2.1 Symmetric V-lobe Analysis	28
3.3.2.2 Symmetric V-lobe Optimization	31

	iv
3.3.3 Nonsymmetric V-lobe Design	34
3.3.3.1 Nonsymmetric V-lobe Analysis	34
3.3.3.2 Nonsymmetric V-lobe Optimization	36
3.3.4 Verification of Analysis Using Shape Factors	39
3.3.5 Verification of Analysis Using Finite Element Method	44
3.4 Comparison of Lobe Designs	56
3.4.1 Complete Optimal Case	56
3.4.2 Practical Optimal Case	60
3.4.3 Pumping Performance Based on Experiment Conditions	61
IV EXPERIMENT SETUP	68
4.1 Equipment and Apparatus	68
4.1.1 Calibrations	73
4.2 Procedure	75
V RESULTS AND DISCUSSION	79
5.1 Experimental Results with Comparison to Theory	79
5.1.1 Investigation of Theoretical Models	87
5.1.2 Investigation of Experimental Conditions	97
5.1.2.1 Occurrences in Experiment Not Accounted For in Theory	100

VI CONCLUSIONS AND RECOMMENDATIONS	103
APPENDICES	
A Derivation of Straight Lobe Flow Equations	108
A.1 Symmetric V-lobe	108
A.2 Nonsymmetric V-lobe	113
B Shape Factors	117
C FEM Code	126
BIBLIOGRAPHY	133

LIST OF TABLES

Table 1	Semicircular Lobe Optimization Results	24
Table 2	Symmetric V-lobe Optimization Results	33
Table 3	Nonsymmetric V-lobe Optimization Results	37
Table 4	Comparison of Equations to FEM Model (Poiseuille Flow)	53
Table 5	Comparison of FEM Models ($FEM_{p=0}$ and $FEM_{\partial p / \partial s = \text{constant}}$)	56
Table 6	Optimal Pumping Comparison For Complete Optimal Case	59
Table 7	Optimal Pumping Comparison For Practical Exit Hole Size	62
Table 8	Properties of Shell Tellus 10 Mineral Oil	75
Table 9	Maximum Operating Conditions Parameter (S'_{\max}) Achieved During Experiments	83
Table 10	Clearance Variations At Specified Test Conditions	98
Table 11	Comparison of Bounds To Approximate Actual Value (Literature) For Corner Geometry	123
Table 12	Comparison of Bounds To FEM Model for V-lobe Geometry	125

LIST OF FIGURES

Figure 1 Stator of Semicircular Lobe Viscous Pump	1
Figure 2 Three Dimensional View of a Lobe	2
Figure 3 Straight Lobe Designs (a) Symmetric V-lobe (b) Nonsymmetric V-lobe	6
Figure 4 Fluid Film Described By Reynolds Equation	13
Figure 5 Eccentric Mechanical Face Seal	15
Figure 6 Geometric Variable Definitions For Semicircular Lobe Design	17
Figure 7 Optimal Pumping For Various Number of Lobes at Given Operating Conditions	23
Figure 8 Graphical Comparison of Lobe Designs (a) Symmetric V-lobe Versus Semicircular Lobe (b) Nonsymmetric V-lobe Versus Symmetric V-lobe	26
Figure 9 Geometric Variable Definitions For Symmetric V-lobe Design	29
Figure 10 Geometric Variable Definitions For Nonsymmetric V-lobe Design	34
Figure 11 Generic V-lobe Geometry For Shape Factors (a) Upper Bound (b) Lower Bound	41
Figure 12 Comparison of Flow Predicted By Bounds To Flow Predicted By Analysis (Equation (39))	43

Figure 13	Geometric Approximation of Lobe Leg Ends	44
Figure 14	Natural Area Coordinates For Finite Element Formulation	48
Figure 15	Boundary Conditions For FEM Model	50
Figure 16	Boundaries Corresponding to Nodal Flows	51
Figure 17	Typical Mesh Generated For V-lobe Geometry By ANSYS	52
Figure 18	Comparison of Theoretical Pumping Capacities For Semicircular Lobe and V-lobe (Test Conditions, 8 μm)	65
Figure 19	Comparison of Theoretical Pumping Capacities For Semicircular Lobe and V-lobe (Test Conditions, 12 μm)	66
Figure 20	Comparison of Theoretical Pumping Capacities For Semicircular Lobe and V-lobe (Test Conditions, 16 μm)	67
Figure 21	Pump Assembly	69
Figure 22	Front View of Stator	70
Figure 23	Test Rig	72
Figure 24	Experimental Results With Comparison to Theory (1800 rpm, 8μm)	80
Figure 25	Experiment Results With Comparison to Theory (1200 rpm, 12μm)	81

Figure 26 Experiment Results With Comparison to Theory (600 rpm, 16 μ m)	82
Figure 27 Semicircular Lobe: Experimental and Theoretical Results For Varying Clearance and Constant Speed	85
Figure 28 V-lobe: Experimental and Theoretical Results For Varying Clearance and Constant Speed	86
Figure 29 Semicircular Lobe: Experimental and Theoretical Results For Two Temperatures	88
Figure 30 V-lobe: Experimental and Theoretical Results For Two Temperatures	88
Figure 31 Three Analytical Models Compared to Experimental Results (1800 rpm, 8 μ m)	90
Figure 32 Three Analytical Models Compared to Experimental Results (1200 rpm, 12 μ m)	91
Figure 33 Three Analytical Models Compared to Experimental Results (600 rpm, 16 μ m)	92
Figure 34 FEM _{p=0} Model Compared To V-lobe Experimental Results (8 μ m)	94
Figure 35 FEM _{p=0} Model Compared To V-lobe Experimental Results (12 μ m)	95

Figure 36 FEM _{p=0} Model Compared To V-lobe Experimental Results (16 μm)	96
Figure 37 Typical Clearances at Various Stator Locations	99
Figure 38 Symmetric V-lobe Geometry	108
Figure 39 Nonsymmetric V-lobe Geometry	113
Figure 40 Electrical Circuits For Determining Current Bounds	118
Figure 41 Heat Transfer Analogy of Electric Circuits	119
Figure 42 Simple Geometry For Calculating Shape Factors (a) Isotherms - Upper Bound (b) Insulated Strips - Lower Bound	120
Figure 43 Corner Geometry For Calculating Shape Factors (a) Isotherms - Upper Bound (b) Insulated Strips - Lower Bound	122

NOMENCLATURE

Generalized Notation

(a,b,c)	- Natural area coordinates
c	- Small clearance between rotor and stator
C	- Large clearance between rotor and stator
D	- Width dimension for various geometries
F	- Element loading vector
h	- Fluid film thickness (clearance)
k	- Element stiffness matrix
L	- Length dimension for various geometries
p	- Pressure
q	- Flow per unit length
Q	- Dimensional volumetric flow
Q'	- Dimensionless volumetric flow
R	- Radial coordinate measured from stator center
r	- General radial coordinate
Δr	- Dimensional semicircular lobe thickness
s	- Lobe step height, C-c
	- General path coordinate

S - Shape factor

S' - Operating Conditions Parameter , $\frac{\pi}{12} \frac{P}{\mu \omega} \left(\frac{c}{R_o} \right)^2$

Greek Letters

α - Variable lobe angle

β - Lobe angle determined by number of lobes

δ - Dimensional V-lobe thickness

λ - Geometry ratio for shape factors (b/a)

μ - Absolute viscosity of fluid

ξ - Dimensionless lobe thickness, $\Delta r/R_o$ or δ/R_o

ρ - Density of fluid

σ - Dimensionless step height, s/c

ω - Angular velocity of rotor

Subscripts

c0 - Refers to zero clearance case

e - Element

i - Inner

l - Lower

o - Outer

- p - Pressure induced (Poiseuille)
- s - Shear induced (Couette)
- u - Upper
- x - X-direction
- y - Y-direction
- ,x - Partial derivative with respect to x
- ,y - Partial derivative with respect to y

SUMMARY

A viscous pump design is developed and investigated which is more efficient than a viscous pump previously introduced (Etsion and Yaier, 1988). The key to the new design is straight lobes (V-lobes) as opposed to the semicircular lobes of the previous design. The straight lobe analysis, unlike the semicircular lobe analysis, does not produce a closed form solution. Approximations are made that are verified using shape factors and finite element models. Based on the analyses, the lobe geometry for each lobe design is optimized to produce maximum pumping capacity. The results of the analyses and optimizations, which are based on ideal boundary conditions, show that the straight lobe pump is theoretically superior to the semicircular lobe pump.

A test rig was devised to test the semicircular lobe and the V-lobe design using a real time data acquisition system. The results of the experiments prove that the V-lobe is superior to the semicircular lobe. The experimental results showed good agreement with the analytical predictions, though some deviations were experienced at relatively low flow rates and high pressures. The deviations were attributed to the fact that the test pump did not have the ideal boundary conditions on which the analysis and optimization were based. Alternate boundary conditions were investigated using finite element models which better described the boundary conditions in the test pump. The analysis based on the new boundary conditions more appropriate to the test pump show excellent agreement with the experimental results.

CHAPTER I

INTRODUCTION

A new concept viscous pump was first introduced by Etsion and Yaier (1988). In this pump, the rotor and stator are circular disks separated by the process fluid. Specially designed circular lobes, shown in Figure 1, protrude from the surface of the stator and make a small gap, c , and a larger gap, C , with the flat rotor disk. The gaps C and c are in the order of microns. To help visualize the lobes, an exaggerated three dimensional view of a lobe is shown in Figure 2. The fluid is sheared by the rotor and is dragged by viscous forces in a circumferential direction with the rotor. Because of the clearance difference between C and c , the lobes direct

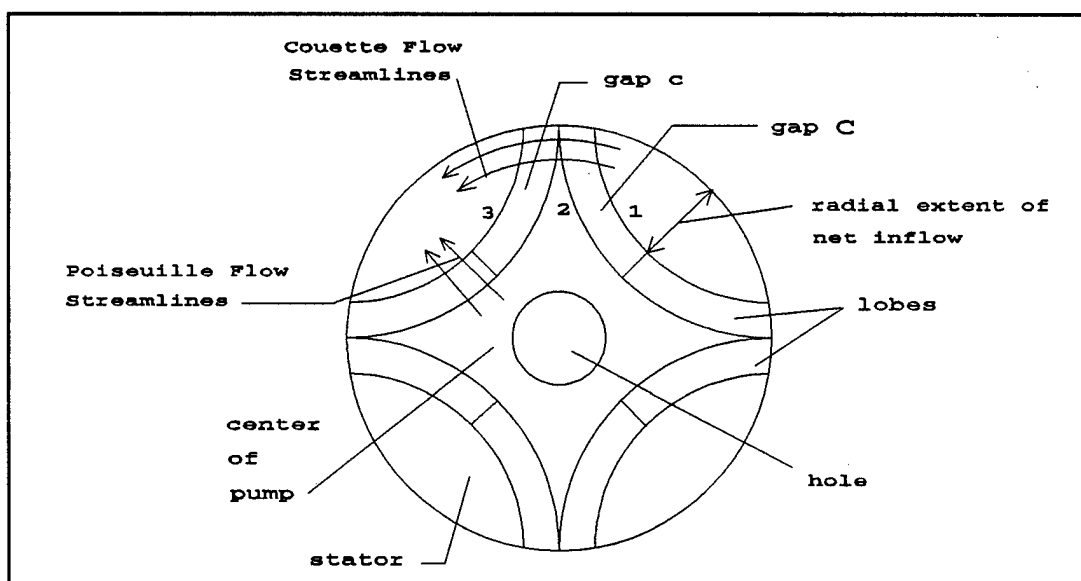


Figure 1 Stator of Semicircular Lobe Viscous Pump

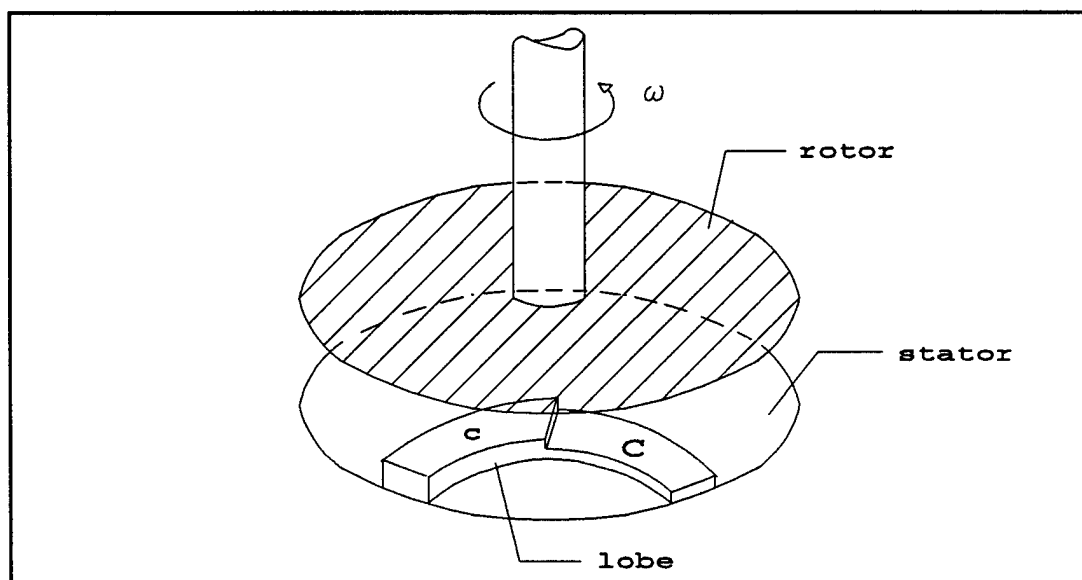


Figure 2 Three Dimensional View of a Lobe (figure not to scale)

the fluid dragged by the rotor into the center of the pump where the fluid exists through a hole in the stator.

Although viscous pumps are not considered to be efficient from a power input conversion standpoint, they have other beneficial qualities. Important features of this pump include nonpulsatile flow rate and discharge pressure, a linear flow-pressure relationship, easy adaptability to a needed flow-pressure operating point, and the absence of dynamic seals or valves or contact between the rotor and stator.

The viscous pump is advantageous for applications requiring easy and accurate flow control such as metering pumps. Although positive displacement (reciprocating) pumps are traditionally used in metering, the viscous pump is advantageous where steady flow is needed. Because there is no contact between moving and stationary parts in the fluid's flow path, nor does this fluid come in contact with any lubricating

fluids, there is no concern of contamination of the fluid. Therefore, the viscous pump would be an appropriate selection for pumping jobs requiring high levels of cleanliness, for example, blood or other biofluid pumps.

The viscous pump can produce flow rates comparable to peristaltic pumps. Peristaltic pumps, however, can be damaging to the process fluid since they operate by squeezing a tube to push the fluid along its flow path. The viscous pump does not produce this potentially harmful normal force. The viscous pump is comparable to other rotary pumps such as screw or gear pumps but avoids the local pressure build up at gear matings which occurs in these pumps and can be damaging to the process fluid. In cases of pumping slurries containing abrasive crystals, such as aluminum dioxide (which has a hardness close to that of a diamond), serious damage to the gear surfaces is highly likely. Slurry pumps requiring mechanical face seals are limited by seal failure related to the abrasive slurries (Manning and Key, 1990). The viscous pump can pump such viscous slurries without being damaged by the abrasive crystals, providing that the gaps between stator lobes and rotor are bigger than the diameter of the crystal.

A pump operates at a particular flow-pressure rise point. For the viscous pump, any desired operating point within the maximum pumping capacity curve can be found by altering the speed and/or the clearance (distance between rotor and stator). Centrifugal pumps are limited in this respect because alternate operating points can only be found by changing the speed, unless complicated variable pitch

impeller blades are used. This provides only limited flexibility in finding a satisfactory operating point. Of course, for both the viscous pump and the centrifugal pump, the lobes or blades could be changed. Another problem with centrifugal pumps is cavitation at very high speeds, which the viscous pump can be designed to avoid.

The design of the lobes is the key to obtaining a net pumping action. The flat rotor disk is parallel to the stator disk and faces the lobes on the stator. The shear induced flow is represented by streamlines which are concentric circumferential lines in the direction of the rotor's rotation. Referring to Figure 1, each lobe is stepped at the middle such that the distance between the rotor and the lobes is the small gap, c , over one portion of the lobe and the large gap, C , over the other portion of the lobe (and the step height is $C-c$). Since the shear induced flow (the Couette flow) is proportional to the radial extent and the gap height, more fluid is sheared into the center of the pump from point 1 to point 2 than is allowed to exit from point 2 to point 3. If the pressure at the center of the pump (where the fluid can exit via a hole at the center of the stator) is greater than the pressure of the fluid surrounding the rotor and stator, then a pressure-gradient induced flow (Poiseuille flow) will travel from the center of the pump, across the lobes and to the area surrounding the pump. Maximum efficiency occurs when the geometry is prescribed such that the net inward Couette flow is maximized while the Poiseuille flow (leakage losses) is minimized.

Etsion and Yaier (1988) analytically investigated a semicircular lobe design

and performed an optimization on the flow equations to determine the optimal geometry for maximum pumping efficiency under given operating conditions. Their optimization, however, does not include all the pertinent geometric variables, particularly the step height, and is therefore revised in this work.

Further improvements in pump efficiency can be realized by reconfiguring the lobe shape. A straight lobe design such as the symmetric V-shaped lobe in Figure 3(a) has the same amount of net inflow but smaller losses than the semicircular lobe. The net inflow, which is provided by the net Couette inflow, is the same because the radial extent of the net inflow and the step height are equal for both lobe designs. The losses, which are caused by the Poiseuille flow, are reduced for the symmetric V-lobe because of the shortened transverse length of the Poiseuille flow. By capitalizing on this idea, the non-symmetric V-lobe (a V with an angular distortion) shown in Figure 3(b) will be investigated to produce the optimal lobe design by further reducing leakage losses. An additional beneficial feature of the V-lobe is that the radial extent of the net inflow can be increased beyond what the semicircular lobes can provide. This means that the V-lobe can be optimized further to have greater flow capacity than the semicircular lobe.

The Reynolds equation (which is the basic equation of hydrodynamic lubrication theory) is used to model the flow field in the pump. Although this equation can be solved using a closed form integration for the semicircular lobe geometry, some approximations must be made to account for the more complex

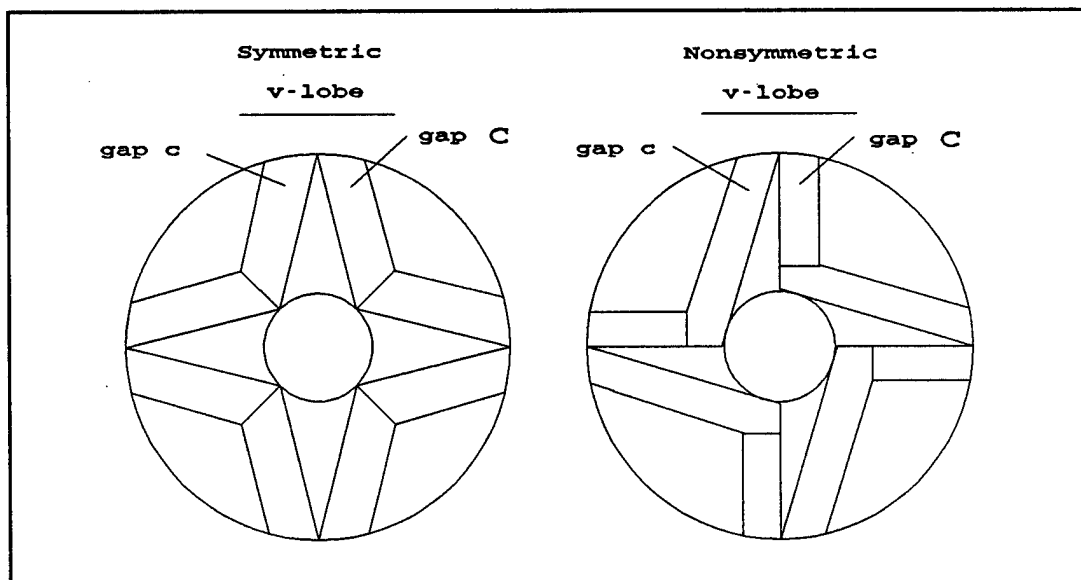


Figure 3 Straight Lobe Designs (a) Symmetric V-lobe (b) Nonsymmetric V-lobe

geometry of the symmetric and non-symmetric V-lobes. The simplifications made will be justified by comparing the simplified analytical model against upper and lower bounds and then to a finite element computational model. The equations will then be optimized for geometry that will produce maximum pumping efficiency.

An experimental investigation of the semicircular lobe design and the non-symmetric V-lobe will be conducted to prove the physical feasibility of the pump and to show the superiority of the non-symmetric V-lobe over the semicircular lobe. The experimental results will then be compared to the results predicted by the analytical models.

CHAPTER II

LITERATURE SURVEY

The idea for this type of viscous pump originated as a new concept for a zero-leakage noncontacting mechanical face seal proposed by Etsion (1984). Mechanical face seals can be categorized as contacting and noncontacting. In comparison, contacting seals minimize leakages through the seal at the cost of increased rotor shaft work due to energy dissipation arising from friction between the rotating shaft and the stator. Reduced component life, damaging high temperatures, and debris generation may also result from the contact. Noncontacting seals, on the other hand, minimize rotor shaft work and wear at the cost of leakage between the rotating and stationary members. Etsion's idea for a noncontacting zero-leakage mechanical face seal incorporates the advantages of both types of mechanical face seals, i.e., minimal energy dissipation between the rotor and stator and zero leakage. The zero leakage was an average zero leakage such that fluid would enter the center of the seal and then be pumped back out. The key to the seal design was specially designed lobes on the stator that create a flow that cancels the flow induced by the pressure gradient across the seal. The idea of the semicircular lobe design was then reformulated as an idea for a viscous pump (Etsion and Yaier, 1988). An optimization of pump geometry for maximum pump efficiency was performed on a limited basis.

An experimental investigation of a semicircular lobe viscous pump was performed by Green et al. (1989). This work proved that the semicircular lobe design provides a feasible pumping mechanism. Significant deviation between theoretical and experimental flow capacity was found, especially at the high pressure - low flow rate conditions. The deviations were largely attributed to indirect measurements inherent to the testing. Several recommendations were included for improvement of the experimental methodology. The key point of the recommendations was to use direct and real time measurement of the pertinent variables, namely the clearance, pressure, temperature and flow rate.

Several other pumps which take advantage of the viscosity of the fluid to transfer energy from the rotor to the fluid have been introduced in the literature.

The shear-force pump, such as that investigated by Hasinger and Kehrt (1963), consists of closely spaced rotor disks with an opening at the center of the disks. Fluid enters the pump axially and is accelerated radially outward by the shearing force created by the rotor. This is a different operating principle than the lobe design viscous pump studied in this work which operates on a principle that allows the acceleration terms to be ignored.

Relatively extensive work has been done in the area of spiral groove viscous pumps, which have typical applications in bearings and seals. The hydrodynamic pressure generated by the pumping action can be used to carry load in the case of the bearing or to seal against leakage in the case of the seal. An analytical and

experimental investigation of flow between a stationary disk and grooved rotating disk by Missimer and Johnson (1982) reveals that, in some cases, radial inertial terms and turbulence are indeed important. Analyses of flow of this nature typically neglect the radial inertia terms and assume laminar flow conditions. The well known narrow groove theory introduced by Vohr and Pan (1969) forms the basis for many investigations related to spiral grooves (e.g., Hsing (1972),(1974)).

A viscous pump with shrouded Rayleigh steps was studied by Sato, et al. (1988). In this pump, the pressure generated by the Rayleigh step (located on the stator and facing the rotor) is the driving force for the flow. The pump geometry was optimized for maximum flow and was shown to be more efficient than a comparable spiral groove viscous pump.

Another application of the viscous pumping mechanism in the area of seals is the investigation of a face seal with shrouded pockets by Walowit and Pinkus (1982).

General cases of flow near a rotating disk, including laminar and turbulent flow regimes, are studied in a text by Schlichting (1968). Cases of a "free" disk and a disk enclosed in a housing are investigated.

Pumping mechanisms such as those described above frequently fall into the classification of lubrication problems (i.e., the Reynolds equation is the governing equation). The Reynolds equation can be solved in closed form for many practical lubrication problems in which the geometry is rather regular (e.g., long and short

bearings). Sometimes, the finite differences method is used to solve such problems. However, in cases of complex or irregular geometries it is highly unlikely to obtain a closed form solution, and the finite difference method may prove to be excessively inefficient and cumbersome to implement. These problems can often be efficiently solved using the finite element method.

The finite element method has received extensive treatment in the literature (e.g., Cook et al., 1989) and has evolved primarily to solve structural problems. It is out of the scope of this work to cover that field. For incompressible lubrication problems in particular, Reddi (1969) explains the finite element method based on a variational principle. A general solution technique for incompressible lubrication problems, also based on a variational principle, is presented by Booker and Huebner (1972). A work that pertains to the current work was performed by Blech et al. (1986) in which a finite element method based on a heat transfer shape factor was developed.

2.1 Recommendations

Analytical and experimental work has been done for various pump designs. We suggest a more efficient pump, namely the V-lobe design introduced above. For this pump, realistic analytical models will be developed using approximating equations, shape factor bounds, and the finite element method. Based on the analyses, both lobe designs will be optimized with respect to lobe geometry to

produce maximum pumping efficiency. Experiments will be performed to compare the V-lobe design to the semicircular design described above. The experimental results will also be compared to the analytical models.

CHAPTER III

ANALYSIS

3.1 Introduction

This work is divided into two components. The first component is the analytical study of both the semicircular lobe, which is the original pump design, and the straight lobe (V-lobe), which is the new pump design. The second component is the experiments which test the semicircular lobe and straight lobe designs.

The analytical work involves the description of the flow using equations and computational checks. The equations are used to optimize the geometry of each of the lobe configurations. First, the semicircular lobe design will be explored followed by the investigation of the straight lobe designs (the symmetric and nonsymmetric V-lobe designs).

For all configurations investigated, the Reynolds equation is assumed to be the governing equation. The Reynolds equation applies to an x - z fluid region, shown in Figure 4, which has height h in the y -direction and (u,v,w) velocity components in the (x,y,z) directions. The following assumptions are made about this fluid region:

1. dimension in the y -direction are small compared
to other dimensions

2. no pressure variation across the fluid film
($\partial p / \partial y = 0$)
3. flow is laminar
4. body forces are negligible
5. inertial forces are negligible
6. no slip at solid boundaries
7. compared to $\partial u / \partial y$ and $\partial w / \partial y$, all other velocity gradients are negligible.

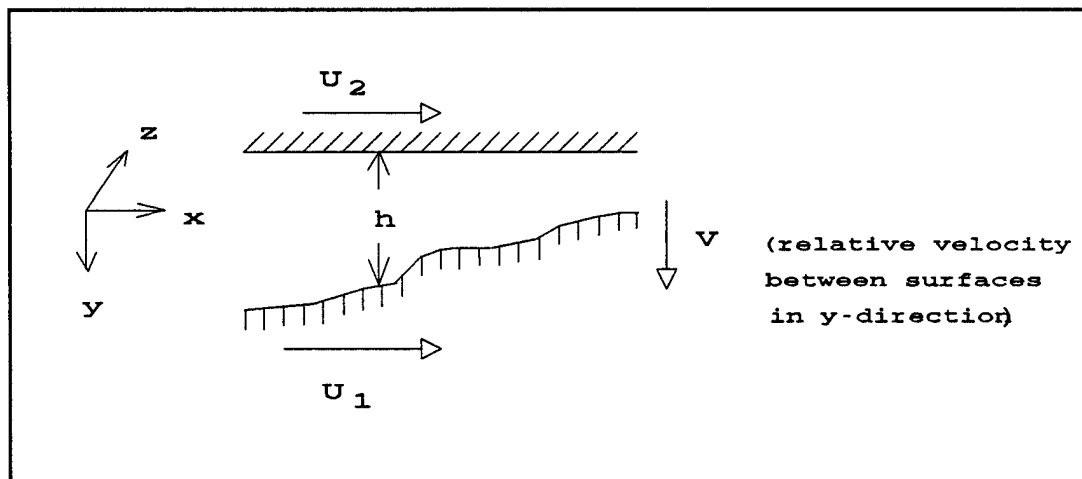


Figure 4 Fluid Film Described By Reynolds Equation

Based on these seven assumptions, the three-dimensional conservation of momentum equations are reduced to a form where they can be integrated across the film thickness, $0 \leq y \leq h$, to solve for the u , v , and w velocity profiles. These velocity profiles are then substituted into the continuity equation. The resulting equation is

integrated across the film thickness to yield the following equation (Gross,1980):

$$\frac{\partial}{\partial x} \left(\frac{\rho h^3}{\mu} \frac{\partial p}{\partial x} \right) + \frac{\partial}{\partial z} \left(\frac{\rho h^3}{\mu} \frac{\partial p}{\partial z} \right) = 6 \frac{\partial}{\partial x} [\rho h(U_1 + U_2)] + 12 \left(\rho V - \rho U_2 \frac{\partial h}{\partial x} + h \frac{\partial \rho}{\partial t} \right) \quad (1)$$

where ρ is the density of the fluid, μ is the absolute viscosity of the fluid, p is the pressure, and the remaining variables are described in Figure 4. For the isothermal, steady, incompressible case with $U = U_1$, $U_2 = 0$, and $V = 0$, this reduces to:

$$\frac{\partial}{\partial x} \left(h^3 \frac{\partial p}{\partial x} \right) + \frac{\partial}{\partial z} \left(h^3 \frac{\partial p}{\partial z} \right) = 6\mu U \frac{\partial h}{\partial x} \quad (2)$$

For this equation, the flow can be calculated by linearly superimposing the Couette and Poiseuille flow components.

3.2 Semicircular Lobe Design

3.2.1 Semicircular Lobe Analysis

Before deriving the equations for the semicircular lobe design, some background regarding the evolution of the pump (which originated as a seal design) is provided. Etsion's idea for the noncontacting zero-leakage mechanical face seal was to design the stator geometry such that the stator would direct the fluid dragged by the rotor in a direction that would cancel the flow induced by the pressure gradient across the seal. Referring to Figure 5, the annular stator faces the rotor disk and has a machined step on its surface. The distance between the rotor and

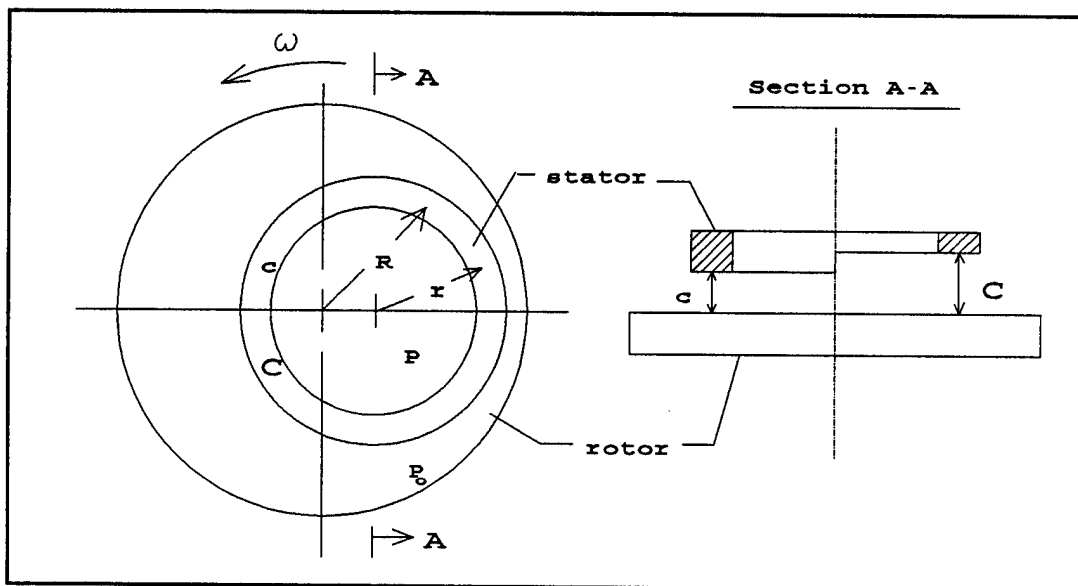


Figure 5 Eccentric Mechanical Face Seal

stepped stator is a large gap, C , over one half of the stator and a smaller gap, c , over the remaining half of the stator. As the rotor rotates, it shears and drags the fluid in towards the center of the stator (which would correspond to the center of the pump) through the large gap, C . At the same time, fluid is dragged out from the stator center through the smaller gap, c . Because the shear induced Couette flow is proportional to the gap height, more fluid enters the center of the stator than exits. The development of Equations (3)-(17) which follow is referenced from Etsion and Yaier (1988). The net inward Couette flow per unit length is given by

$$q_s = \frac{\omega R}{2} (C - c) \quad (3)$$

At the stator interior, a discharge pressure exists which is greater than the pressure

outside the stator. The result is a radially outward Poiseuille flow across the width of the stator lobes through the gaps C and c . This leakage is given by

$$q_{pC} = -\frac{C^3}{12\mu} \frac{\partial p}{\partial r} \quad (4a)$$

$$q_{pc} = -\frac{c^3}{12\mu} \frac{\partial p}{\partial r} \quad (4b)$$

$$q_p = q_{pC} + q_{pc} \quad (4c)$$

The net flow is the sum of these two components (q_s and q_p) integrated around the stator and is given as $Q = Q_s + Q_p$.

The eccentric stator design of Figure 5 gives a nonaxisymmetric pressure field which could cause rotor imbalance and does not readily accommodate a rotating shaft. These problems are overcome by using the design of Figure 1 where the stator is broken into several lobes and placed on an annular disk. Geometric definitions of a lobe are shown in Figure 6 where the annular disk has inside radius R_i and outside radius R_o . The lobes are stepped and form a large gap, C , and a small gap, c , with the rotor and are placed on the stator. At this point, the seal can also be considered a pump.

From the geometry, it can be seen that the angle β is

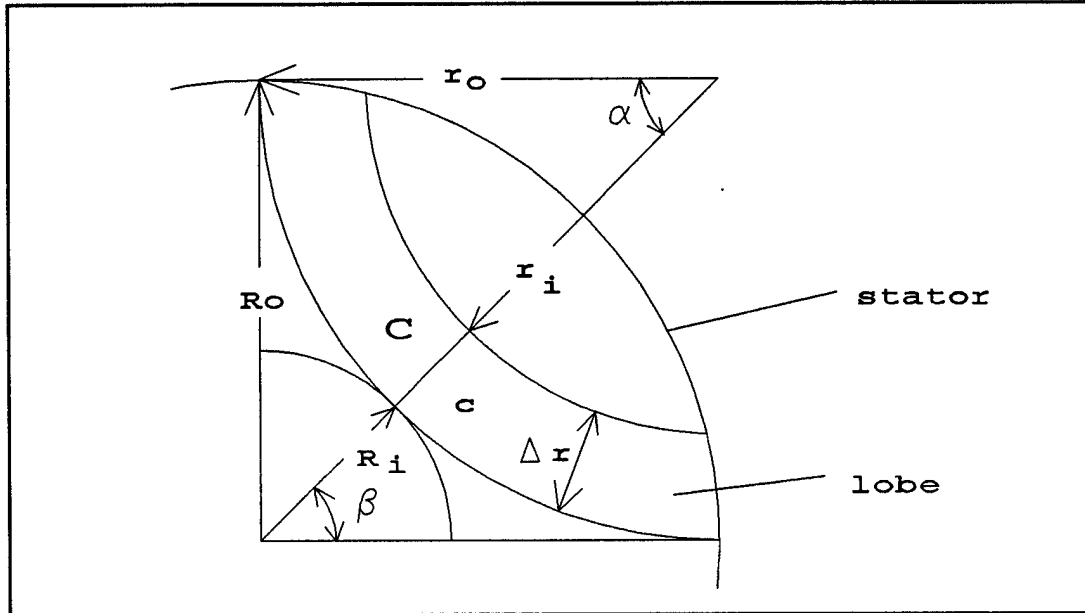


Figure 6 Geometric Variable Definitions For Semicircular Lobe Design

$$\beta = \frac{\pi}{n} \quad (5)$$

where n is the number of lobes.

As mentioned earlier, the equations for flow are obtained by integrating q_s and q_p over their effective lengths. The net Couette flow occurs across the radial distance from $R_i + \Delta r$ to R_o , resulting in

$$Q_s = \int_{R_i + \Delta r}^{R_o} q_s dR \quad (6)$$

Using the equation for q_s (Equation (3)) and defining the machined step height as $s = C - c$, the integration results in the following equation for flow:

$$Q_s = \frac{\omega s}{4} R_o^2 \left[1 - \left(\frac{R_i}{R_o} + \frac{\Delta r}{R_o} \right)^2 \right] \quad (7)$$

The Poiseuille flow is found by integrating the equations for q_p (Equation (4)) along the length of the lobe

$$Q_p = \int_{-\alpha}^0 q_{pc} r d\theta + \int_0^{\alpha} q_{pc} r d\theta \quad (8)$$

This integration yields:

$$Q_p = -\frac{\alpha(c^3 + C^3)}{12\mu} r \frac{\partial p}{\partial r} \quad (9)$$

Since Q_p is constant as r varies and p is a function of r only, Equation (9) can be rewritten as

$$\frac{dp}{dr} = -\frac{12\mu Q_p}{\alpha(C^3 + c^3)} \frac{1}{r} \quad (10)$$

and is subjected to the following boundary conditions:

$$p = P \quad \text{at} \quad r = r_o \quad (\text{inside of pump}) \quad (11a)$$

$$p = 0 \quad \text{at} \quad r = r_i \quad (\text{outside of pump}) \quad (11b)$$

Integrating Equation (10) and employing the boundary conditions results in

$$Q_p = \frac{\alpha}{12\mu} (C^3 + c^3) \frac{P}{\ln\left(1 - \frac{\Delta r}{r_o}\right)} \quad (12)$$

Note that the closed form of this integration relies on approximating the outer edges of the lobes, which are arcs, with secants. The net flow of the pump for n lobes is then given by adding Q_s and Q_p (Equations (7) and (12)) which yields:

$$Q = \frac{n}{4} \omega s R_o^2 \left[1 - \left(\frac{R_i}{R_o} + \frac{\Delta r}{R_o} \right)^2 \right] + \frac{n}{12\mu} (C^3 + c^3) \frac{\alpha P}{\ln\left(1 - \frac{\Delta r}{r_o}\right)} \quad (13)$$

The geometric constraint of lobe tangency at the outer radius requires that

$$\alpha = \frac{\pi}{2} - \beta = \frac{\pi}{2n} (n-2) \quad (14)$$

Introducing F_n , a function of the number of lobes,

$$F_n = \frac{1 - \sin\beta}{\cos\beta} = \frac{R_i}{R_o} \quad (15)$$

and the non-dimensional lobe width, ξ ,

$$\xi = \frac{\Delta r}{R_o} \quad (16)$$

the pump flow is rewritten as

$$Q = \frac{\omega s n}{4} R_o^2 [1 - (F_n + \xi)^2] + \frac{\pi P}{24\mu} (C^3 + c^3) \frac{n-2}{\ln\left(1 - \frac{\xi}{\tan\beta}\right)} \quad (17)$$

The tangency requirement of the semicircular lobe imposes a constraint on the radius R_i through Equations (14) and (15) once the number of lobes, n , and the outer radius, R_o , have been specified.

3.2.2 Semicircular Lobe Optimization

Etsion and Yaier (1988) arrived at Equation (17). The next step is to find the optimal lobe geometry for maximum flow. The variables are the number of lobes, n , the lobe width, ξ , and the step height, s , which is nondimensionalized by the minimal clearance parameter, c ,

$$\sigma = \frac{s}{c} \quad (18)$$

In the work by Etsion and Yaier (1988), the step height was not treated as a variable; it was defined to be a given operating condition. The step height, however, is a geometric variable for design and does not need to be prescribed as an operating condition. Therefore, the step height is treated in the present work as a variable to be optimized for maximum flow. Because of the new role of the step height, this work now bifurcates from the work presented by Etsion and Yaier (1988).

An operating conditions parameter, S' , is defined by

$$S' = \frac{\pi}{12} \frac{P}{\mu \omega} \left(\frac{c}{R_o} \right)^2 \quad (19)$$

S' contains all the variables usually specified by the design requirements of the pump. For example, the viscosity, μ , would be given based on what fluid the pump was being designed to process. The small clearance, c , would be given based on what would be the smallest clearance that would not damage the fluid (due to shear stress or particle size) or the pump (due to very hard particles or contact between the rotor and stator lobes resulting from rotor runout and machining imperfections). S' is equivalent to the inverse of the Sommerfeld number (the bearing-characteristic number) in journal bearings.

The equation for flow can be written as

$$Q = \frac{1}{2} \omega c R_o^2 Q' \quad (20)$$

where Q' is the nondimensionalized flow and includes the operating conditions parameter S' as follows:

$$Q' = \frac{\sigma n}{2} [1 - (F_n + \xi)^2] + S' [(\sigma + 1)^3 + 1] \frac{(n-2)}{\ln \left(1 - \frac{\xi}{\tan \beta} \right)} \quad (21)$$

This equation is optimized for a given operating conditions parameter, S' , by setting its partial derivatives with respect the non-dimensional lobe width, ξ , and the non-dimensional step height, σ , equal to zero for a particular number of lobes, n . From $\partial Q'/\partial \xi = 0$ we obtain

$$F(\xi, \sigma, n) = S' \quad (22)$$

where

$$F(\xi, \sigma, n) = \frac{n\sigma(F_n + \xi) \left[\ln \left(1 - \frac{\xi}{\tan \beta} \right) \right]^2 (\tan \beta - \xi)}{(n-2)[(\sigma+1)^3 + 1]} \quad (23)$$

From $\partial Q'/\partial \sigma = 0$, we obtain

$$G(\xi, \sigma, n) = S' \quad (24)$$

where

$$G(\xi, \sigma, n) = \frac{n[(F_n + \xi)^2 - 1] \ln \left(1 - \frac{\xi}{\tan \beta} \right)}{6(n-2)(\sigma+1)^2} \quad (25)$$

The resulting Equations (22) and (24) were solved simultaneously to yield the optimal values of ξ and σ for the corresponding number of lobes, n , at a given operating conditions parameter, S' . The non-dimensional flow, Q' , was then

computed for these ξ , σ , and n values. Values for Q' were then compared over a range of n values to determine which n (and corresponding ξ and σ) yielded the maximum flow. The optimization was performed in this manner because the number of lobes must be an integer parameter. Table 1 presents the results of the optimization over a range of the operating conditions parameter S' .

A comparison of the values of Q' listed in Table 1 to the optimal flow values obtained by Etsion and Yaier (1988) proves that using an optimal step height improves the efficiency of the pump.

As it turns out, the optimization of Q' is not particularly sensitive to the number of lobes, providing that the corresponding ξ and σ values are used. This finding is depicted in Figure 7 where Q' is plotted as a function of S' for $n = 3, 4$, and 5. Although the maximum Q' occurs at a particular n for a given S' , the variation of

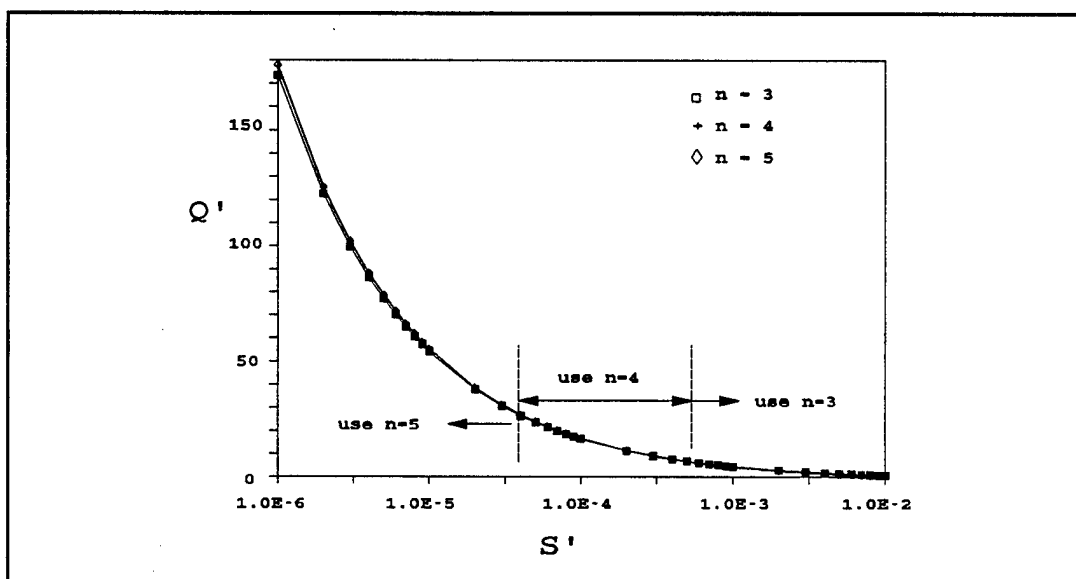


Figure 7 Optimal Pumping For Various Number of Lobes at Given Operating Conditions

Table 1 Semicircular Lobe Optimization Results

S'	Lobes n	Lobe Width ξ	Step Height, σ	Flow Q'
1×10^{-6}	3	0.253	238.96	173.66
	4	0.194	211.73	177.54
	5	0.158	193.23	178.17 *
	6	0.133	179.30	176.93
	7	0.116	168.20	174.65
	8	0.102	159.04	171.81
1×10^{-5}	3	0.255	75.02	54.17
	4	0.195	66.43	55.28
	5	0.159	60.60	55.40 *
	6	0.135	56.20	54.94
	7	0.117	52.70	54.16
	8	0.103	49.80	53.22
1×10^{-4}	3	0.259	23.18	16.39
	4	0.199	20.49	16.62 *
	5	0.163	18.66	16.58
	6	0.138	17.27	16.37
	7	0.120	16.17	16.07
	8	0.107	15.26	15.73
1×10^{-3}	3	0.273	6.79	4.443 *
	4	0.213	5.96	4.407
	5	0.176	5.40	4.310
	6	0.151	4.97	4.180
	7	0.133	4.63	4.036
	8	0.119	4.35	3.888

* Designates maximum flow

Q' with n (and the corresponding ξ and σ values) is only slight. The conclusion to be drawn from this is that although the selection of n is not a critical decision, it is important that its corresponding ξ and σ be used to achieve maximum pumping efficiency.

Another important point to be learned from the study of the equation for Q' (Equation (13)) is that maximum pumping occurs when the minimal clearance is zero. This is not, however, a practical option because this condition corresponds to touchdown between the rotor and stator. This is accompanied by energy dissipation which translates into wear, increased shaft work, heating and possible debris generation. The minimal clearance should therefore be set to a value as close to zero as physically possible. Its minimum practical value would be limited by rotor runout, misalignment, surface roughness and maximum particle size in the fluid being pumped. The next step in the investigation of this viscous pump is to consider alternate lobe configurations.

3.3 Straight Lobes

3.3.1 Introduction

The straight lobe configuration is introduced in Figure 8(a). The straight lobe is a symmetric V-shaped lobe and is shown in relation to the semicircular lobe design. For both lobe designs, the net inward Couette flow is the same. For the symmetric V-lobes, however, the Poiseuille flow is less than the Poiseuille flow of the

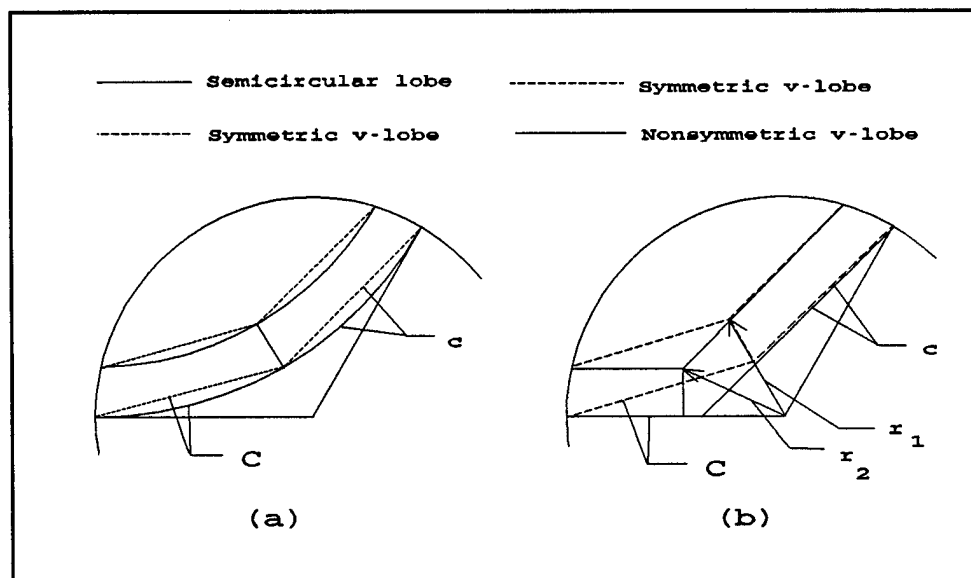


Figure 8 Graphical Comparison of Lobe Designs (a) Symmetric V-lobe Versus Semicircular Lobe (b) Nonsymmetric V-lobe Versus Symmetric V-lobe

semicircular lobe because the symmetric V-lobe has a shorter effective length over which the fluid can flow. In other words, both lobe designs have the same inward flow (pumping) but the symmetric V-lobe design has reduced losses. Thus, the symmetric V-lobe is a superior design. Furthermore, the radial extent of the net inflow, which is provided by the net Couette flow, can be increased beyond that attainable by the semicircular lobe. This point will be discussed in more detail later. Although the symmetric V-lobe design is an improvement over the semicircular lobe design, further beneficial modifications can be made.

Consider Figure 8(b) where the nonsymmetric V-lobe is shown so that it can be compared to the symmetric V-lobe. For both designs, the net inward Couette flow is the same when $r_1 = r_2$. The nonsymmetric V-lobe design, however, has the

potential to have smaller losses (Poiseuille flow) than the symmetric V-lobe. The losses are proportional the gap height raised to the third power (Equation (4), Poiseuille flow). Because the gap between the rotor and stator for the leg of the lobe labelled C (C-leg) is larger than the gap over the leg of the gap labelled c (c-leg), the length of the C-leg should be minimized. The nonsymmetric V-lobe design accomplishes this. It is true that the losses related to the c-leg are increased because this leg is now longer. Note also that for the nonsymmetric V-lobe the total lobe length (length of c-leg plus length of C-leg) is greater than that for the symmetric V-lobe. The increase in losses due to these increased lengths, however, varies only linearly with the length of the leg. In cases where C is sufficiently larger than c, the result will be that the nonsymmetric V-lobe produces higher pumping capabilities than the symmetric V-lobe.

Another important advantage of the straight lobes is that the radial extent of the net inflow, which is provided by the net Couette flow, is not limited by geometric constraints as in the case of the semicircular lobes. For the semicircular lobes, the tangency requirement of the lobes at the outer radius of the stator means that the radial extent of the net inflow is determined by the number of lobes. For large n , this distance becomes very small. The straight lobes are not hindered by this limitation. Theoretically, the radial extent of the net inflow could be the entire radius of the stator. This will be investigated in more detail when the straight lobe optimization results are examined.

As in the case of the semicircular lobe design, the pump geometry of the straight lobe was optimized to achieve maximum flow. This optimization process was applied to both straight lobe designs. Based on the physical reasoning above, the optimal symmetric V-lobe should produce larger flow values than the optimal semicircular lobe design. The reasoning above also suggests that the optimal nonsymmetric V-lobe has the potential to produce flow values superior to the symmetric V-lobe (and thus the semicircular lobe also). Because the nonsymmetric V-lobe did indeed turn out to be the superior design, the equations derived for the symmetric V-lobe are only briefly outlined here. The results of the optimized equations will later be compared to the results related to the nonsymmetric V-lobe to confirm the inferiority of the symmetric V-lobe.

3.3.2 Symmetric V-lobe Design

3.3.2.1 Symmetric V-lobe Analysis. Consider the symmetric V-lobe depicted in Figure 9. The flow was solved for (although not in closed form) in a manner similar to the treatment of the semicircular lobes, i.e., superimposing the Couette and Poiseuille components of flow. The Couette component was straightforward and exact. Using the equation for Couette flow (Equation (3)), the following equation applies to this geometry:

$$Q_s = \int_{R_i}^{R_o} \frac{\omega R}{2} (C - c) dR \quad (26)$$

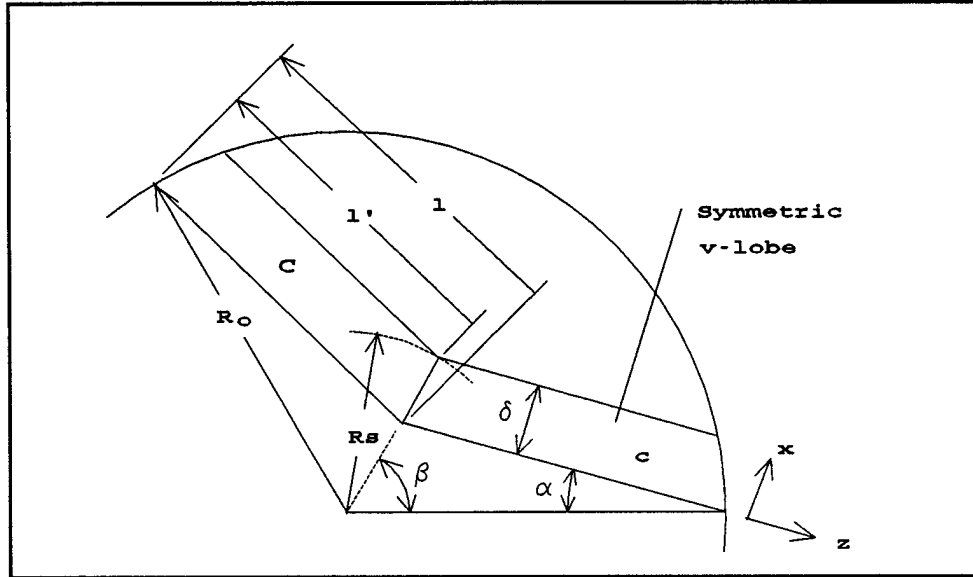


Figure 9 Geometric Variable Definitions For Symmetric V-lobe Design

where

$$R_s = \frac{R_o \sin \alpha + \delta}{\sin(\alpha + \beta)} \quad (27)$$

Upon integration, the net Couette flow is

$$Q_s = \frac{\omega s}{4} \left\{ R_o^2 - \left[\frac{R_o \sin \alpha + \delta}{\sin(\alpha + \beta)} \right]^2 \right\} \quad (28)$$

The Poiseuille component could not be solved in a closed form due to the complicated geometry. Here, the streamlines are assumed to traverse the lobes perpendicular to the length of the lobe over the length l' on Figure 9. This model assumes that the top of the lobe (the region where the legs of the lobe meet) does

not contribute to the flow and that the pressure gradient, $\partial p / \partial x$, is P / δ for the length l' . A more conservative (i.e., allows greater losses), though conceivably less accurate model, would assume a length of l instead of l' . Using Equation (4), the Poiseuille component is written as

$$Q_p = \int_0^{l'} \frac{C^3}{12\mu} \frac{\partial p}{\partial x} dz + \int_0^{l'} \frac{c^3}{12\mu} \frac{\partial p}{\partial x} dz \quad (29)$$

Alternatively, l could replace l' in the Equation (29). Using the boundary conditions $p=P$ at $x=0$ and $p=0$ at $x=\delta$, the integration of Equation (29) yields

$$Q_p = -\frac{P(C^3+c^3)}{12\mu\delta} \frac{R_o \sin\beta}{\sin(\alpha+\beta)} \quad (30)$$

when using the length l , and

$$Q_p = -\frac{P(C^3+c^3)}{12\mu\delta} \frac{R_o \sin\beta - \delta \cos(\alpha+\beta)}{\sin(\alpha+\beta)} \quad (31)$$

when using the length l' . The total flow is the sum of the Couette and Poiseuille components for n lobes and is written as

$$Q = n \left\{ \frac{\omega s}{4} \left[R_o^2 - \left(\frac{R_o \sin\alpha + \delta}{\sin(\alpha+\beta)} \right)^2 \right] - \frac{P(C^3+c^3)R_o \sin\beta}{12\mu\delta \sin(\alpha+\beta)} \right\} \quad (32)$$

when using the length l , and

$$Q = n \left\{ \frac{\omega s}{4} \left[R_o^2 - \left(\frac{R_o \sin \alpha + \delta}{\sin(\alpha + \beta)} \right)^2 \right] - \frac{P(C^3 + c^3)[R_o \sin \beta - \delta \cos(\alpha + \beta)]}{12\mu \delta \sin(\alpha + \beta)} \right\} \quad (33)$$

when using the length l' . The equation for Q was nondimensionalized by the operating conditions as in Equation (20) for the semicircular lobe design. Using the operating conditions parameter, S' , and the nondimensional variables, $\sigma = s/c$ and $\xi = \delta/R_o$, the resulting equations are

$$Q' = n \left\{ \frac{\sigma}{2} \left[1 - \left(\frac{\sin \alpha + \xi}{\sin(\alpha + \beta)} \right)^2 \right] - 2S' \frac{[(1 + \sigma)^3 + 1] \sin \beta}{\pi \xi \sin(\alpha + \beta)} \right\} \quad (34)$$

when using the length l , and

$$Q' = n \left\{ \frac{\sigma}{2} \left[1 - \left(\frac{\sin \alpha + \xi}{\sin(\alpha + \beta)} \right)^2 \right] - 2S' \frac{[(1 + \sigma)^3 + 1] [\sin \beta - \xi \cos(\alpha + \beta)]}{\pi \xi \sin(\alpha + \beta)} \right\} \quad (35)$$

when using the length l' .

3.3.2.2 Symmetric V-lobe Optimization. These dimensionless equations for flow were next optimized and compared to the semicircular lobes. The general method of optimization was to vary the variables α , σ , and ξ for $n = 3, 4, 5, \dots$ for a given operating conditions parameter, S' , to find which geometry yielded maximum flow. The optimization procedure was performed using two approaches for the case of the l length. The first approach involved taking the partial derivative of the flow

equation (for a given S') which respect to α , σ and ξ , setting these equations equal to zero, and then solving the equations simultaneously. This was done over a range of n values so that the optimal n value could be selected. The second approach was to use a numerical method known as the path of steepest descent (in the IMSL library) to determine the values of α , σ , and ξ which yielded maximum flow. The method of path of steepest descent solves for the minimum of a function of m variables. The function can be pictured as an m -dimension surface with a dip in it that represents the minimum. The method sends out feelers along the surface across increments of each variable to determine which path has the steepest slope of descent. The method then moves in this direction and repeats the process. If stability is maintained, the method will end up at the lowest point on the surface (the function minimum). The value of the variables here are the optimized values which provide a minimum function value. Of course, using the negative of the function results in maximizing the function. Both approaches, namely solving the equations simultaneously and the method of path of steepest descent, yielded the same results (as expected) which justified the use of the more convenient path of steepest descent method.

Because the symmetric V-lobe was only a step towards the best lobe configuration (this did, however, need to be proved), only brief results of the optimization are displayed. The results for $S' = 1 \times 10^{-3}$ are presented in Table 2. This table compares the optimization results obtained for the semicircular lobes, the

Table 2 Symmetric V-lobe Optimization Results

Q' ($S' = 1 \times 10^{-3}$)			
n	Semicircular lobe	Symmetric v-lobe (l)	Symmetric v-lobe (l')
3	4.443	6.066	6.971
4	4.407	7.144	8.905
5	4.310	7.954	10.435
6	4.180	8.604	11.699
7	4.036	9.146	12.774
8	3.888	9.608	13.711
9	3.741	10.008	14.541

symmetric V-lobe using the length l, and the symmetric V-lobe using the length l'. Note that even the conservative l model still outperforms the semicircular lobe design. The straight lobe design is clearly more efficient than the semicircular lobe design. Also of interest is the fact that Q' decreases as n increases for the semicircular lobe. Maximum Q' occurs at $n=3$ for this S' . For the V-lobe, however, an maximum value of Q' with respect to n is not found; Q' continues to increase as n increases. While this is true in theory, it is not a physically realizable situation. If the number of lobes becomes too large, the fluid will not have sufficient room to enter the center of the pump. The physically practical limit on the number of lobes

would depend on the application.

3.3.3 Nonsymmetric V-lobe Design

3.3.3.1 Nonsymmetric V-lobe Analysis. As mentioned earlier, the nonsymmetric V-lobe has the potential to yield even higher pumping efficiency than the symmetric V-lobe. The geometry to be considered is in Figure 10. The important feature in this design is that the leg that has the large gap, C , is shorter than the leg that has the small gap, c . Since the Poiseuille flow (which represents the losses) is proportional to the gap height raised to the third power, the losses here should be lower than the symmetric V-lobe where the legs are of equal length. The variables are the lobe width, δ , the step height, $s = C - c$, the angle, α , and the number of lobes, n . The Couette flow is represented by employing Equation (26) for the

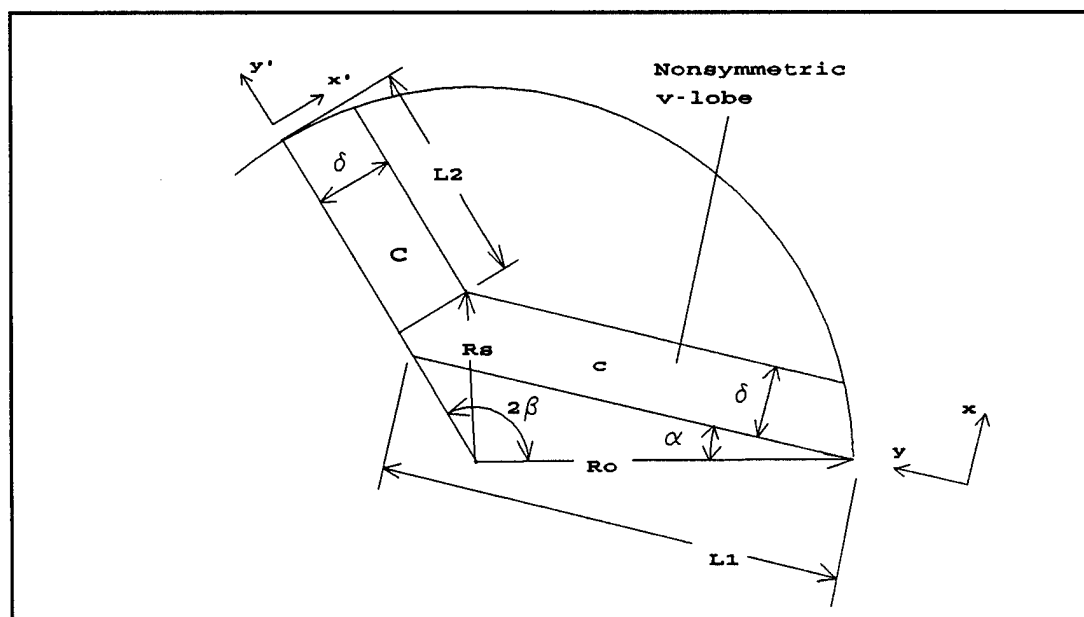


Figure 10 Geometric Variable Definitions For Nonsymmetric V-lobe Design

geometry in Figure 10. Upon integration for this geometry, the net Couette flow is given by the following:

$$Q_s = \frac{\omega s}{4}(R_o^2 - R_s^2) \quad (36)$$

where

$$R_s^2 = \delta^2 + \left[\frac{R_o \sin \alpha}{\sin(\alpha + 2\beta)} + \frac{\delta}{\tan\left(\frac{\alpha + 2\beta}{2}\right)} \right]^2 \quad (37)$$

The Poiseuille component cannot be solved exactly, so some approximations were made. For the c-leg (the long leg with gap c), it was assumed that the pressure gradient, $\partial p / \partial x$, is P / δ for the length $L1$. For the C-leg (the short leg with gap C), it was assumed that the pressure gradient, $\partial p / \partial x'$, is P / δ for the length $L2$. Following the procedure used to solve for the Poiseuille component in the symmetric V-lobe design, the following equation was obtained

$$Q_p = -\frac{C^3 P}{12\mu\delta} \left[R_o - \frac{\delta}{\tan \psi} - \frac{R_o \sin \alpha}{\sin(\alpha + 2\beta)} \right] - \frac{c^3 P}{12\mu\delta} \left[\frac{R_o \sin 2\beta}{\sin(\alpha + 2\beta)} \right] \quad (38)$$

where $\psi = (\alpha + 2\beta)/2$. Q_s and Q_p (Equations (36) and (38)) were added together to account for the total flow for n lobes:

$$Q = \frac{n\omega s}{4} \left(R_o^2 - \left\{ \delta^2 + \left[\frac{R_o \sin \alpha}{\sin(\alpha + \beta)} + \frac{\delta}{\tan \psi} \right]^2 \right\} \right) - \frac{nP}{12\mu \delta} \left\{ C^3 \left[R_o - \frac{\delta}{\tan \psi} - \frac{\sin \alpha}{\sin(\alpha + 2\beta)} \right] + c^3 \left[\frac{R_o \sin 2\beta}{\sin(\alpha + 2\beta)} \right] \right\} \quad (39)$$

As in the case of the other lobe designs, Q' was solved for (using Equations (18)-(20)). For the nonsymmetric V-lobe, the dimensionless flow is

$$Q' = n \left\{ \frac{\sigma}{2} \left[1 - \xi^2 - \left(\frac{\sin \alpha}{\sin(\alpha + 2\beta)} + \frac{\xi}{\tan \psi} \right)^2 \right] - \frac{2S'}{\xi \pi} \left[(1 + \sigma)^3 \left(1 - \frac{\xi}{\tan \psi} - \frac{\sin \alpha}{\sin(\alpha + 2\beta)} \right) + \frac{\sin(2\beta)}{\sin(\alpha + 2\beta)} \right] \right\} \quad (40)$$

where $\xi = \delta/R_o$ and $\sigma = s/c$. Complete derivations of the flow equations outlined above for the V-lobe designs are available in Appendix A.

3.3.3.2 Nonsymmetric V-lobe Optimization. The next step in the investigation of the nonsymmetric V-lobe is to optimize Equation (40) with respect to the variables α , ξ , σ and n . The optimization was performed using the method of path of steepest descent in the IMSL library and the results are presented in Table 3.

The results show that Q' increases as n increases, just as in the symmetric V-

Table 3 Nonsymmetric V-lobe Optimization Results

S'	n	Lobe width, ξ	Angle α (deg)	Step height, σ	Flow Q'
1×10^{-6}	3	0.362	0.0	313.3	258.3
	4	0.313	0.0	308.6	330.4
	5	0.269	0.0	296.5	389.8
	6	0.234	0.0	282.9	440.7
	7	0.207	0.0	269.6	485.6
	8	0.184	0.0	257.2	526.2
1×10^{-5}	3	0.363	0.0	98.5	80.8
	4	0.314	0.0	97.1	103.4
	5	0.270	0.0	93.3	121.9
	6	0.235	0.0	89.0	137.8
	7	0.207	0.0	84.8	151.7
	8	0.185	0.0	80.9	164.2
1×10^{-4}	3	0.367	0.0	30.6	24.7
	4	0.317	0.0	30.2	31.6
	5	0.274	0.0	29.0	37.2
	6	0.238	0.0	27.7	42.0
	7	0.210	0.0	26.4	46.1
	8	0.188	0.0	25.1	49.9
1×10^{-3}	3	0.379	0.0	9.13	6.98
	4	0.329	0.0	9.03	8.90
	5	0.284	0.0	8.68	10.43
	6	0.249	0.0	8.23	11.69
	7	0.220	0.0	7.88	12.77
	8	0.197	0.0	7.50	13.70

lobe optimization. While a very large number of lobes is possible in theory, it would not be practical because there would not be sufficient room for the fluid to flow into the center of the pump. Note also that in all cases, the optimal α is zero degrees. This makes sense since $\alpha=0^\circ$ provides for maximum lobe thickness, δ , (and therefore minimum Poiseuille losses) for a given net Couette inflow. Again, $\alpha=0^\circ$ is not a practical value since there is no room for the fluid to enter the center of the pump. Later, the geometry will be optimized for practical α values.

Before comparing the values for Q' in Table 3 to the values for Q' obtained in the semicircular lobe and symmetric V-lobe optimizations, the validity of the equations used to approximate the Poiseuille component of flow for the nonsymmetric V-lobe had to be checked. One of the major purposes of this work was to derive a lobe configuration that is superior to the semicircular lobe in theory and then to run an experiment that would test and compare the designs. This purpose necessitates a check on the validity of the V-lobe equations to ensure a fair theoretical comparison is made as well as to ensure that the correct optimal values of α , σ and ξ for the nonsymmetric V-lobe were used in the experiment. To check the validity, shape factors borrowed from heat transfer (Kreith and Bohn,(1986) and Blech et al., (1986)) were used to see if the equations fell within the bounds of the possible solutions. Following this, the finite element method (FEM) was used to check the more detailed accuracy of the equations.

3.3.4 Verification of Analysis Using Shape Factors

Shape factors used in conduction heat transfer are used to solve for upper and lower bounds for the flow of heat for a given geometry. The equations derived from the bounds can then be used for preliminary design or optimization calculations. The equations are more helpful than a finite element or difference numerical solution because they offer a closed form solution which can be used to optimize the variables directly. Optimization using finite element or difference results would have to be done on a case by case basis.

For the geometry being considered, the potential (e.g., temperature) is governed by the Laplace equation with Dirichlet boundary conditions over one portion of the boundaries and insulated (no flow) conditions over the remaining boundaries.

Although shape factors are traditionally applied to heat transfer problems, they can also be used in lubrication and fluid flow problems such as the Poiseuille flow over the lobes under study in this work. As far as the author knows, this is the first time that shape factors have been used for fluid flow applications. An informal proof and discussion of the reasoning behind shape factors and their application to fluid flow is presented in Appendix B and will be briefly outlined here.

The shape factor represents an effective length to width ratio. The flow can be calculated using $Q = KS(\phi_1 - \phi_2)$ where Q is the flow, K is the conductance, S is the geometrical shape factor and ϕ is the potential. In heat transfer, Q is the flow of

heat, the temperature, T , is the potential and K is the conductivity of the material. The lower bound shape factor, S_l , is found by assuming that insulated (adiabatic) lines govern the flow of heat and then integrating the differential shape factor for these insulated strips over the entire body. The upper bound shape factor, S_u , is found by assuming that isotherms govern the temperature field of the body and then integrating the differential shape factor for these isotherms over the entire body.

The Poiseuille flow problem is analogous to the heat flow problem. The potential is the pressure, P , the conductance is $h^3/12\mu$, where h is the fluid film thickness and μ is the absolute viscosity of the fluid, and the flow is of course the fluid flow. The shape factor, which is determined solely by geometry, is the same as in the heat transfer problem. The upper bound is found by assuming isobars, which are analogous to the heat transfer isotherms. The lower bound is found by assuming insulated lines across which there is no fluid flow (analogous to heat flow). These insulated lines are in fact streamlines.

For the problem at hand, bounds must be found for the Poiseuille flow over the V-lobes. We wish to see if the equations predict a reasonable pressure-flow relationship. Each of the lobe legs can be generically described by the geometry of Figure 11. Although one end of each lobe leg is an arc, it will be approximated as a secant for the investigation here. The upper bound shape factor is found in reference to Figure 11(a) and using a resistance, $R=1/S$, as follows:

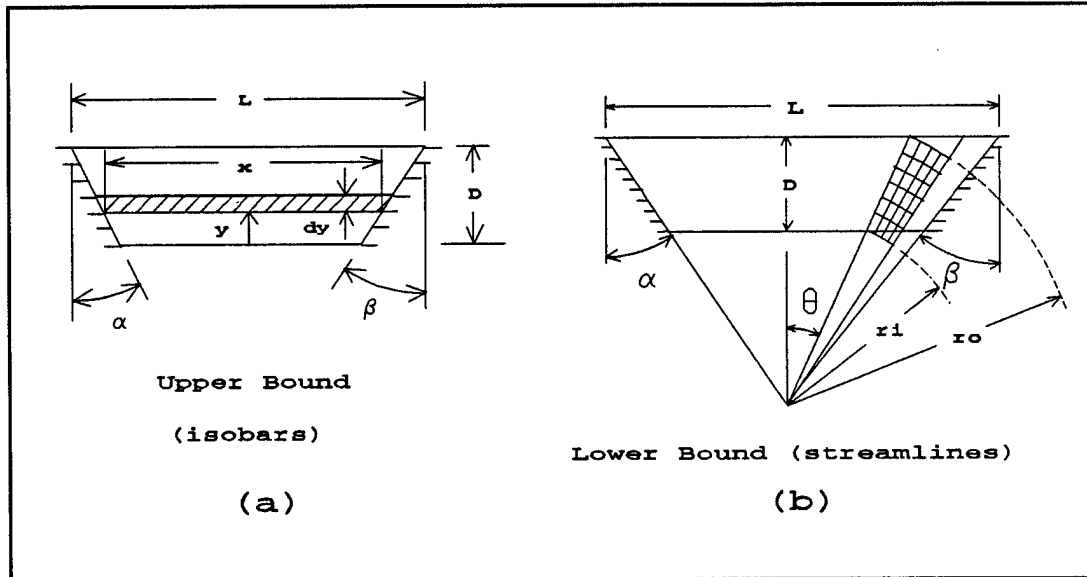


Figure 11 Generic V-lobe Geometry For Shape Factors (a) Upper Bound (b) Lower Bound

$$dR = \frac{dy}{x} = \frac{dy}{L + (y-D)(\tan\alpha + \tan\beta)} \quad (41)$$

$$R = \frac{\ln\left(\frac{L}{L-D(\tan\alpha + \tan\beta)}\right)}{\tan\alpha + \tan\beta} \quad (42)$$

$$S_u = \frac{1}{R} = \frac{\tan\alpha + \tan\beta}{\ln\left(\frac{L}{L-D(\tan\alpha + \tan\beta)}\right)} \quad (43)$$

The lower bound shape factor is found using the variables of Figure 11(b). The calculation of this shape factor involves some approximations which are discussed in detail in Appendix B. The geometry is broken into two pieces, namely $0 \leq \theta \leq \alpha$, and

$0 \leq \theta \leq \beta$. The procedure for each piece is as follows:

$$dR = \frac{dr}{r\Delta\theta} ; \quad \Delta R = \frac{1}{\Delta\theta} \ln \frac{r_o}{r_i} ; \quad \Delta S = \frac{1}{\Delta R} = \frac{\Delta\theta}{\ln \frac{r_o}{r_i}} \quad (44)$$

$$S = \int_0^{\theta_{\max}} \frac{d\theta}{\ln \frac{r_o}{r_i}} \quad (45)$$

The total shape factor is found by integrating Equation (45) for $\theta_{\max} = \alpha$ and $\theta_{\max} = \beta$ and adding the results together. The final lower limit shape factor is:

$$S_l = \frac{\alpha + \beta}{\ln \left(\frac{L}{L - D(\tan\alpha + \tan\beta)} \right)} \quad (46)$$

The flow predicted by the equations can now be compared to the flow calculated using these bounds to see if the equations are appropriate. Since the equation for Couette flow is exact, it will be used with the bounded Poiseuille flows to account for the total flow. The comparison needs to be done for a particular geometry and operating conditions. We will jump ahead and use the geometry and operating conditions used in the experiment, though any set of conditions could be used. Figure 12 shows that the equation for flow of the nonsymmetric V-lobe (Equation (39)) predicts pump performance very close to the flows predicted using the bounds.

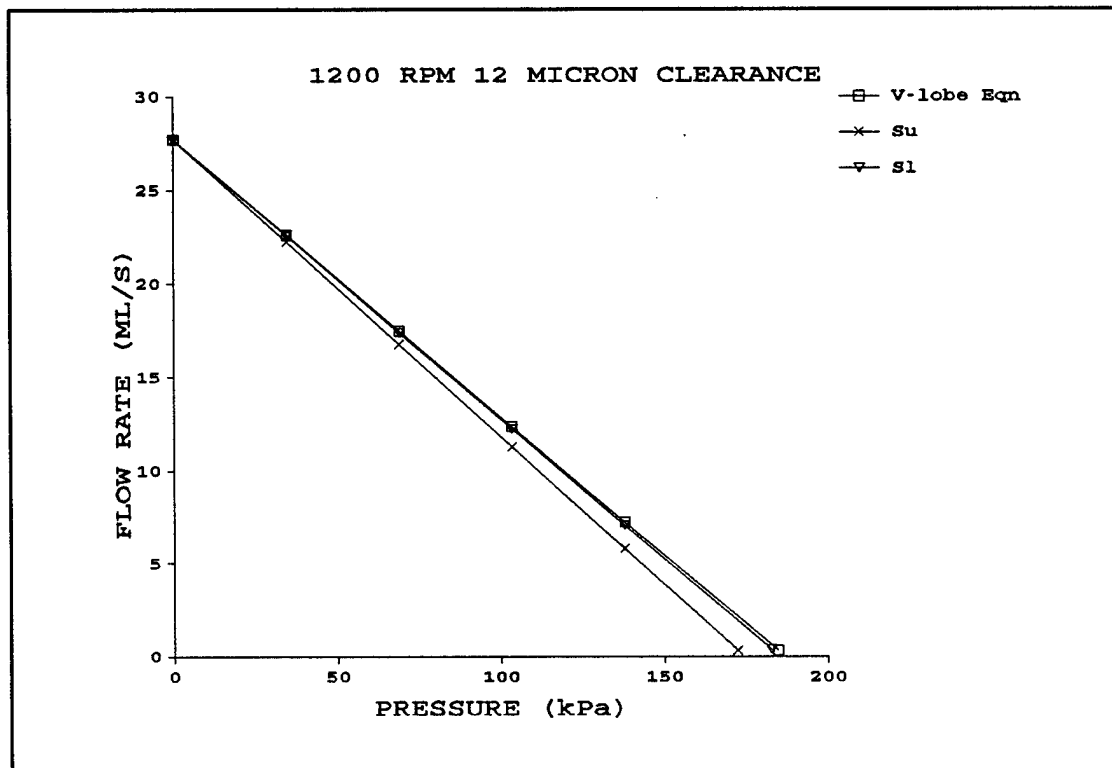


Figure 12 Comparison of Flow Predicted By Bounds To Flow Predicted by Analysis (Equation (39))

Note that the flow corresponding to S_1 is higher than the flow corresponding to S_u . This is true because the lower and upper bounds are used to determine the losses (Poiseuille flow). The total flow equals the magnitude of the Couette flow minus the magnitude of the Poiseuille flow. S_1 determines a lower bound for the Poiseuille flow which is an upper bound for the total net flow. Likewise, S_u determines an upper bound for the Poiseuille flow which is a lower bound for the total net flow. Although the results from the equation are slightly out of the range predicted by the bounds, the variation is negligible. Some tolerance is allowed since the end of the lobe legs are arcs and the shape factors are calculated by approximating these arcs with

secants. The equations approximate the arcs with perpendicular lines. The difference between these two approximations is illustrated in Figure 13.

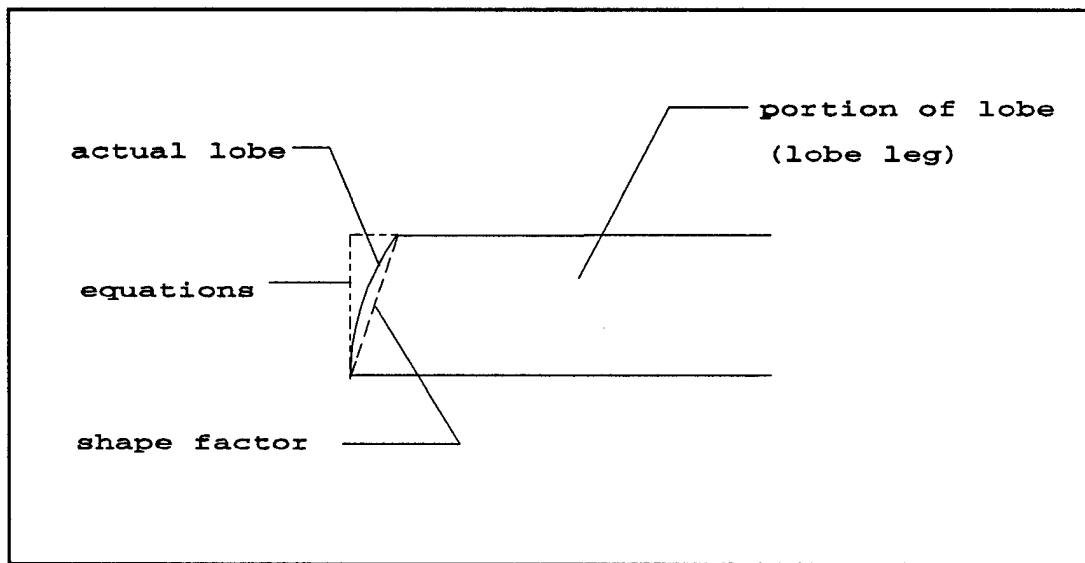


Figure 13 Geometric Approximation of Lobe Leg Ends

Using the shape factors is a quick and uncomplicated method of obtaining an initial guess for the flow. Since the pumping capacity based on the equations falls in the range of the pumping capacity suggested by the bounds, a closer inspection of the equations will now be performed using the finite element method.

3.3.5 Verification of Analysis Using Finite Element Method

The finite element model can only be solved for a given geometry, i.e. it cannot be used to arrive at an optimal geometry unless the optimization process is done on a case by case basis. Concerning numerical solution of partial differential equations, the finite element method has the advantage over finite difference

methods because it is much more adept at handling irregular geometries (such as the lobes studied here). The finite element model was solved over a range of geometries for the nonsymmetric V-lobe configuration. The approach used was a finite element formulation using Galerkin's method. This method can be applied to a field equation of the general form:

$$\frac{\partial}{\partial x}(k_x \phi_x) + \frac{\partial}{\partial y}(k_y \phi_y) + Q = 0 \quad (47)$$

The essential boundary conditions are

$$\phi = \phi(x,y) \quad (48)$$

over a defined portion of the boundaries and the nonessential boundary conditions over the remaining boundaries are

$$n_x k_x \phi_x + n_y k_y \phi_y - q_b = 0 \quad (49)$$

where n_x and n_y are the components of n , the normal to the boundary.

The field equation (Equation (47)) is multiplied by an interpolation function, $[N]^T$, and integrated over a domain, R , to produce Galerkin's general two-dimension residual equation:

$$\int_R [N]^T \left[\frac{\partial}{\partial x}(k_x \phi_x) + \frac{\partial}{\partial y}(k_y \phi_y) + Q \right] dx dy = 0 \quad (50)$$

Applying Green's Theorem to terms in Equation (50) produces

$$\int_R [N]^T \frac{\partial}{\partial x} (k_x \phi_x) dx dy = - \int_R [N_x]^T k_x \phi_x dx dy + \int_B [N]^T k_x \phi_x n_x dS \quad (51)$$

and

$$\int_R [N]^T \frac{\partial}{\partial y} (k_y \phi_y) dx dy = - \int_R [N_y]^T k_y \phi_y dx dy + \int_B [N]^T k_y \phi_y n_y dS \quad (52)$$

where B is the boundary of the domain, R. The potential, ϕ , and its derivatives can be expressed as functions of nodal values through the interpolation function, [N], and its derivatives as follows:

$$\phi = [N]\phi_e ; \quad \phi_x = [N_x]\phi_e ; \quad \phi_y = [N_y]\phi_e \quad (53)$$

Equations (49), (51), (52), and (53) are substituted into Galerkin's residual equation (Equation (50)). The result of this substitution is

$$\left[\int_R ([N_x]^T k_x [N_x] + [N_y]^T k_y [N_y]) dx dy \right] \{\phi_e\} = \int_R [N]^T Q dx dy + \int_B q_B dS \quad (54)$$

For incompressible and steady conditions, the Reynolds equation (Equation (2)) can be written as the field equation (Equation(46)) for $k_x=k_y=h^3$, $\phi=p$ and $Q=-6\mu U \partial h / \partial x$. The approach outlined for the finite element solution of the Reynolds equation was presented by Green (1989) and was used as the basis for a

FORTTRAN program included in Appendix C written to solve the Reynolds equation. This formulation can be applied to the Poiseuille flow over the V-lobe. The purpose of studying the Poiseuille flow over the nonsymmetric V-lobe is to check to see if using the effective leg lengths L1 and L2 is appropriate. For the Poiseuille flow over the V-lobe, $U=0$, and the Reynolds equation reduces to

$$\frac{\partial}{\partial x}(h^3 \frac{\partial p}{\partial x}) + \frac{\partial}{\partial z}(h^3 \frac{\partial p}{\partial z}) = 0 \quad (55)$$

The height, h , is C over the short leg, and c over the long leg as in Figure 10. Since h is constant over each of the legs, Equation (55) yields the Laplace equation.

The physical interpretation of Equation (54) is

$$[k] \{P\} = \{F\} \quad (56)$$

where $[k]$ is the stiffness or fluidity matrix, $\{F\}$ is the loading function (boundary conditions and flow) and $\{P\}$ is the resulting nodal pressure to be solved for. The general idea for the application of Equation (54) is to divide the area over which the field equation applies into many elements. The value of the dependent variable, p , at any point within the element is then assumed to be a linear interpolation of the value of the dependent variable at the element nodes. Referring to Figure 14, the interpolation function, $[N]$, for an element of area A is:

$$[N] = \begin{Bmatrix} N_1 \\ N_2 \\ N_3 \end{Bmatrix} = \frac{1}{2A} \begin{bmatrix} a_1 & b_1 & c_1 \\ a_2 & b_2 & c_2 \\ a_3 & b_3 & c_3 \end{bmatrix} \begin{Bmatrix} 1 \\ x \\ z \end{Bmatrix} \quad (57)$$

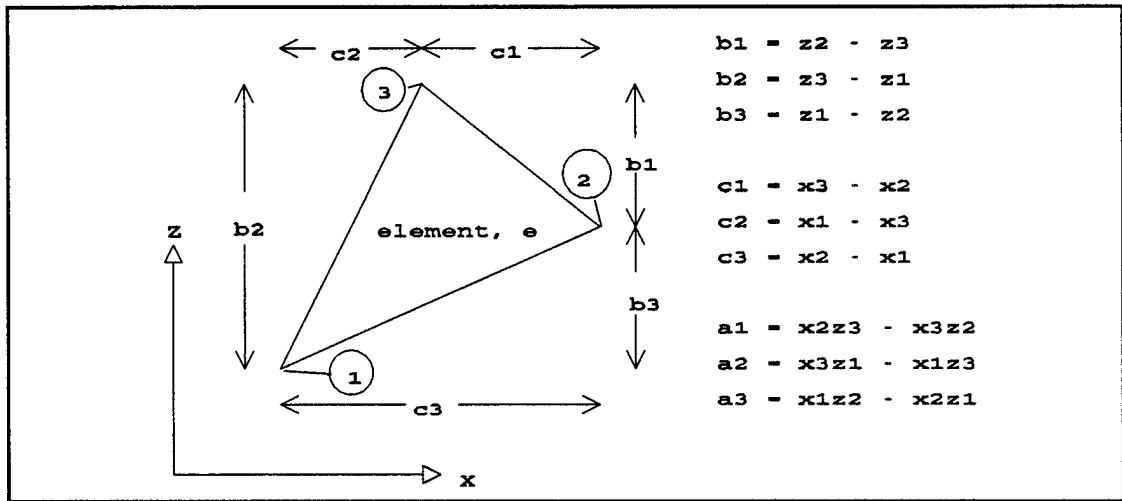


Figure 14 Natural Area Coordinates For Finite Element Formulation

The pressure at any point within an element can be interpolated from the values of the pressure at the element nodes using $P = N_1 P_1 + N_2 P_2 + N_3 P_3$. Since $\partial N_i / \partial x = b_i / 2A$ and $\partial N_i / \partial z = c_i / 2A$, a member of the elemental stiffness matrix is

$$k_{ij} = (b_i b_j + c_i c_j) \int_R h^3 dx dz \quad (58)$$

The loading vector is simply zero everywhere before application of the boundary conditions. The elemental stiffness matrix, $[k]$, is assembled into a global stiffness

matrix which describes the entire lobe. The boundary conditions are then incorporated in the global system of equations. The solution to the pressure field is solution of M equations, where M is the number of unknowns. The mesh selected is considered to produce a converged solution if increasing M does not affect the values obtained for the pressure field.

A value of $C/c = 6$ for the fluid film height ratio was selected for the FEM model. The optimization of the pump equations yielded values in this range and higher. The lower end value of six was selected instead of a higher value so that the contribution of the c-leg could be examined. If a larger C/c value were selected, the flow contribution over the c-leg would be reduced to insignificance by the dominance of the flow over the C-leg. Remember that the purpose of the FEM model is to check the appropriateness of the use of the lengths $L1$ and $L2$.

The boundary conditions are $p=P$ along the lower edge of the lobe and $p=0$ along the upper edge of the lobe as shown in Figure 15¹. The boundary conditions at the outer end of the legs are needed but not physically defined. Along these ends, the pressure must change from a value of P to a value of 0. The assumption made for this boundary condition was that the pressure varies linearly along the ends, i.e., $\partial p/\partial s = \text{constant}$ (s is the path along the ends of the legs). The condition of having a constant pressure gradient along the leg ends corresponds closely to the condition

¹The $p=0$ boundary condition does not mean the pressure is actually zero (ambient). Instead, $p=0$ is interpreted to be a value relative to $p=P$ (i.e., P is a differential pressure).

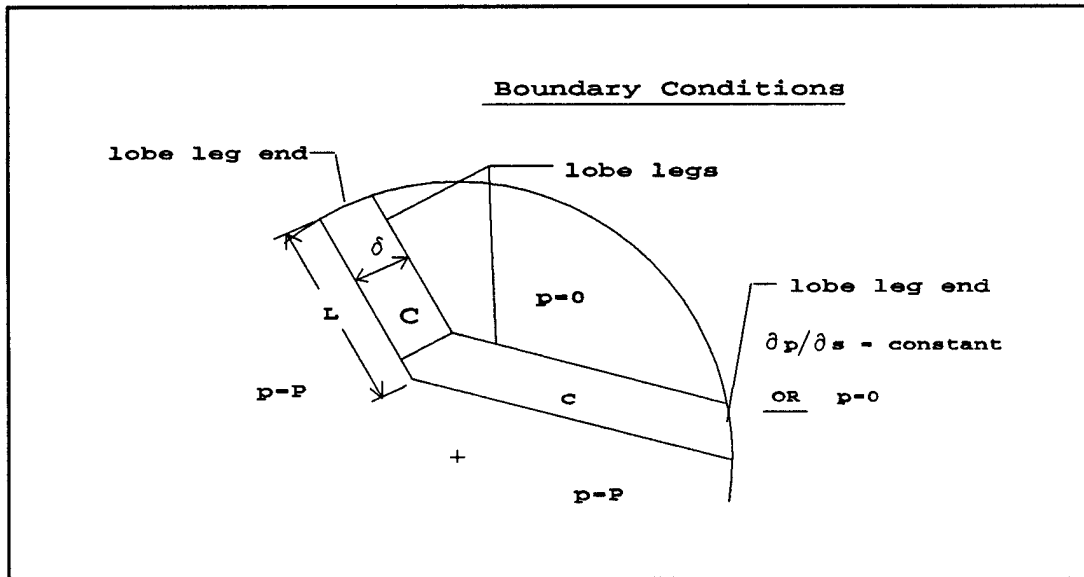


Figure 15 Boundary Conditions For FEM Model

that there is no flow across these boundaries. This is known as an insulated boundary condition and is what the equations model. The insulated boundary describes ideal, or optimal, boundary conditions for the pump. Any flow that does cross this boundary is a loss which would make the pump less than ideal. By defining these essential boundary conditions around the entire boundary, there are no boundaries where there is a forced flow (q_B) and, thus, there are no non-essential boundary conditions.

Once the pressure field is solved, the flow was calculated for a particular node using

$$\{Q_i\} = [k_e]\{P_i\} \quad i=1,2,3$$

where $[k_e]$ is the elemental stiffness matrix and Q_i and P_i are the flow and pressure

for node i of a triangular element. For example, the nodal flow for the node shown in Figure 16(a) for element number 1 is the flow that crosses the double lined boundary. To calculate the flow across the double lined boundary in Figure 16(b), the nodal flows from elements number 1, 2, and 3 for the node of interest are added together. Flow across a line containing many nodes can be calculated by adding together the nodal flows corresponding to the nodes which lie along the line. The flow calculated for comparison to the equations was the flow that crossed the

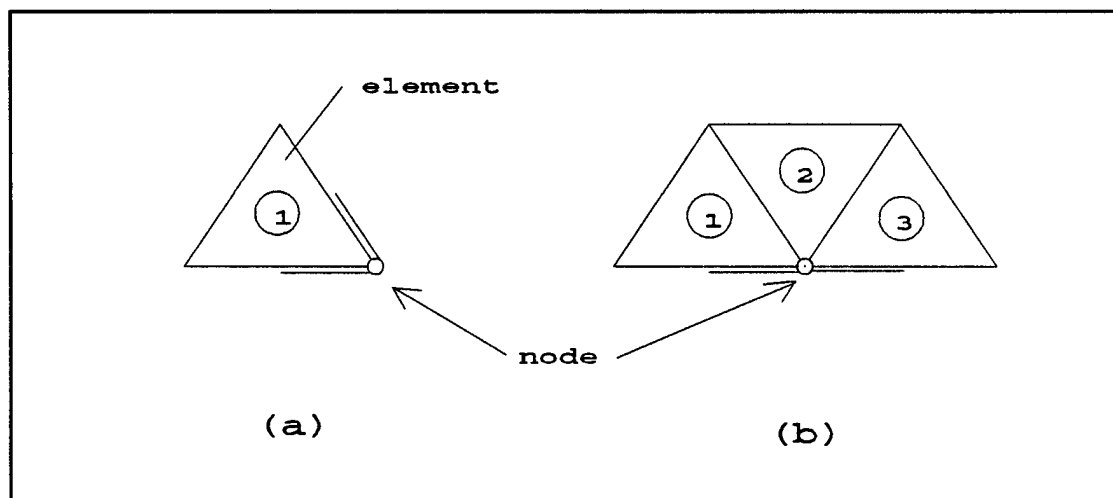


Figure 16 Boundaries Corresponding to Nodal Flows

boundary where $p=P$.

The FEM model was solved for a range of n , δ/R_o and L/R_o values. A FORTRAN program was written to generate V-lobe geometry key points and define mesh generating parameters for input to ANSYS². ANSYS was used solely to

²ANSYS is a registered trademark of Swanson Analysis Systems

generate the mesh and output the resulting nodal coordinates and element definitions. Another FORTRAN program was written to read the ANSYS output, decide which nodes had which boundary conditions and then put all the node, element and boundary condition information into files. The FEM program included in Appendix C then used these files to solve the problem under investigation. All programming was done on a COMPAQ 386/20 microcomputer. Figure 17 shows a typical lobe mesh generated by ANSYS. The number of elements varied slightly from case to case due to mesh generation decisions made by ANSYS. Approximately 100 elements produced a converged solution.

Table 4 compares the Poiseuille flow predicted by the equations to the flow predicted by the FEM model. The results confirm that the equations used to model

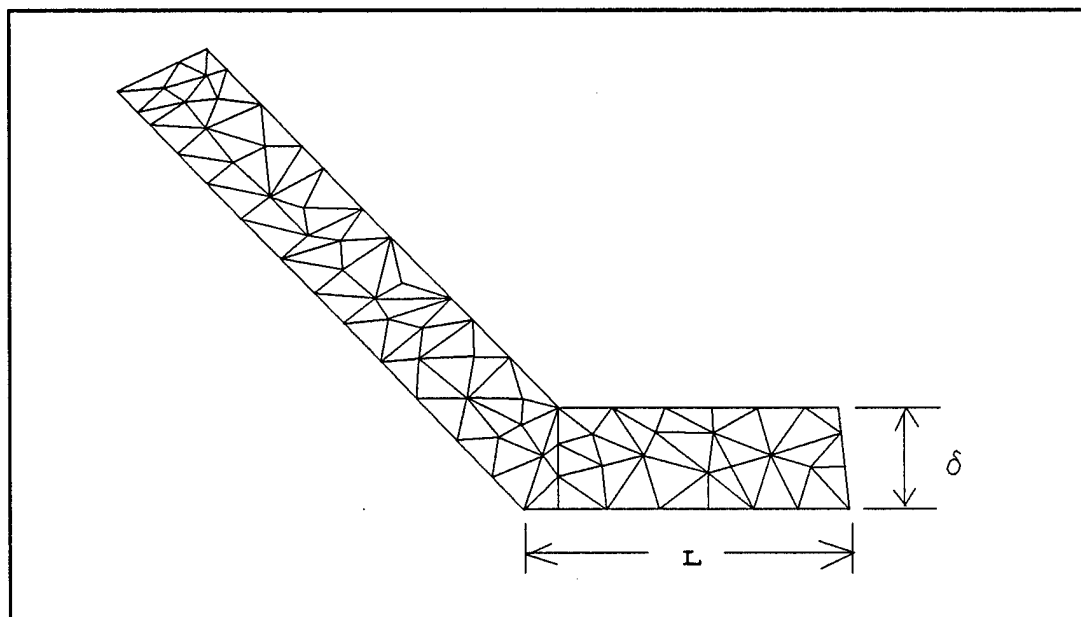


Figure 17 Typical Mesh Generated For V-lobe Geometry by ANSYS

Table 4 Comparison Of Equations To FEM Model (Poiseuille Flow)

Poiseuille Flow: $Q_{\text{EQUATIONS}}/Q_{\text{FEM}}$			
	n	$L/R_o=0.9$	$L/R_o=0.6$
$\delta/R_o=0.1$	3	0.987	0.983
	4	0.984	0.982
	5	0.983	0.983
	7	0.990	0.976
	12	0.983	0.966
$\delta/R_o=0.25$	3	0.974	0.965
	4	0.968	0.957
	5	0.963	0.942
	7	0.964	0.932
	12	0.735	*
$\delta/R_o=0.4$	3	0.966	0.954
	4	*	0.919
	5	*	0.924
	7	*	*
	12	*	*

* Lobes cannot be configured in this geometry

the Poiseuille component of flow are appropriate. Although the equations yield flow values slightly less than the FEM model, the agreement is good and some of the difference can be accounted for. The FEM models slightly over predict the flow because the geometric form generated with ANSYS does not draw the leg ends as arcs; instead, a secant is drawn. This means that a given pressure difference is effective over a shorter distance which would yield higher flow rates. The equations approximate the arc in a less conservative model using perpendicular lines as was discussed in the shape factor section above. Also, although the equations assume insulated end conditions, the FEM model uses a $\partial p / \partial s = \text{constant}$ boundary condition which is only an approximation of an insulated boundary condition. In the FEM model, some flow losses do occur across the leg ends.

Note that as n , δ/R_o and L/R_o each increase, the agreement between $Q_{\text{EQUATIONS}}$ and Q_{FEM} decreases. This is acceptable, however, because the agreement between the equations and the FEM model is excellent for the full range of optimal values of n , δ/R_o and L/R_o encountered. For example, when $S' = 1 \times 10^{-3}$ and $n=3$, the optimized nonsymmetric V-lobe geometry (Table 3) is $\xi = \delta/R_o = 0.379$ (also, since $\alpha=0$, $L/R_o = 1.0$). For this geometry, Table 4 gives an approximate agreement of 0.97 between the equations and the FEM, which is highly acceptable. Looking at the optimized geometry in Table 3 again, higher n values are accompanied by smaller optimal δ/R_o and L/R_o values. When $S' = 1 \times 10^{-3}$ and $n=5$, the optimal δ/R_o and L/R_o are 0.284 and 1.0, respectively. The agreement between the equations and the

FEM model is still approximately 0.97.

Although the current FEM model and the equations agree well, alternate boundary conditions must be investigated. With reference to Figure 15, the boundary conditions of $p=P$ along the lower boundary and $p=0$ along the upper boundary will be maintained. The boundary conditions to be altered are the conditions at the end of the lobe legs.

For the pump built for the experiments, there is no physical barrier at the leg ends to prevent flow. This means that for the actual pump, the leg end conditions are not insulated. The rotor can draw fluid from the leg end region as well as along the upper boundary where $p=0$ (recall footnote number 1, page 49). It is possible, therefore, that in the actual pump, the pressure along these ends is $p=0$. This boundary condition represents a worst case condition for the pump since it maximizes losses across the leg end boundaries. This is the extreme opposite of the $\partial p / \partial s = \text{constant}$ boundary condition (an approximately insulated boundary condition) used by the equations and the previous FEM model which describe optimal pumps³. The FEM model was solved with this new boundary condition of $p=0$ along the leg ends. Table 5 lists the ratio of the flow losses based on the $p=0$ condition along the leg ends to the flow based on the $\partial p / \partial s = \text{constant}$ condition along the leg ends for the $n=3$ lobe case. The deviation is significant, particularly at large δ/R_o and small

³ At the time of design and construction of the pump, this disadvantage was not known, so the pump tested is not ideal.

Table 5 Comparison of FEM Models ($FEM_{p=0}$ and $FEM_{\partial p/\partial s = \text{constant}}$)

Poiseuille Flow (losses): $Q_{(p=0)}/Q_{(\partial p/\partial s = \text{constant})}$		
δ/R_o	$L/R_o = .9$	$L/R_o = .6$
.1	1.131	1.159
.25	1.305	1.431
.4	1.516	1.775

L/R_o . If the $p=0$ condition along the leg ends is the more representative model of the physical phenomenon in the pump, then the previous equations will noticeably underestimate the Poiseuille flow (pumping loss) that actually occurs. Although there is uncertainty in the leg end boundary condition, the analysis at this stage will proceed with the $\partial p/\partial s = \text{constant}$ condition. Thus the comparison will be made on the optimal pumping condition for each configuration.

3.4 Comparison of Lobe Designs

3.4.1 Complete Optimal Case

Based on the FEM investigation above, we see that the flow equations for the semicircular lobe and the two V-lobe designs are based on optimal boundary conditions (insulated).

Following this line of thought, it is of interest to compare the complete optimal case for each of the lobe designs. The complete optimal case occurs when

the pump has the insulated boundary conditions described above and is operated at zero clearance. This condition represents the upper limit of pump performance. Practically speaking, it would not be a good idea to run the pump at zero clearance because here the stator lobes and rotor are in full contact. It is insightful, however, to see which lobe design has the greatest potential which is represented by the complete optimal case.

The complete optimal case will be compared for the semicircular design and the nonsymmetric V-lobe design. The symmetric V-lobe design is excluded because it is equivalent to the nonsymmetric V-lobe (with a minor difference of where the step is placed) when $\alpha = 0^\circ$. Recall that the optimization yielded $\alpha = 0^\circ$ for both the nonsymmetric and the symmetric V-lobe.

The equations to be optimized for the $c=0$ (zero clearance) case must be altered slightly from the previous optimization. This is because nondimensionalizing s by c ($\sigma = s/c$) is no longer appropriate. Instead, s is nondimensionalized by R_o :

$$\sigma_{c0} = \frac{s}{R_o} \quad (60)$$

S'_{c0} , a new version of the operation conditions parameter, S' , is defined as follows:

$$S'_{c0} = \frac{\pi}{12} \frac{P}{\mu \omega} \quad (61)$$

A new dimensionless flow, Q'_{c0} is defined from

$$Q_{c0} = \frac{1}{2} \omega R_o^3 Q'_{c0} \quad (62)$$

where Q_{c0} is the flow, Q , when the clearance is zero. Using these definitions, the dimensionless equation for flow at $c=0$ is

$$Q'_{c0} = \frac{\sigma n}{2} [1 - (F_n + \xi)^2] + S'_{c0} \sigma_{c0}^3 \frac{(n-2)}{\ln\left(1 - \frac{\xi}{\tan\beta}\right)} \quad (63)$$

for the semicircular lobe (from Equation (17)), and

$$Q'_{c0} = \frac{\sigma_{c0} n}{2} \left[1 - \xi^2 - \left(\frac{\sin\alpha}{\sin(\alpha+2\beta)} + \frac{\xi}{\tan\psi} \right)^2 \right] - S'_{c0} \frac{2n}{\pi \xi} \sigma_{c0}^3 \left[1 - \frac{\xi}{\tan\psi} - \frac{\sin\alpha}{\sin(\alpha+2\beta)} \right] \quad (64)$$

for the nonsymmetric V-lobe (from Equation (39)).

These equations were optimized using the path of steepest descent method. Table 6 shows a representative comparison of the results of the optimization. The V-lobe design outperforms the semicircular design for the complete optimal case. Note that the optimal geometry occurs at $n=5$ for the semicircular lobe while Q_{c0}' continues to increase with n for the V-lobe. Also note that the V-lobe outperforms the semicircular lobe by the same amount for any operating conditions at a given n .

The corresponding values of ξ and σ_{c0} (dimensionless lobe width and step height) for each n value are not included in the table, but are worth mentioning. As

it turns out, the value of the lobe width, ξ , is not dependent upon the operating conditions, S'_{c0} . For each of the lobe designs, the optimal ξ is constant for any operating conditions at a given n . This value decreases as n increases. The optimal value of σ_{c0} , however, is a function of the operation conditions. As S'_{c0} decreases, the optimal σ_{c0} increases. The optimal σ_{c0} also decreases as the number of lobes increases. The optimal value of α was zero degrees as in the previous optimization as expected.

Table 6 Optimal Pumping Comparison For Complete Optimal Case

S'_{c0}	n	$Q'_{c0\text{semic}}$	$Q'_{c0\text{v-lobe}}$	$Q'_{c0\text{v}} / Q'_{c0\text{s}}$
1×10^{-6}	3	5.526	8.206	1.48
	4	5.654	10.499	1.86
	5	5.678 *	12.389	2.18
	6	5.642	14.010	2.48
	7	5.572	15.442	2.77
	8	5.484	16.736	3.05
1×10^{-3}	3	174.8	259.5	1.48
	4	178.8	332.0	1.86
	5	179.6 *	391.8	2.18
	6	178.4	443.0	2.48
	7	176.2	488.3	2.77
	8	173.4	529.2	3.05

* Designates maximum flow

3.4.2 Practical Optimal Case

Three lobe configurations were investigated, namely the semicircular lobe, the symmetric V-lobe (using two different length models, l' and l) and the nonsymmetric V-lobe. A comparison of the optimal Q' values obtained for the straight leg lobes (symmetric and nonsymmetric V-lobes) to the values obtained for the semicircular lobes revealed that the straight leg lobes appear to be superior to the semicircular lobes in all cases based on the optimization results in Tables 1, 2 and 3. The investigation of the upper limit of pump performance based on the complete optimal case also revealed that the V-lobes have greater potential than the semicircular lobes.

This point is not so obvious, however, when a closer look is taken at the optimal values of α obtained for the V-lobe designs. In all cases, the optimal value of α was zero degrees. This means that the lobes are contiguous and there is no room in the center of the pump for the fluid to enter and exit. The angle α must be greater than zero so that fluid can enter the inside of the pump and exit through the hole at the center of the stator (see Figure 1). As α gets larger, however, the maximum value of Q' based on the optimization decreases. A check had to be made to ensure that, even when α takes on a physically reasonable value that allows the fluid to enter the center of the pump, the V-lobe designs still outperformed the semicircular lobe. When $\alpha=0$, the symmetric V-lobe geometry is the same as that of the nonsymmetric V-lobe (with a minor difference of where the step is placed) and therefore the optimal Q' values are equal. The investigation of a practical angle

α will shed light on the matter of which V-lobe design is better. This is, therefore, the study of the practical optimal case.

A true test for determining which configuration is superior is to compare Q' for a prescribed size of the hole at the center of the stator through which the fluid exits. This is accomplished by determining values of α which correspond to this exit hole size and then optimizing the equations based on this given α . A generous exit hole radius (nondimensionalized by R_o) of 0.2 was selected. Table 7 lists a comparison of the optimal Q' value for the semicircular lobe, the symmetric V-lobe (using the length l') and the nonsymmetric V-lobe for a large S' (1×10^{-3}) and a small S' (1×10^{-6}) for the case where an exit hole in the stator of radius $0.2 \times R_o$ exists. Table 7 proves that the nonsymmetric V-lobe design provides the most efficient pumping mechanism even when a practically sized exit hole is accounted for. Since the nonsymmetric V-lobe is theoretically superior to the symmetric V-lobe, there is no need for further investigation of the symmetric V-lobe. The term 'V-lobe' will subsequently refer solely to the nonsymmetric V-lobe.

3.4.3 Pumping Performance Based on Experiment Conditions

Having compared the theoretical nondimensional flow, Q' , based on the optimized geometries of the lobe designs, the next step is to compare the theoretical pumping performances of the lobe designs for actual test conditions.

The test conditions used in the experiments, which are described in more detail later in Section 4.2, correspond to an operating conditions parameter of

Table 7 Optimal Pumping Comparison For Practical Exit Hole Size

S'	n	Q'		
		Semicircular lobe	Symmetric V-lobe (l')	Nonsymmetric V-lobe
1×10^{-6}	3	173.66	194.62	233.46
	4	177.54	261.00	300.07
	5	178.18	317.38	350.22
	6	176.94	366.06	393.42
	7	174.65	409.12	432.09
	9	171.81	447.74	467.36
1×10^{-3}	3	4.443	5.059	6.315
	4	4.407	6.831	8.067
	5	4.310	8.295	9.337
	6	4.180	9.520	10.393
	7	4.036	10.570	11.304
	8	3.888	11.481	12.108

approximately $S' = 1 \times 10^{-3}$. Based on this operating conditions parameter, optimal geometry was selected for each lobe design.

For the semicircular lobe design, this corresponded to $\xi = 0.273$, $\sigma = 6.79$, and $n = 3$ for maximum pumping efficiency according to the optimized geometry presented in Table 1. Based on the physical dimensions of the pump ($R_o = 55$ mm), the optimal lobe width, $\delta = \xi R_o$, is 15 mm, and the optimal step height, $s = \sigma c$, is 100 μm . The step height value is based on a clearance, c , of 15 μm since this was the original average value selected at which to run the tests. Although an average value of 12 μm was later selected, the step height is still appropriate because the tests were operated in the range of 15 μm .

In the case of the V-lobe, for a given S' (in this case, 1×10^{-3}), there is no optimal n value. The pumping capability, Q' , continues to increase as n increases. For the experiment, a value of $n = 3$ was selected so that the two lobe designs could be more directly compared. Although the optimization points to using higher values of n , the lower end value of $n = 3$ should still theoretically outperform the three lobe semicircular design. Although the optimization also shows that maximum pumping efficiency occurs where $\alpha = 0^\circ$, this is not a physically realistic situation as discussed earlier. An $\alpha = 12^\circ$ was selected since this allows sufficient room for the fluid to exit through the center of the pump. For $S' = 1 \times 10^{-3}$, $n = 3$, and $\alpha = 12^\circ$, the optimized geometry yields $\sigma = 9.25$ and $\xi = 0.323$. Based on the pump's physical dimension of $R_o = 55$ mm and the discussion above concerning the calculation of the step height,

the lobe thickness is $\delta = 17.8$ mm and the step height is $s = 136$ μm .

The procedure for the experiments was to run the pump at three different clearances (8, 12 and 16 μm) and three different speeds (600, 1200 and 1800 rpm). A comparison between the theoretical pumping capabilities of the two pump designs for these test conditions are shown in Figures 18, 19 and 20 for the 8, 12 and 16 μm clearances, respectively. The flow versus pressure relationship is linear as expected. The V-lobe design outperforms the semicircular lobe design in all cases, particularly at high flow rates. The maximum pressure theoretically capable of being developed (i.e., the pressure at zero flow) is approximately equivalent for both designs. This occurs because the optimal geometries were selected for both designs based upon the same S' (1×10^{-3}). They are not exactly equal because the lobe geometry is not exactly the optimized values. Instead, the lobe dimensions are the resulting machined dimensions of the optimized lobe geometry.

The V-lobe design is thus theoretically superior to the semicircular design. The next step is to run tests on each design to see which one performs better in practice.

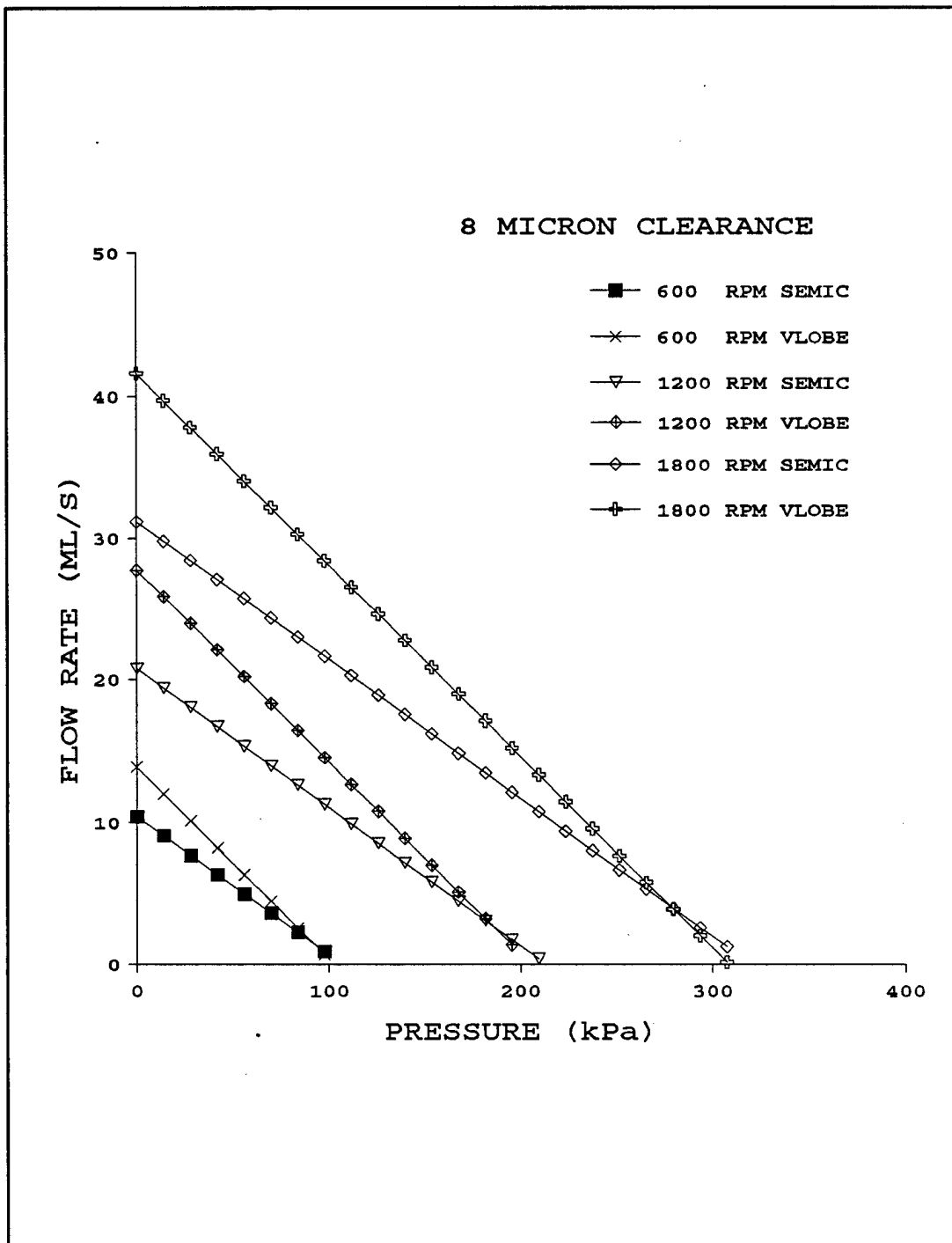


Figure 18 Comparison of Theoretical Pumping Capacities for Semicircular Lobe and V-lobe (Test Conditions, $8\mu\text{m}$)

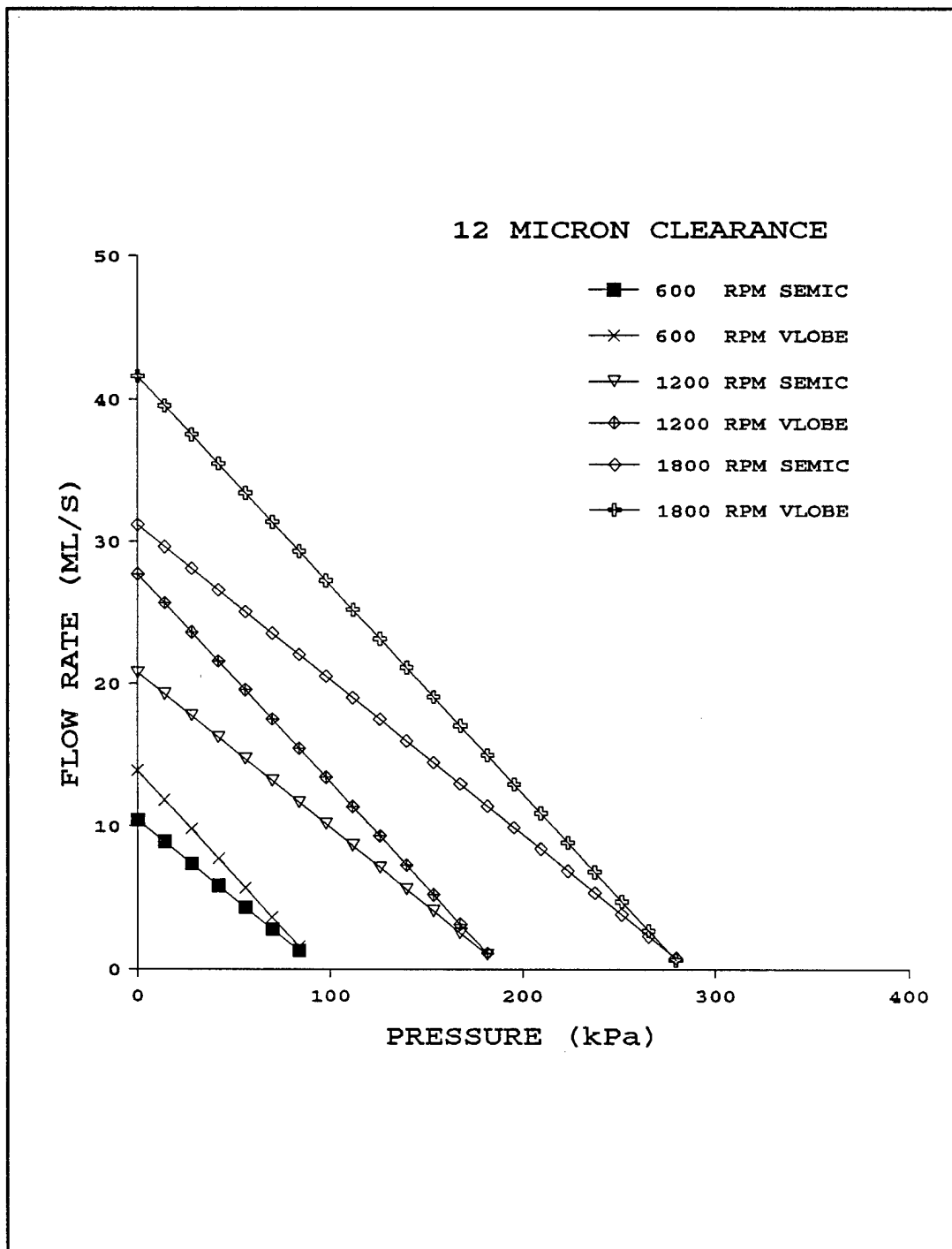


Figure 19 Comparison of Theoretical Pumping Capacities for Semicircular Lobe and V-lobe (Test Conditions, 12 μm)

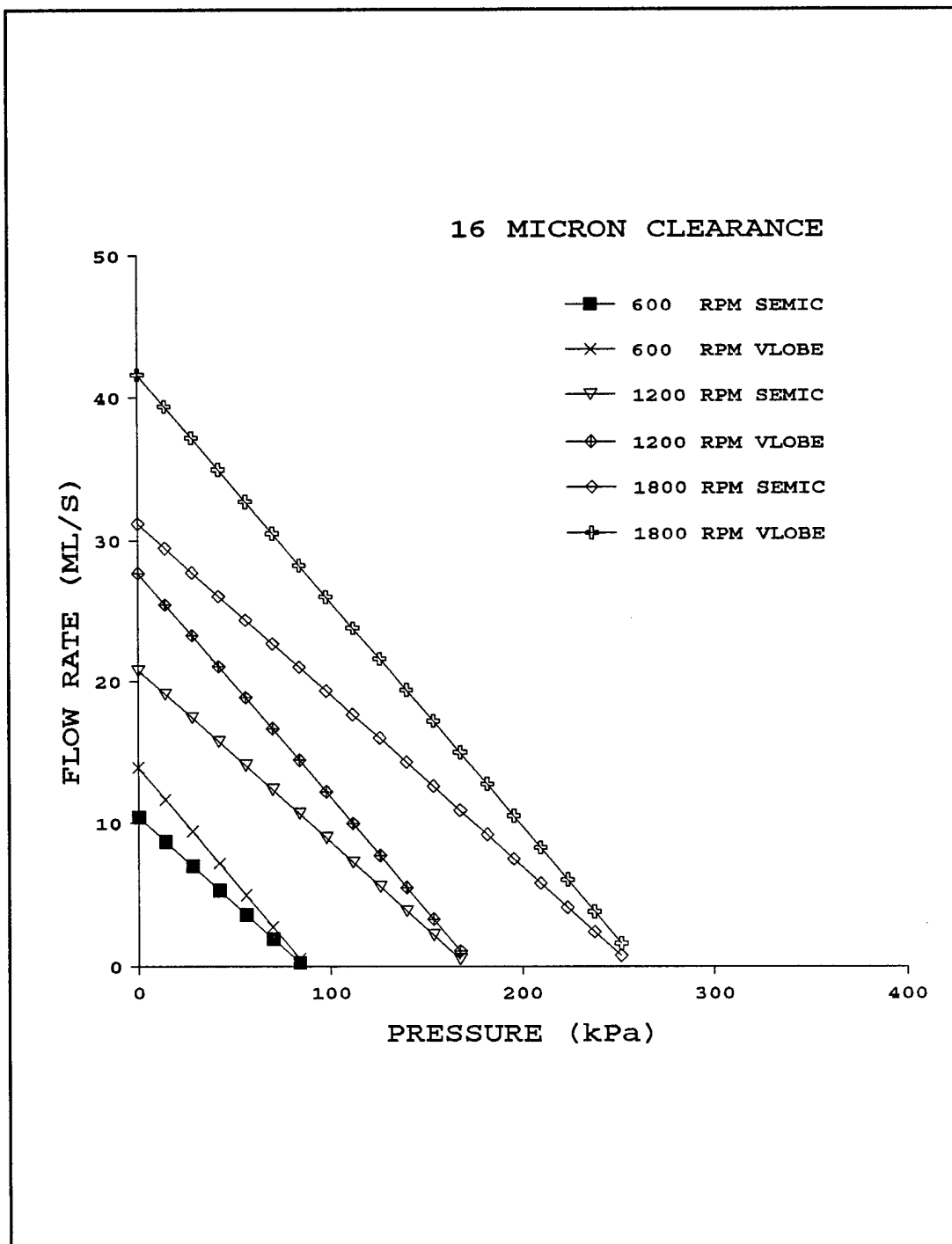


Figure 20 Comparison of Theoretical Pumping Capacities for Semicircular Lobe and V-lobe (Test Conditions, 16 μm)

CHAPTER IV

EXPERIMENT SETUP

4.1 Equipment and Apparatus

The test rig consists of the pump itself and the flow loop apparatus. A sketch of the entire pump is shown in Figure 21. The three lobes (6) are attached to the stator (3) with six bolts (18). The stator housing, which is comprised of several parts, is attached to the rotor housing (7) by eight bolts (4). The position of the stator relative to the rotor (15) is maintained by applying back pressure (air) through the air inlet (16). The fluid to be pumped (the process fluid) enters at (17) and exits through the hole in the stator (20). A bleeder is placed at the top of the pump at location (14) for the purpose of priming the pump. The pressurized air and process fluid are sealed by diaphragms (5) which allow the stator to be flexibly mounted. The rotor shaft (13) is supported by ball bearings (12) which are lubricated with oil (9). This lubricating oil is sealed by lip seals (10) and a gasket (11). The rotor housing (and the motor) are attached to the base (8).

Three proximity probes (2) are placed so that the clearance between the rotor and stator can be read directly. Two thermocouples (1) are located on both sides of the lobes to measure the temperature of the process fluid before and after being sheared between the rotor and the lobes. Two pressure transducers (19) are located

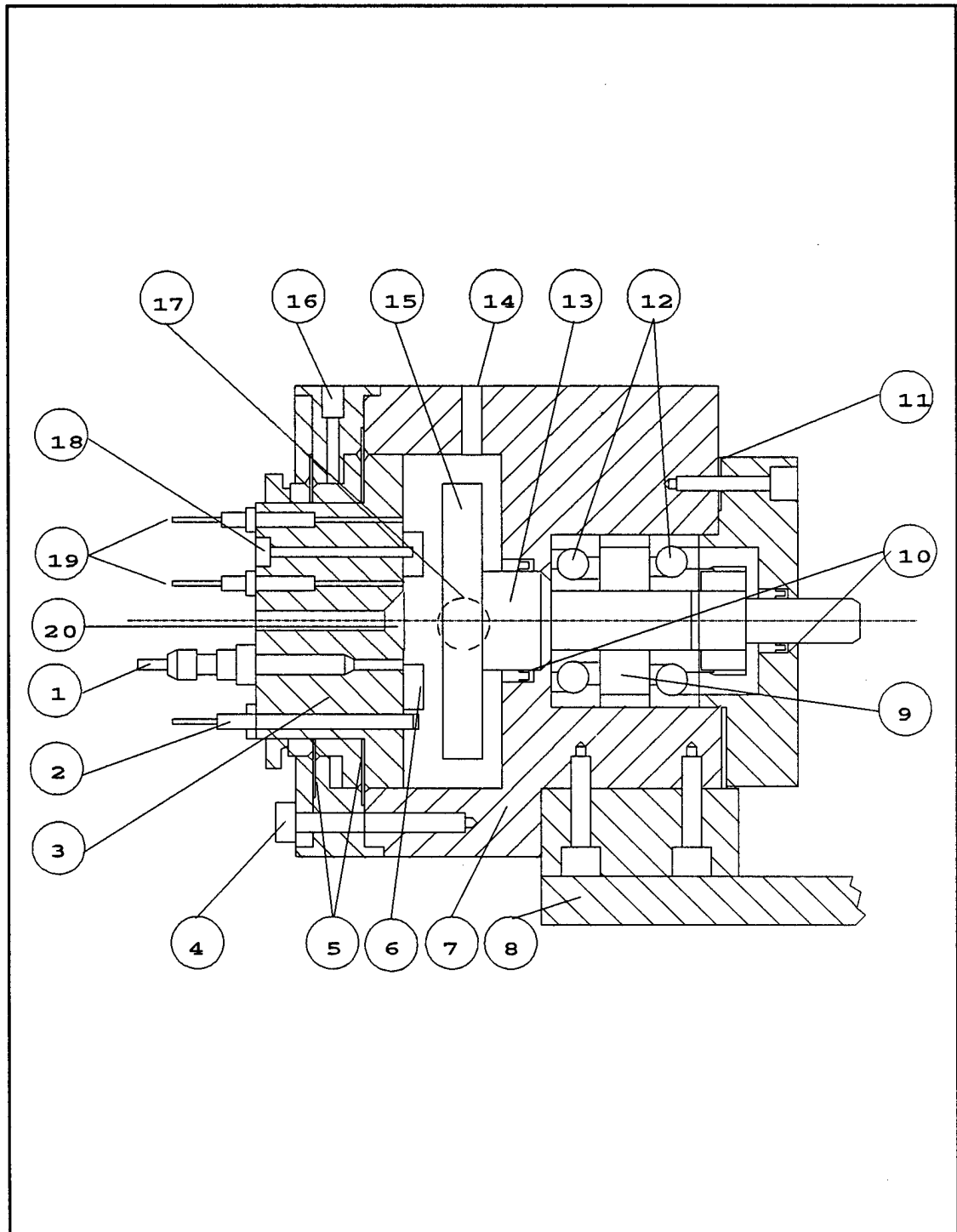


Figure 21 Pump Assembly

on both sides of the lobes to measure the pressure developed in the process fluid before and after being pump. The locations of the probes on the stator are shown in Figure 22. The outer radius of the rotor, R_o , is 55 mm (2.16 in.). The dimensions of the semicircular lobes and the V-lobes are the optimized values presented in section 3.4.3.

The pump design explained above was selected only after careful consideration had been given to the design of the pump investigated by Green et al., (1989). The main point learned from this was to measure the pertinent test variables directly. This means that the clearance between the rotor and stator needed to be measured by proximity probes on the stator facing the rotor. Since the analysis

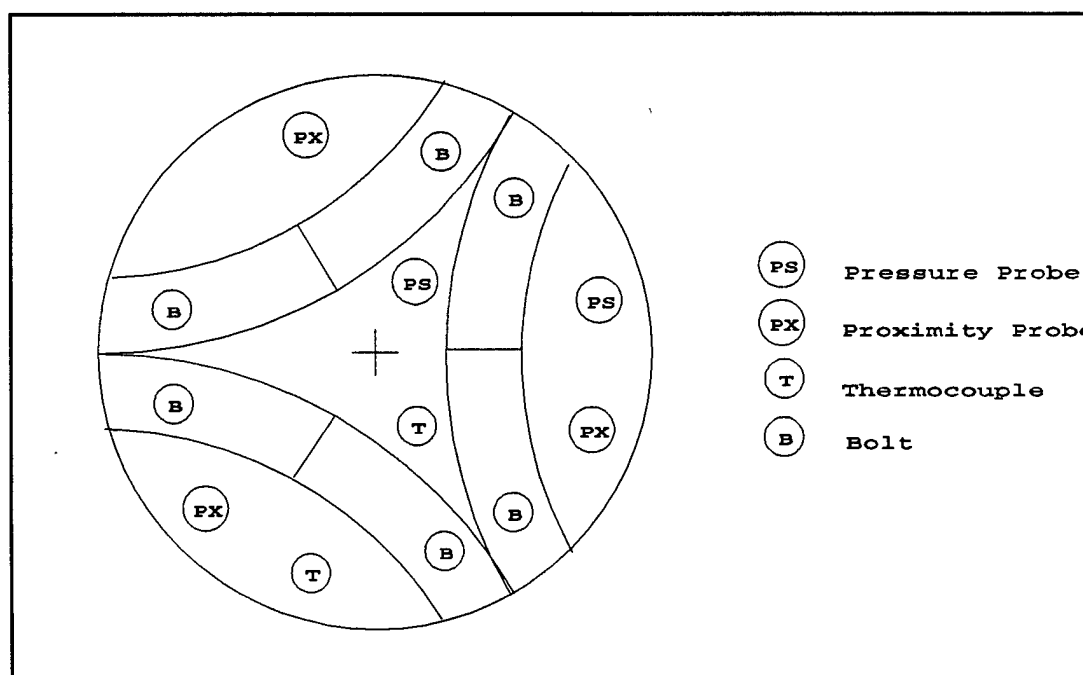


Figure 22 Front View of Stator

models the differential pressure across the lobes, pressure transducers needed to be placed on both sides of the lobes. Additionally, the process fluid temperature needed to be measured where it is being sheared inside the pump.

The complete test rig flow loop is shown in Figure 23. The process fluid (mineral oil) is supplied from a reservoir placed 1.5 meters above the pump to help prime the pump. Also, as mentioned earlier, a bleeder was placed in the pump to help prime the pump. This point was also learned from Green et al. (1989). All the tubing shown in Figure 23 is 9.525 mm (3/8 in.) plastic tubing. The fluid flows from the reservoir, through the filter and into the pump. In the pump, the rotor is driven by a 2 hp DC feedback motor with a digital rpm display. The fluid is pumped and exits through the stator. A simple dial pressure gauge was placed in the flow line at the stator exit to verify the pressure transducer readings. The flow rate is regulated by a needle valve placed after the pressure gauge. Rotameters placed in the flow line measure the volumetric flow rate. After passing through the rotameters, the fluid is recirculated to the reservoir. Fluid temperature was adjusted using a simple copper coil heat exchanger placed in the oil reservoir through which tap water was run. An OMEGA DAS-16 data acquisition board with software (STREAMER) was used to obtain the proximity probe and amplified pressure transducer voltage signals. An IBM AT⁴ computer was used to process all data.

⁴ IBM AT is a registered trademark of International Business Machines

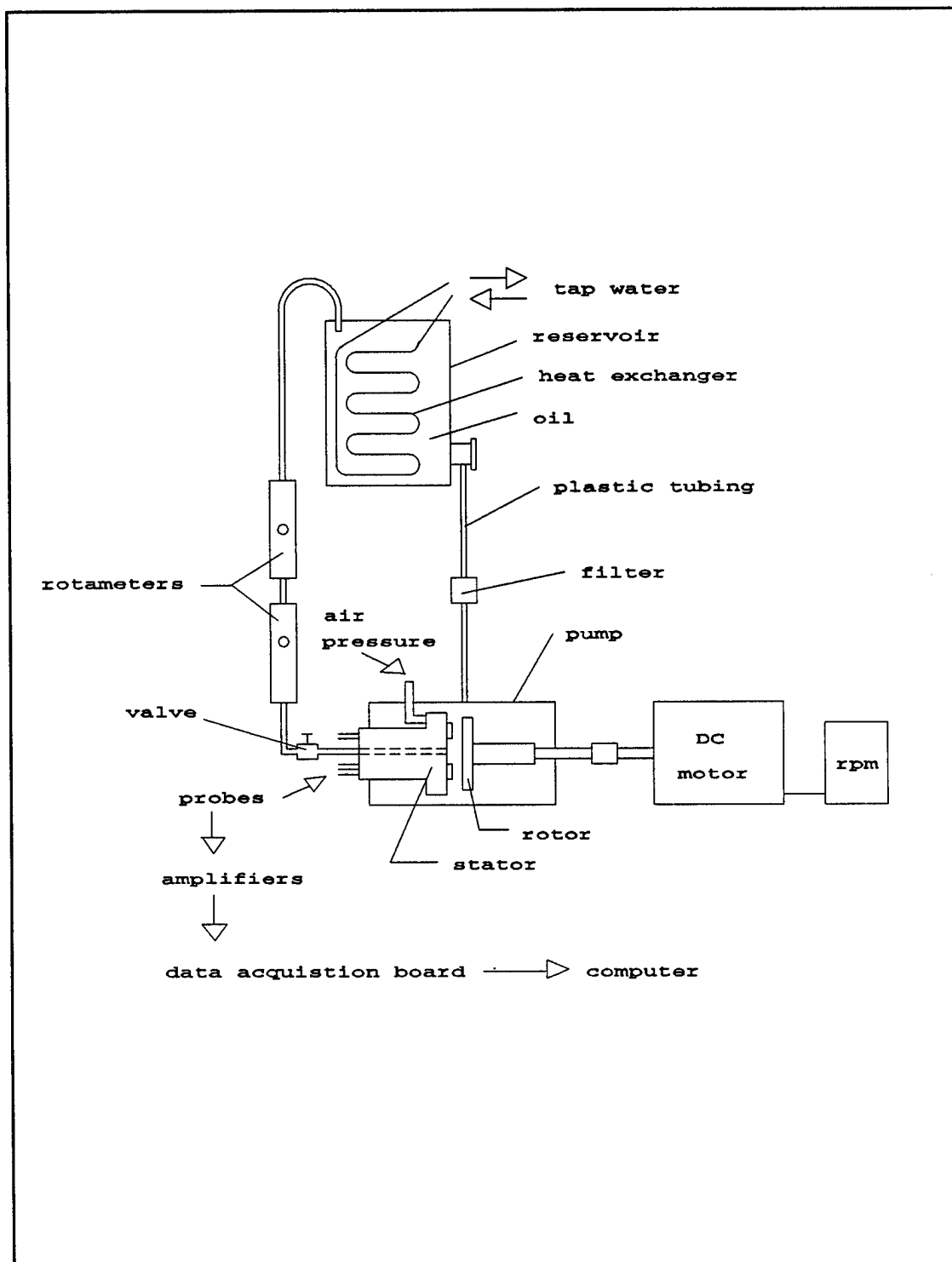


Figure 23 Test Rig

4.1.1 Calibrations

The measuring equipment was calibrated to ensure accurate measurements were taken. Calibration checks were also performed through the course of the experiments to check that the equipment was operating as expected.

The proximity probes were Bentley Nevada type 21500-00-24-10-02. They were used to measure the distance between the rotor and stator. The calibration was done in situ, i.e., they were placed in their location on the stator. The voltage output from the probes was recorded as the stator was pulled a measured distance away from the rotor. This distance was measured using a dial indicator placed at the back of the stator. The distances and corresponding voltages were used to generate a calibration curve. Note that it is only the slope of this curve that is important for measuring relative distances. It is important to check that the probes are operating in their linear range. The calibration procedure was repeated two to three times for each probe and produced repeatable data. The resulting calibration constants (with units of mm/mV) corresponded closely to the approximate value predicted by the manufacturer.

The pressure transducers were Kulite model XTM-190-100 with piezoresistive active half bridge sensors. Each transducer was individually calibrated by the manufacturer and comes with a calibration constant (with units of mv/psi). The transducer signal was amplified using Electro Instruments Model A16 DC differential amplifiers. These amplifiers were calibrated for a set gain by measuring the input

voltage (supplied by a frequency generator) and the output voltage and then calculating the gain. Calibration checks were also performed in situ. Here, the input voltage from the pressure transducers was measured as was the amplified output voltage. The gain was calculated for the full range of input voltage values (supplied by the pressure transducers) to make sure that the gain was constant and the amplifiers did not saturate.

Two rotameters were used: one (type OMEGA FL-114) to measure relatively low to medium flow rates and one (type OMEGA FL-115) to measure relatively high flow rates. The operating principle behind a rotameter, also known as a variable area meter, is a force balance between the pressure drop across the ball, the shearing force of the fluid on the ball, the weight of the ball, and the buoyancy force of the ball in the fluid. The calibration of the scale on the rotameter, which indicates the vertical height of the ball in a variable area duct, is therefore dependent on the viscosity and density of the fluid. The calibration was done at two temperatures. The basic technique was to collect a measured amount of fluid in a graduated cylinder over a measured period of time. At the same time, the scale reading on the rotameter was recorded as was the temperature. Thus, a scale reading versus volumetric flow rate curve was generated for each of the two temperatures. The flow rate corresponding to any other temperature than the two calibration temperatures is assumed to be a linear interpolation of the calibrated flow rates.

The thermocouples were OMEGA Model 650 type J. They were

supplemented with their own compensation unit and digital readout.

The properties of the fluid (Shell Tellus 10 Mineral Oil) also had to be measured. The kinematic viscosity and specific gravity of the oil were measured for two temperatures (23.5°C and 74.8°C) using a viscometer and a hydrometer. The absolute viscosity, μ , of the oil was then calculated for each temperature, T. An absolute viscosity-temperature curve was then generated by assuming a log-log linearity relationship between μ and T (Shigley and Mitchell, 1983). This relationship reduces to the form $\mu = bT^a$ where a and b are constants determined from the known (μ, T) points. The measured property values of the oil are shown in Table 8.

Table 8 Properties of Shell Tellus 10 Mineral Oil

T (°C)	Specific Gravity H ₂ O, 15.6°C	Kinematic Viscosity m ² /s x10 ⁻⁶	Absolute Viscosity Pa•s x10 ⁻³
23.5	0.868	16.63	14.42
74.8	0.836	3.682	3.075

4.2 Procedure

The experimental procedures for testing the semicircular lobe design and nonsymmetric V-lobe design were identical. The semicircular lobes were tested first

and were then replaced (on the stator) by the V-lobes. The basic format of the experiments was to run the pump at a certain clearance, speed and temperature and then measure pressure and flow rate for the range from zero flow to full flow. The data thus generates a system curve (Q versus P) for given clearance, speed and temperature. For the experiments, operating speeds of 600, 1200 and 1800 rpm and clearances of 8, 12 and 16 μm were selected. All test cases were run at 31.5°C with the exception of two test cases run at 25.0°C to investigate the effect of temperature.

Taking each set of data involved several steps for each point in the set. A set of data points consists of the flow, pressure, and temperature for a given clearance and speed (test case) over the full range from zero flow (valve closed) to full flow (valve fully open). Before taking each set of data, the stator was placed in contact with the rotor by the force of the back pressure. This was assumed to correspond to zero clearance. The data acquisition board was programmed using OMEGA's STREAMER software to take data for approximately 0.3 seconds. FORTRAN programs and batch files were written to convert the STREAMER output into voltages.

The next step was to run the motor at a given speed and apply a back pressure to the stator to maintain a given clearance. The valve was then turned to a position that resulted in flow between zero flow and full flow. The heat exchanger was adjusted until the average value of the two thermocouple readings was at the desired value $\pm 0.5^\circ\text{C}$. Once this state of operation appeared to be steady (none of

the readings were changing), STREAMER was again activated to take data for about 0.3 seconds of all probes in multiplex mode. During this time, the rotameter scale reading, temperatures, and motor speed were noted. FORTRAN programs and batch files were written to interpret this STREAMER data and the previous zero clearance (contact) data. The FORTRAN program then calculated the resulting clearances and pressures based on the voltage data using the calibration curves. If the resulting average clearance (the average of the 3 proximity probes) was $\pm 0.1 \mu\text{m}$ from the desired operating clearance, then the values for speed, temperature and rotameter scale reading were input to the program. The FORTRAN program then converted the rotameter scale reading into the corresponding flow rate and finally, the complete data point (clearances, pressure, speed, temperature and flow rate) was stored in a data file.

Since the data was taken over 0.3 seconds, each probe reading was taken to be the average reading over time. Also, the signal interpreted by the data acquisition board had occasional errant spikes. These spikes were filtered out by excluding any reading greater than 3 standard deviations away from the average reading. Out of 610 reading taken per probe in the 0.3 second interval, there would typically be 5-8 of these spikes for the pressure readings and 3-6 spikes for the proximity probe readings. The spikes were assumed to be erroneous representations of the measured property since the signal was otherwise constant (steady state).

The results of a set of data points represents a pointwise system curve (flow

as a function of pressure) for the given test case (speed, clearance and temperature).

The tests were run for each case 2-3 times (nonconsecutively) to ensure that the data was repeatable.

CHAPTER V

RESULTS AND DISCUSSION

5.1 Experimental Results With Comparison To Theory

For the experiments, operating speeds of 600, 1200 and 1800 rpm and clearances of 8, 12 and 16 μm were selected. All nine of these test cases were run for both the semicircular lobe design and the V-lobe design at a temperature of 31.5°C. Additionally, the 1200 rpm, 12 μm case was run at 25°C for each lobe design. The 600 rpm, 16 μm case constitutes the smallest pumping capabilities, the 1200 rpm, 12 μm (and 31.5°C) case is the average case, and the 1800 rpm, 8 μm case provides the highest pumping capabilities realized in the tests. Although all test cases were analyzed, these three test cases, which contain the full range of test cases, will frequently be used for presentation purposes. The test results for the 1800 rpm, 8 μm case, the 1200 rpm, 12 μm case and the 600 rpm, 16 μm case are shown in Figures 24, 25 and 26, respectively. These graphs show the experimental and theoretical (based on Equations (17) and (39)) results for both the semicircular lobe and the V-lobe. Before comparing the performance of the V-lobe to the semicircular lobe, it is necessary to check to see that the pump operating conditions corresponded to the operating conditions parameter, S' , that was used in the selection of the optimal geometry for both lobe designs. If the operating conditions result in

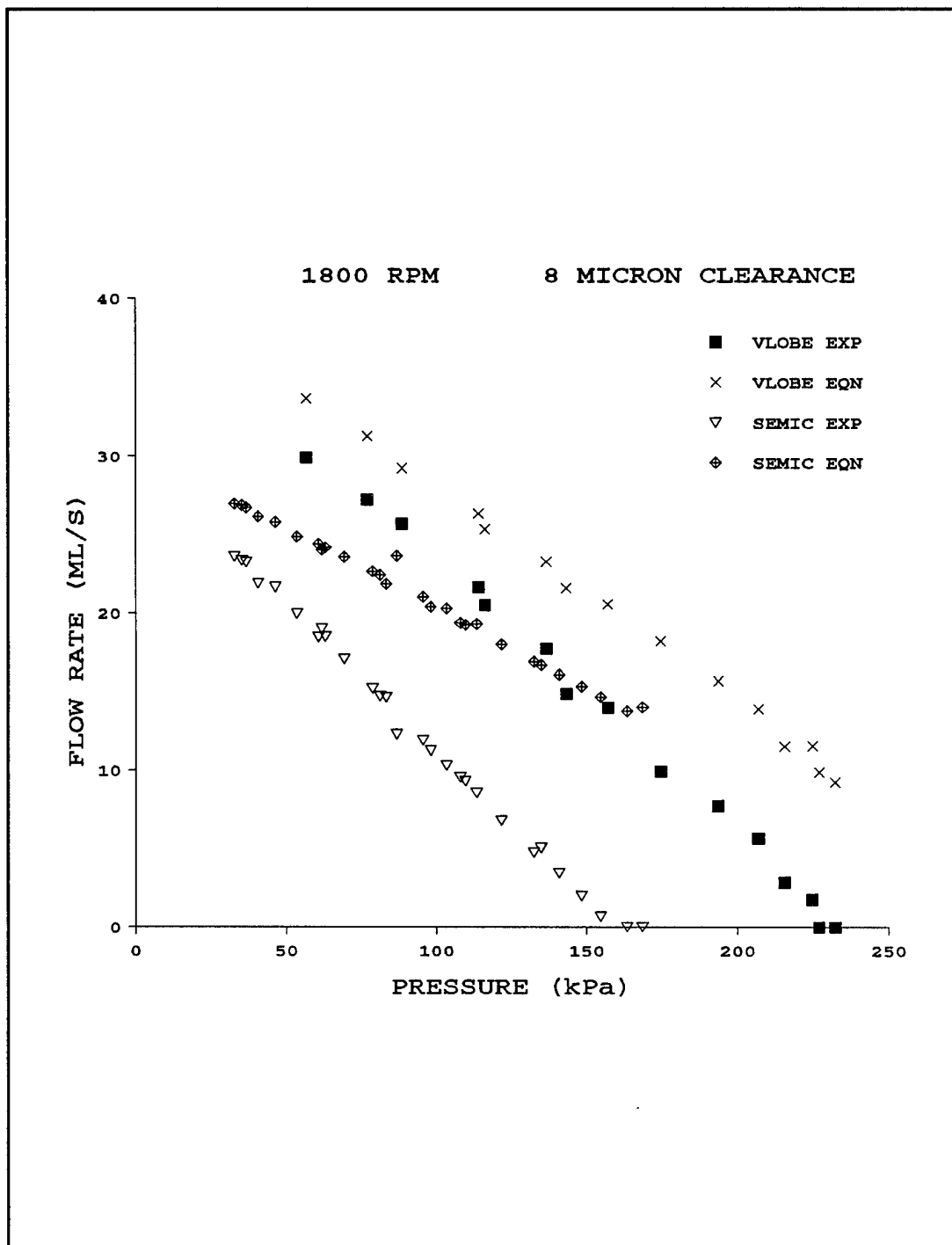


Figure 24 Experimental Results With Comparison to Theory (1800 r.p.m., 8 μ m)

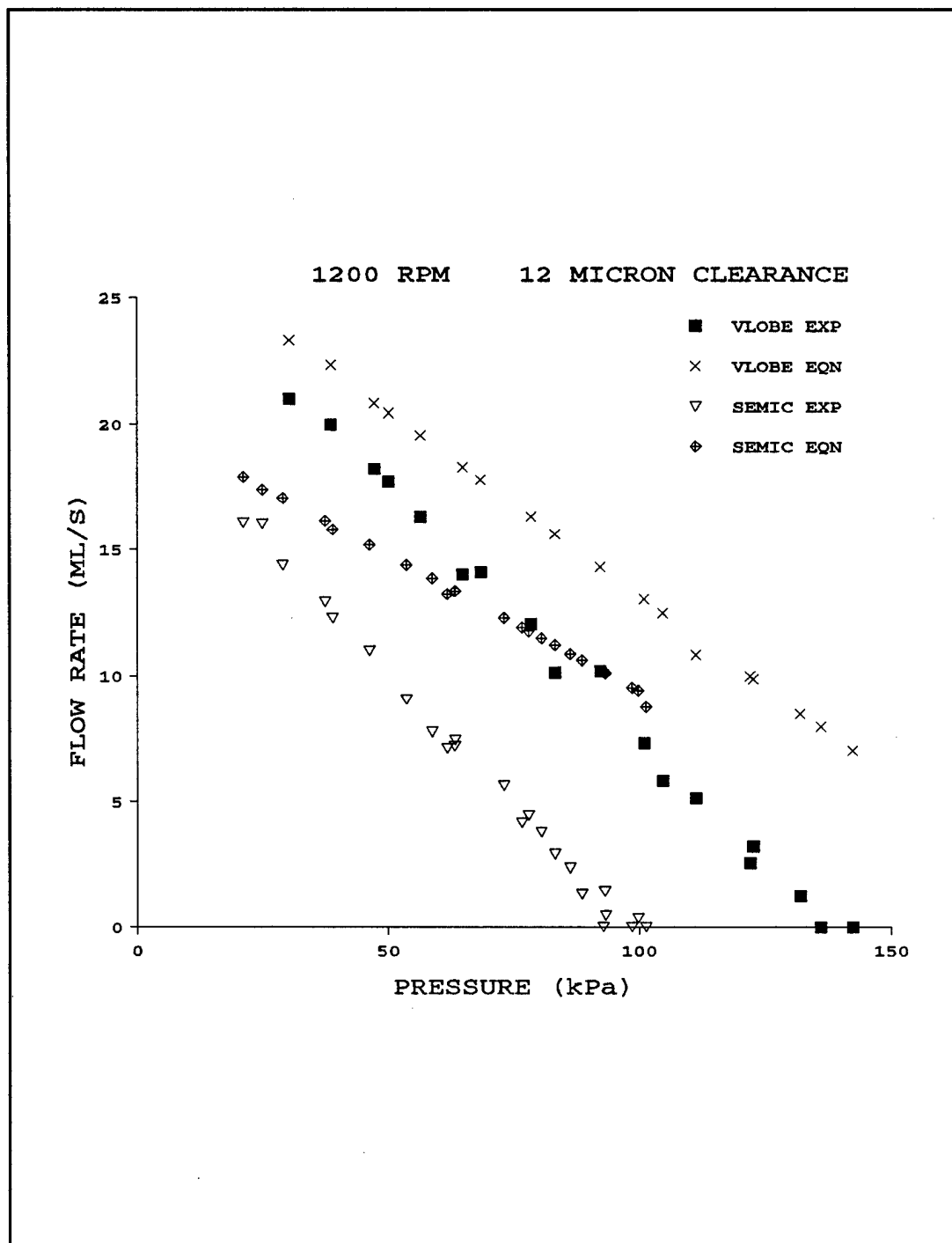


Figure 25 Experimental Results With Comparison to Theory (1200 r.p.m., 12 μm)

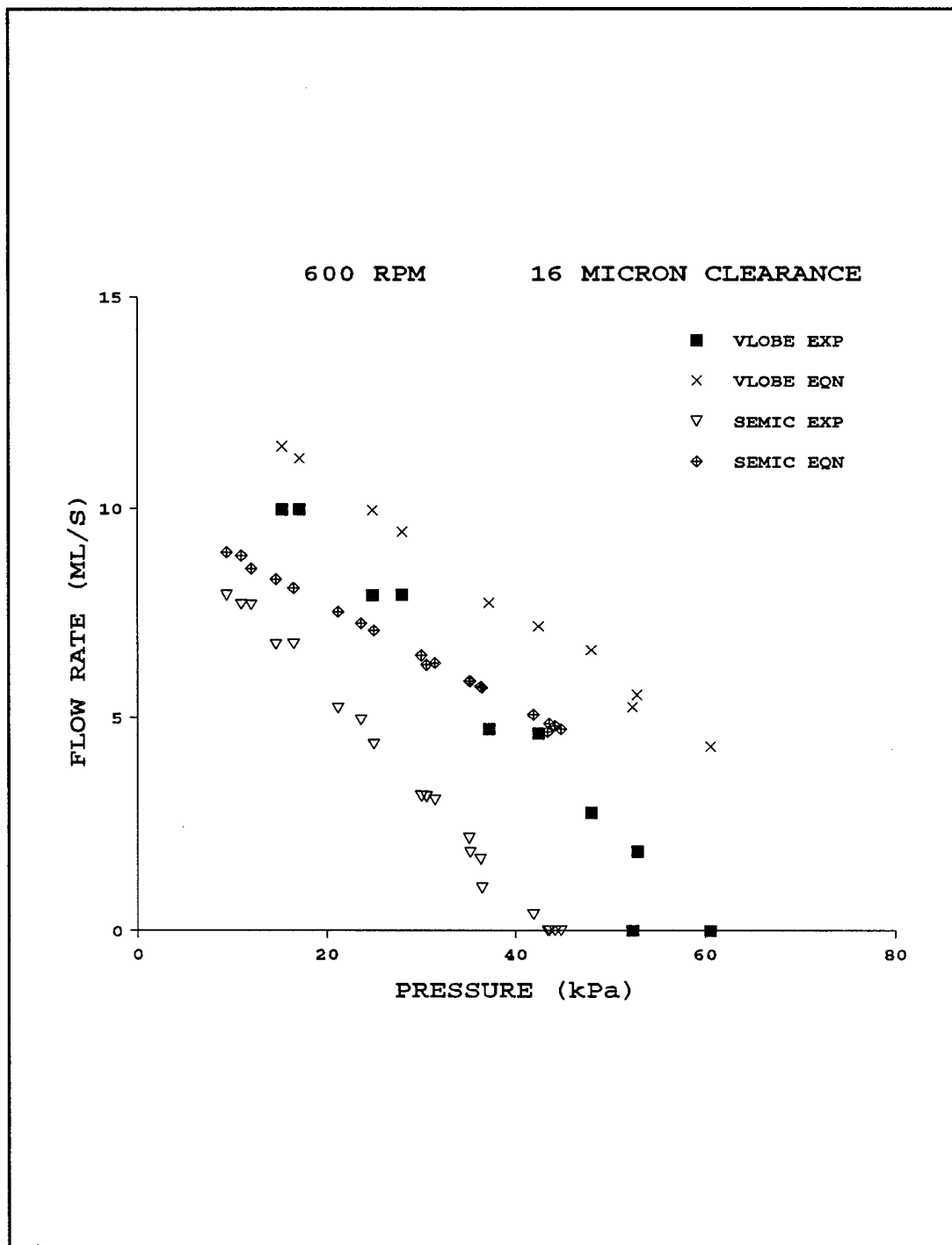


Figure 26 Experimental Results With Comparison to Theory (600 r.p.m., 16 μ m)

an S' other than in the range of $S' = 1 \times 10^{-3}$ then the lobe geometries selected are not optimal values and thus the comparison between the semicircular lobe and V-lobe would not necessarily be appropriate.

The maximum S' values, S'_{\max} , which are based on the maximum pressure developed for each test case, are shown in Table 9. Note that S' varies from approximately zero to S'_{\max} for all cases because the pressure varies from approximately zero to the maximum pressure. The value of $S' = 1 \times 10^{-3}$ was used as a basis for optimal lobe geometry selection. Based on Table 9, this is an excellent selection since $S' = 1 \times 10^{-3}$ falls in the range of the table values. Thus, the comparison between the V-lobe and semicircular lobe experiments is appropriate.

Table 9 Maximum Operating Conditions Parameter (S'_{\max}) Achieved During Experiments

$S'_{\max} \times 10^{-3}$ (Semicircular Lobe)			
$S'_{\max} \times 10^{-3}$ (V-lobe)			
Clearance	600 RPM	1200 RPM	1800 RPM
8 μm	0.469	0.516	0.500
	0.657	0.719	0.708
12 μm	0.985	1.02	1.03
	1.41	1.41	1.41
16 μm	1.50	1.75	1.71
	2.00	2.25	2.25

It is of interest to point out the maximum shear stress to which the fluid is subjected. This value is of great importance when designing a pump to handle sensitive fluids. The maximum shear stress for a given test case is occurs at the outer radius of the pump and when the differential pressure is zero. Using the relationship $\tau = \mu U/c$, the maximum shear stress is 12.6 kPa for the 1800 rpm, 8 μm case and 2.1 kPa for the 600 rpm, 16 μm case for $\mu = 9.75 \text{ mPa}\cdot\text{s}$.

Referring again to the test results in Figures 24, 25 and 26, it is clear that the experimental V-lobe results are consistently better than the semicircular experimental results in these three cases presented as well as the remaining six cases. Note that the flow versus pressure relationship appears to be linear, as suggested by theory.

For both the semicircular lobe pump and the V-lobe pump, the equations predict a larger flow than that realized in practice, particularly at high pressures. The agreement is, however, good at low pressures. Figures 27 and 28 show the test and theoretical results at a given speed (1200 rpm) for varying clearances for the semicircular and the V-lobe, respectively. These graphs show that as the pressure goes to zero, the pumping capabilities become independent of the clearance. Note also that if the data is extrapolated to zero pressure, the theory is an excellent match to the experiments. These trends suggest that the Couette component of flow has been accurately modelled since at zero pressure, the Poiseuille component is zero and it is solely the Couette component that describes the flow. As the pressure increases, the theory deviates from the experimental results. The theoretical model

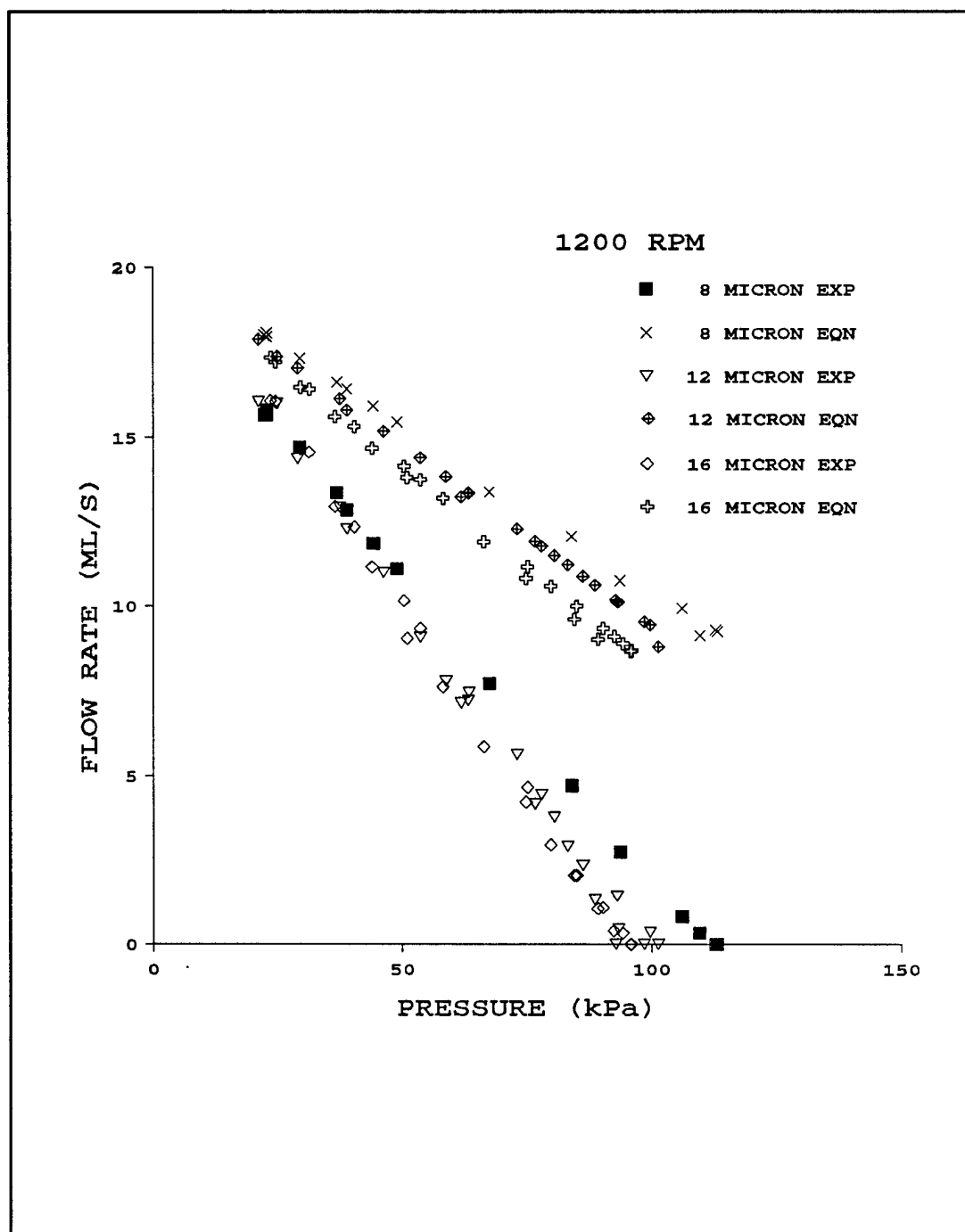


Figure 27 Semicircular Lobe: Experimental and Theoretical Results for Varying Clearance and Constant Speed

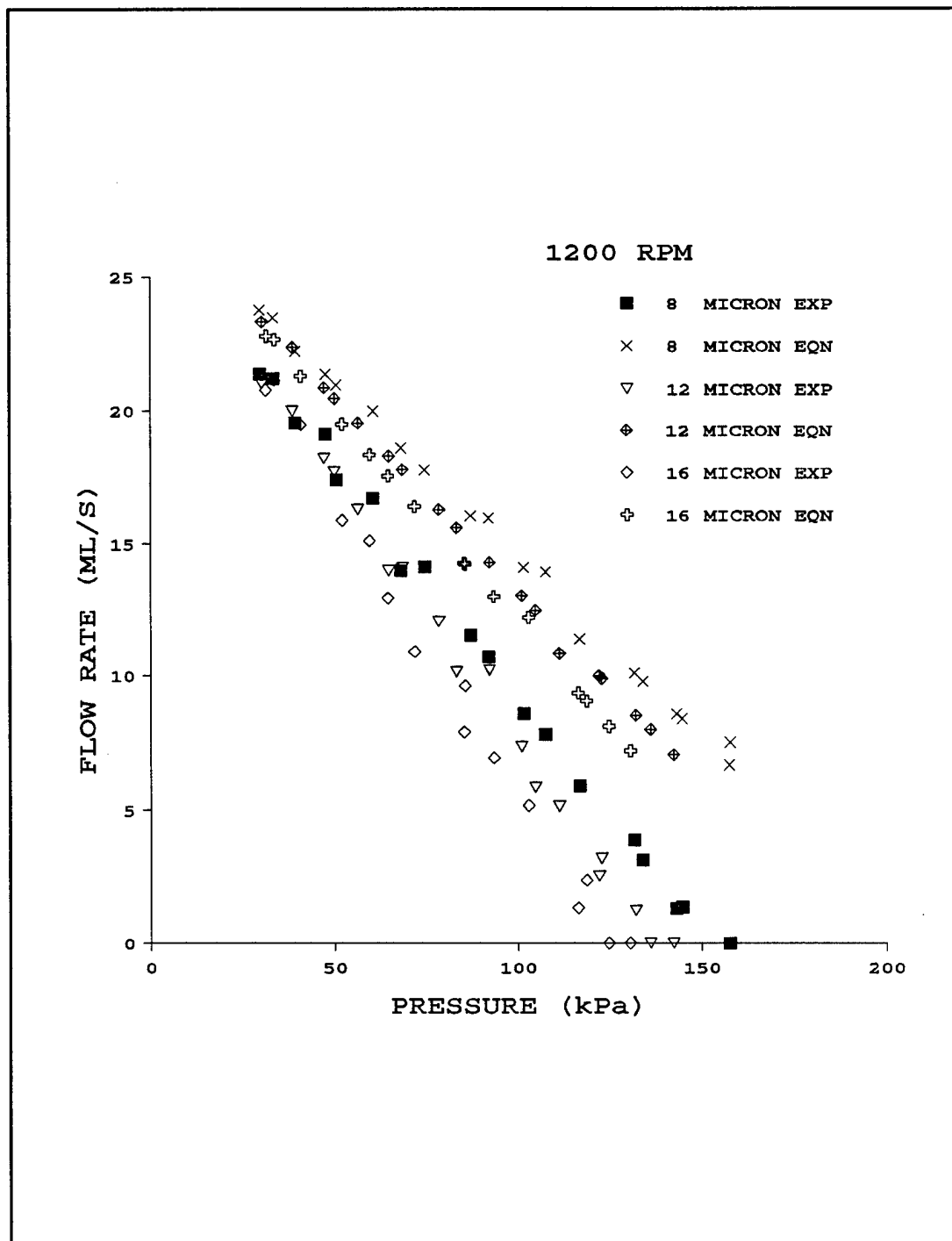


Figure 28 V-lobe: Experimental and Theoretical Results For Varying Clearance and Constant Speed

of the Poiseuille flow is, therefore, not entirely accurate.

Figures 29 and 30 investigate the effect of different viscosities for the semicircular and V-lobe, respectively. To obtain these plots, the experiments were run with the oil at two different temperatures, 31.5°C and 25.0°C. At the lower temperature, the viscosity of the fluid is larger and thus the pumping capabilities of the pump are greater. As the pressure goes to zero, the experimental (and theoretical) results are not dependent on the viscosity. This is expected because the viscosity only appears in the Poiseuille component term. Note again that as the pressure goes to zero, the agreement between experiment and theory is excellent. This trend supports the idea that the Couette flow has been correctly accounted for and it is Poiseuille component of flow that has not been modelled in an entirely accurate manner.

The next step is to have another look at the analysis to determine a possible modification of the theoretical modelling of the Poiseuille flow.

5.1.1 Investigation of Theoretical Models

Because the V-lobe design has been shown to be both theoretically and experimentally superior to the semicircular lobe design, there is no need to further explore the semicircular lobe design. The V-lobe pump will be examined to determine why the theory does not match the experiments at low flow rates and high pressures.

Recall from the development of the V-lobe equations and the discussion in

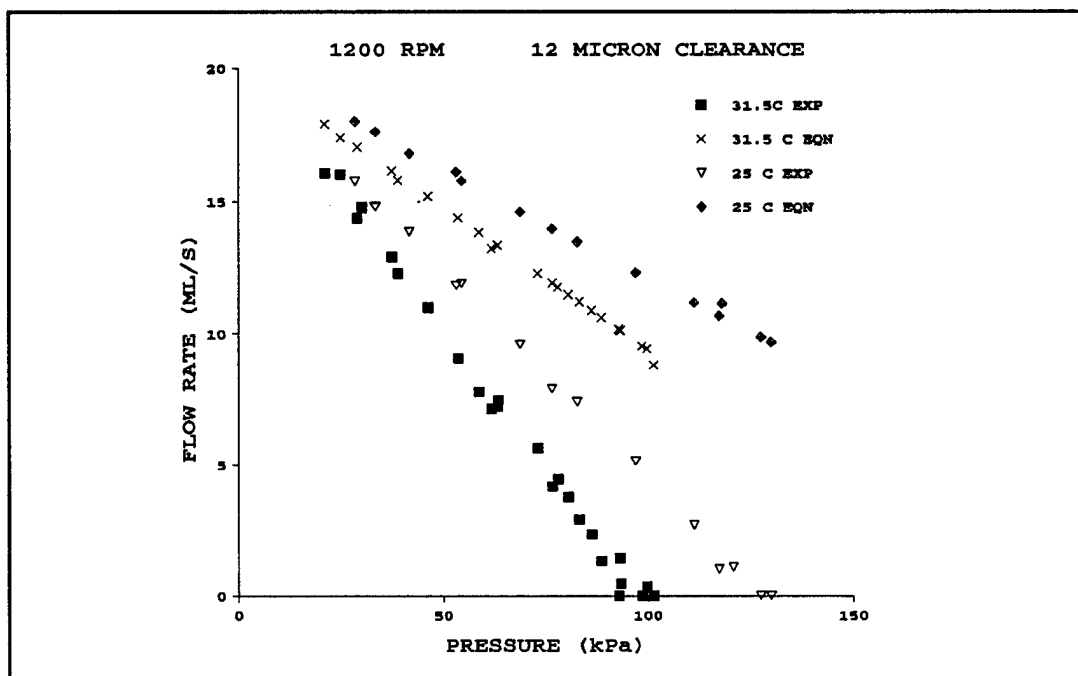


Figure 29 Semicircular Lobe: Experimental and Theoretical Results For Two Temperatures

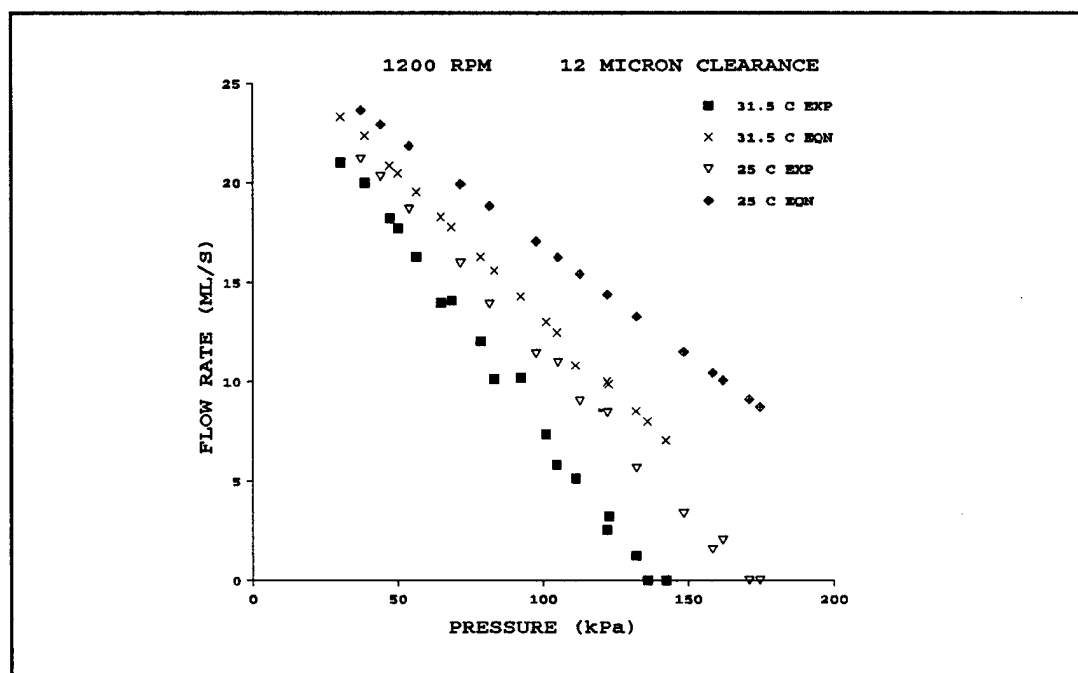


Figure 30 V-lobe: Experimental and Theoretical Results For Two Temperatures

the FEM section (section 3.3.5) that the equations approximate an ideal pump. An ideal pump here is defined to be one for which there is no flow across the leg end boundaries (the lobe edges at the outer radius of the pump). This type of insulated boundary does not actually exist in the tested pump. The stator housing does not provide a physical boundary at the outer edge of the lobes and fluid can, therefore, exit along the lobe leg ends. In the FEM section, a model was investigated which had leg end boundary conditions of $p=0$ as opposed to the insulated boundary conditions. The FEM model with $p=0$ boundary conditions ($FEM_{p=0}$) predicted significantly larger losses than the approximately insulated ($\partial p / \partial s = \text{constant}$) FEM model ($FEM_{\partial p / \partial s = \text{constant}}$).

In the experiments, it is difficult to determine what is actually happening at the leg end boundaries. It is possible that the pressure is zero there (again, recall footnote number 1, page 49). To explore this possibility, the $FEM_{p=0}$ model was solved for the lobes used in the experiment. The FEM model only calculates the Poiseuille component. It has already been shown that the current Couette component model (Equation (36)) is accurate, and therefore it will continue to be used.

Figures 31, 32 and 33 show the comparison between the V-lobe flow equation (Equation (39)), the $FEM_{\partial p / \partial s = \text{constant}}$ model, the $FEM_{p=0}$ model and the experimental results for the 1800 rpm, 8 μm case, the 1200 rpm, 12 μm case, and the 600 rpm, 16 μm case. From these plots, we see that the equations and the

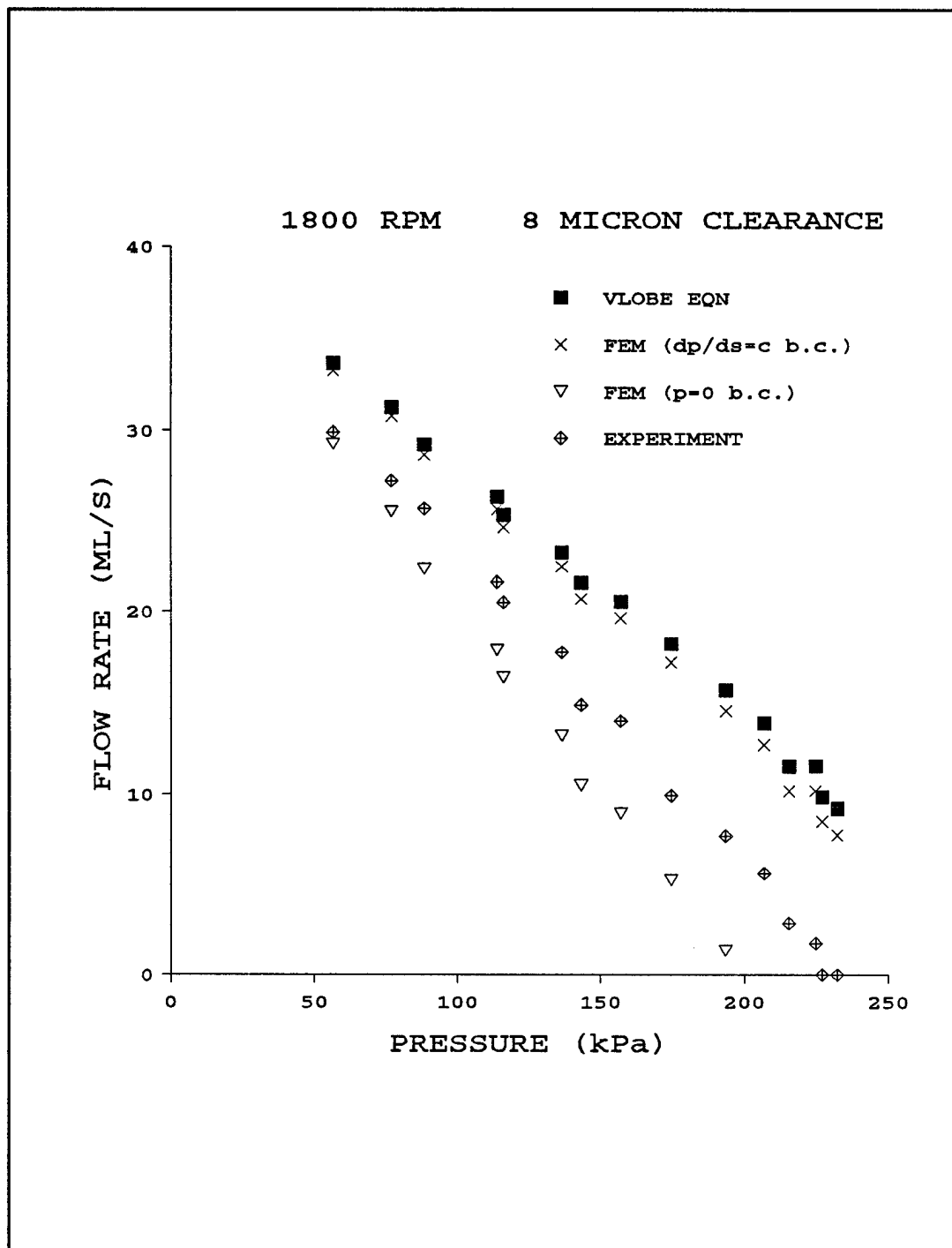


Figure 31 Three Analytical Models Compared to Experimental Results (1800 r.p.m., 8 μ m)

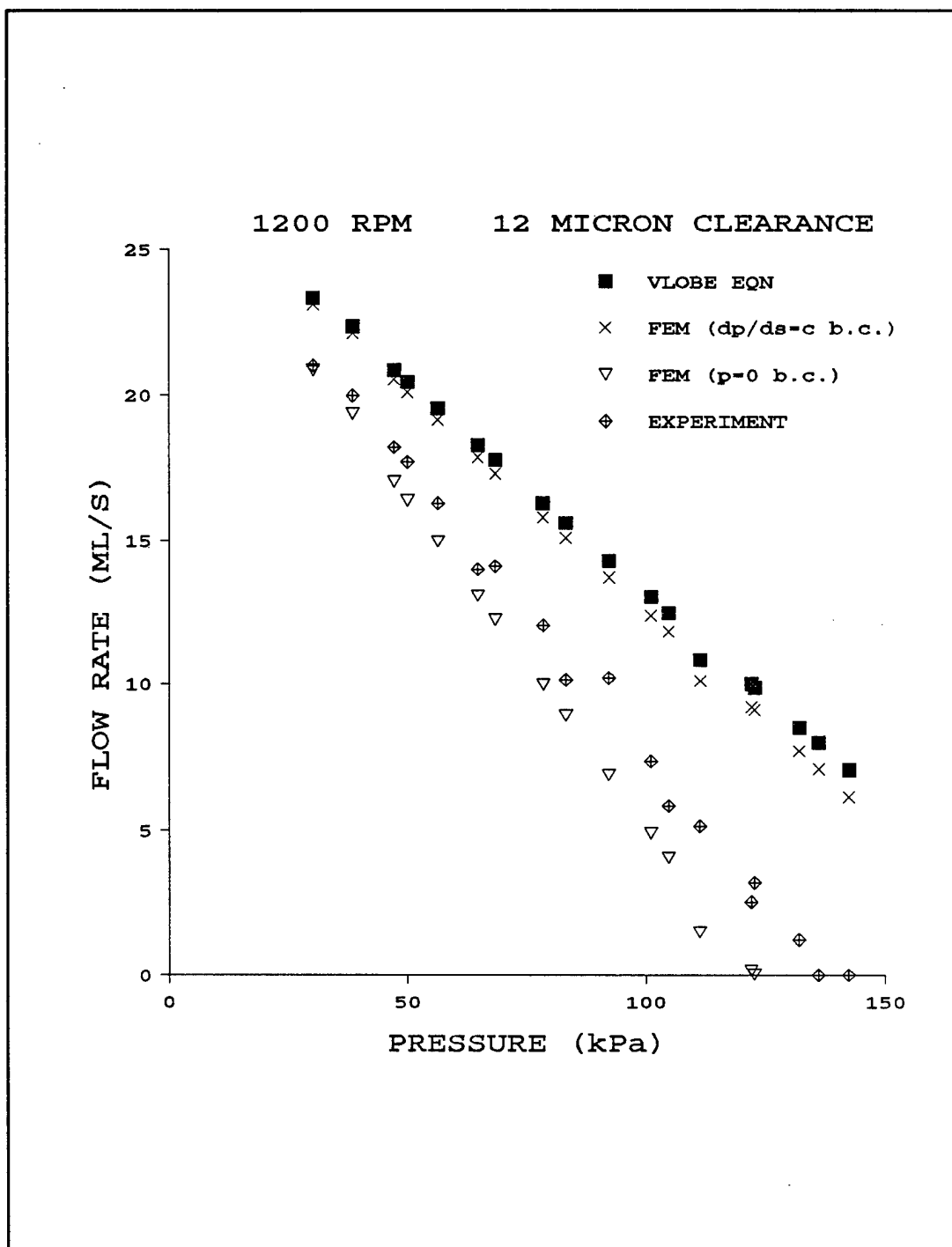


Figure 32 Three Analytical Models Compared to Experimental Results (1200 r.p.m., 12 μ m)

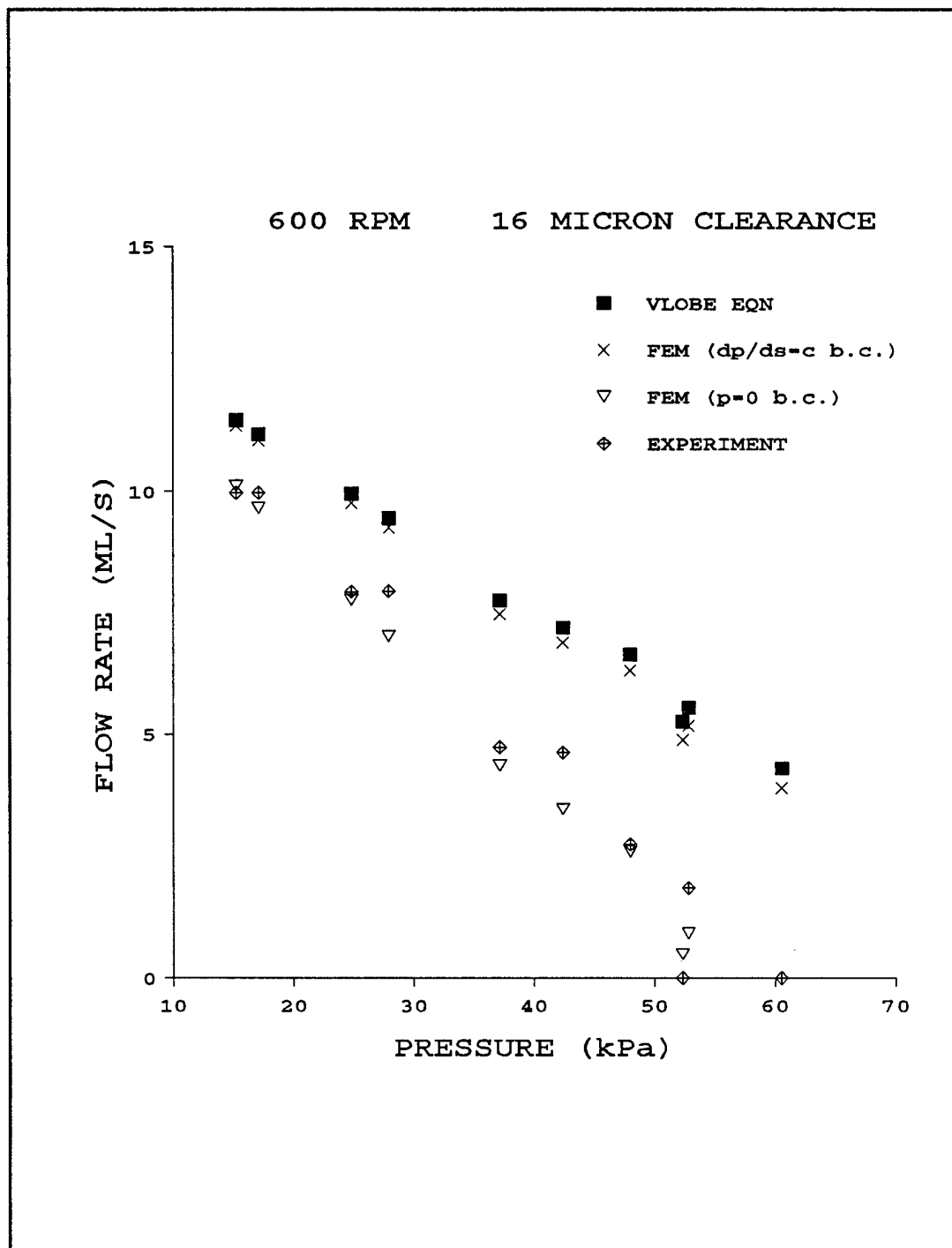


Figure 33 Three Analytical Models compared to Experimental Results (600 r.p.m., 16 μ m)

$FEM_{\partial p/\partial s = \text{constant}}$ model are basically describing the same flow conditions. The experimental results fall somewhere between the $FEM_{\partial p/\partial s = \text{constant}}$ results and the $FEM_{p=0}$ results, but generally the $FEM_{p=0}$ model appears to be more accurate. The complete set of experimental results compared to the $FEM_{p=0}$ model for the V-lobe are shown in Figure 34 ($8 \mu\text{m}$ clearance), Figure 35 ($12 \mu\text{m}$ clearance) and Figure 36 ($16 \mu\text{m}$ clearance). The $FEM_{p=0}$ correlates closely with the experimental results, particularly at low speeds. At higher speeds, the $FEM_{p=0}$ model underestimates the experimental results, though the agreement is still good. Perhaps at the higher speeds, the flow pattern becomes more complicated and the true boundary conditions are somewhere between $p=0$ and $\partial p/\partial s = \text{constant}$.

Overall, there is excellent agreement between the analytical model using the $FEM_{p=0}$ model (with the Couette flow equation (Equation (36))) and the V-lobe experiments, especially at the medium to low speeds. Although the experimental results for flow are slightly larger the analytical results using $FEM_{p=0}$, they still fall within the upper bound created using the $FEM_{\partial p/\partial s = \text{constant}}$ model. Of course, the analysis is not solely to blame for any deviation between experiment and theory. The experiment contains a certain amount of error and approximations. A study of the experimental errors as well as some of the phenomena discovered during the experiment process gives some insight into what is truly happening in the pump.

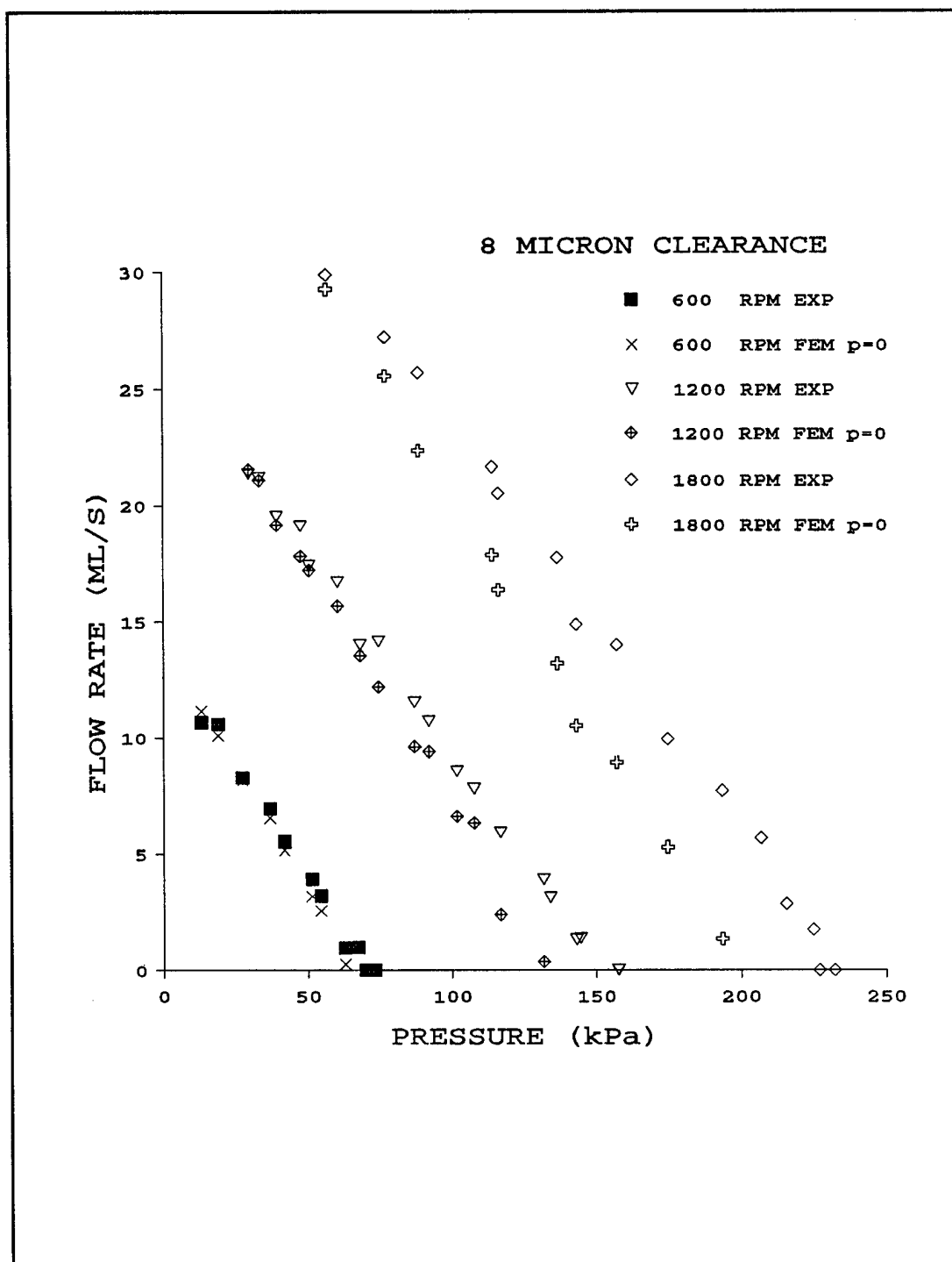


Figure 34 FEM _{$p=0$} Model Compared To V-lobe Experimental Results (8 μm)

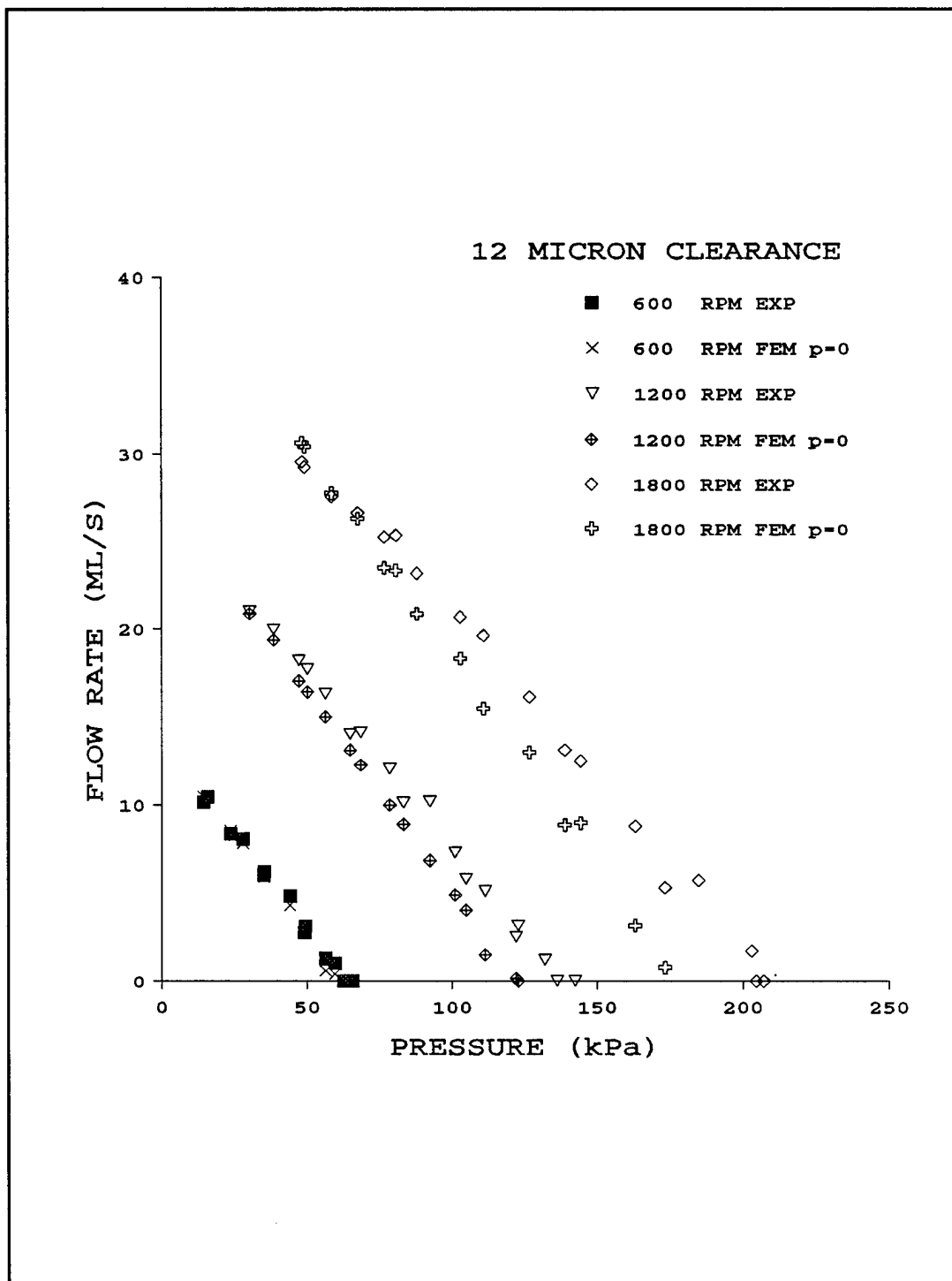


Figure 35 FEM_{p=0} Model Compared to V-lobe Experimental Results (12 μm)

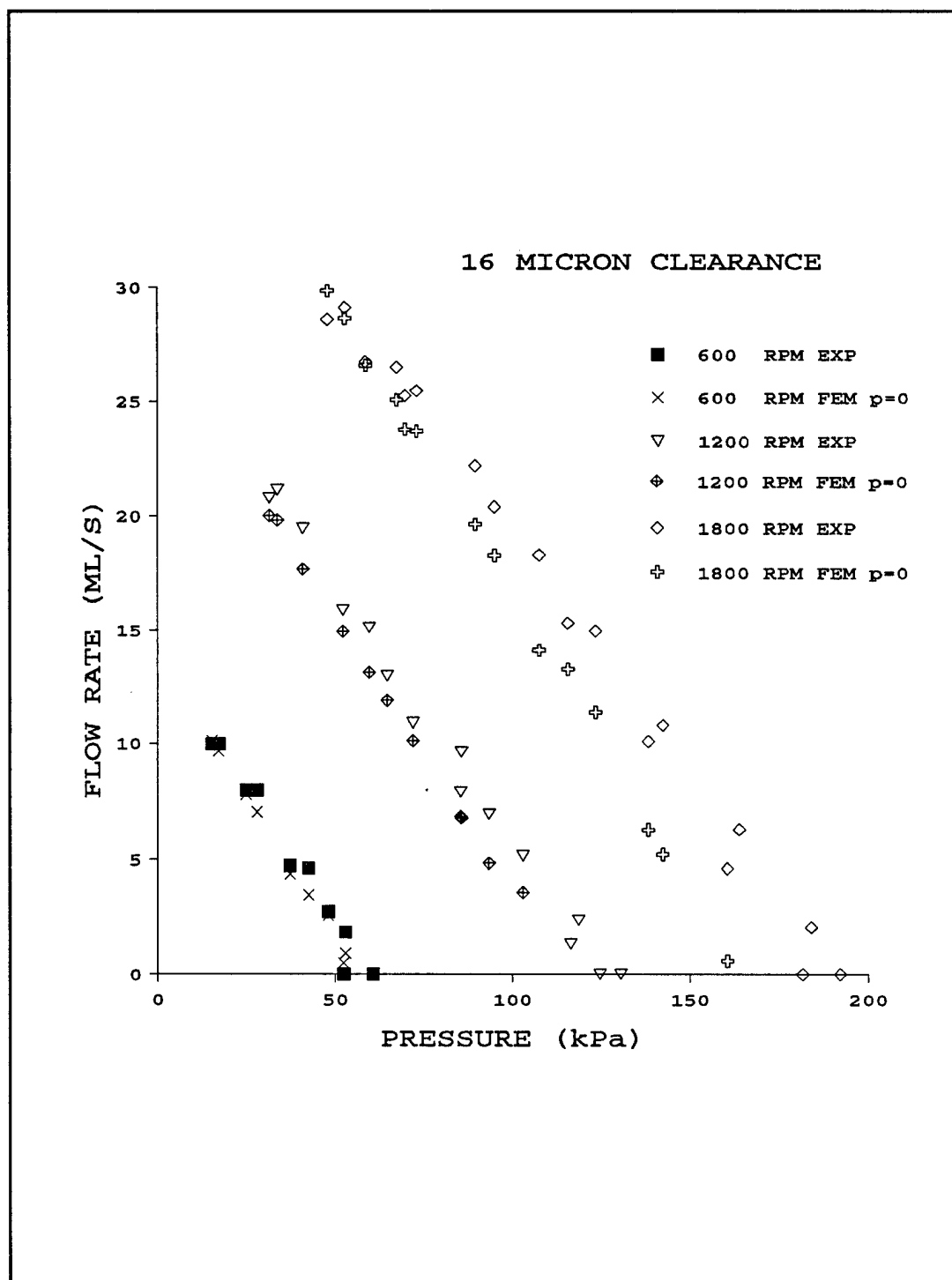


Figure 36 FEM_{p=0} Model Compared to V-lobe Experimental Results (16 μm)

5.1.2 Investigation of Experimental Conditions

To help understand the inaccuracies associated with the experimental results, the inaccuracies of the tests and test equipment will be mentioned here.

Since the pump deals with such small measurements, any machining and pump assembly errors are noticeable. The machined size of the lobes inevitably deviates from the design dimensions. Also, for the assembled pump, when the rotor is rotated without the pump actually running, the runout is as much as three to five microns at the outer edge of the rotor. Although this is significant relative to the clearances at which the pump was operated, the pumping mechanism compensates for some of this runout. When the pump is running, hydrodynamic forces are created which help align the stator with the rotor. This is particularly true at high speeds and small clearances. For the semicircular lobe pump, the lobes are tangent at the outer radius, and are very close to each other at large radii. In this region, a step exists such that the step is formed by C-leg of one lobe and the c-leg of another lobe. Moving in the direction of rotation of the rotor, this is a step up from the C gap to the c gap. This step therefore acts as a Rayleigh step and the hydrodynamic forces generated by it help align the stator and rotor. For the V-lobe pump, the C-legs and the c-legs are not tangent and are spaced far enough apart that a Rayleigh step is not created. Therefore, this design does not benefit from the aligning forces. The effect of the Rayleigh step was detected because more back pressure was needed to maintain a certain clearance at given operating conditions for the semicircular lobes

than for the V-lobes. The effect of the aligning forces is best shown by looking at the rotor from a particular point on the stator (namely, where the proximity probes were located) and seeing how much the time varying clearance differs from the average clearance. These variations are shown in Table 10.

Another problem with the clearance measurement was that the three proximity probes placed axisymmetrically around the pump read slightly different average values when the pump was running. Zero clearance was measured by bringing the rotor and c-legs of the stator into contact and measuring the proximity probe voltages. The operating clearance was then calculated when the pump was running from the measured voltage relative to the contact voltage. If the lobes had slightly different step heights, then the stator c-leg may not be in full contact with the rotor, resulting in error for the contact (zero clearance) voltage measurements. Also, once the pump is operating, these inconsistent step heights would generate slightly

Table 10 Clearance Variations At Specified Test Conditions

RPM, μm	Clearance Variation (μm)	
	Semic-lobe	v-lobe
1800, 8	± 1.0	± 1.5
1200, 12	± 1.1	± 2.5
600, 16	± 1.9	± 5.0

different pressures which would affect the alignment of the rotor and stator. In addition there may be some mechanical interferences which would prevent the stator from being truly flexibly mounted. These effects, together with the effect of gravity pulling the stator back from the rotor at the top of the pump, influenced the existing average clearance at each of the points around the stator. Figure 37 shows the average clearances measured at their respective locations for the semicircular lobe tests and the V-lobe tests for the full range of operating conditions. These varying clearance results are for particular positions on the stator and are not probe dependent. Because the three probes gave slightly different clearance values, an average value was used to describe the clearance. For the tests, a $0.1 \mu\text{m}$ fluctuation about the desired value (8, 12 or $16 \mu\text{m}$) was allowed.

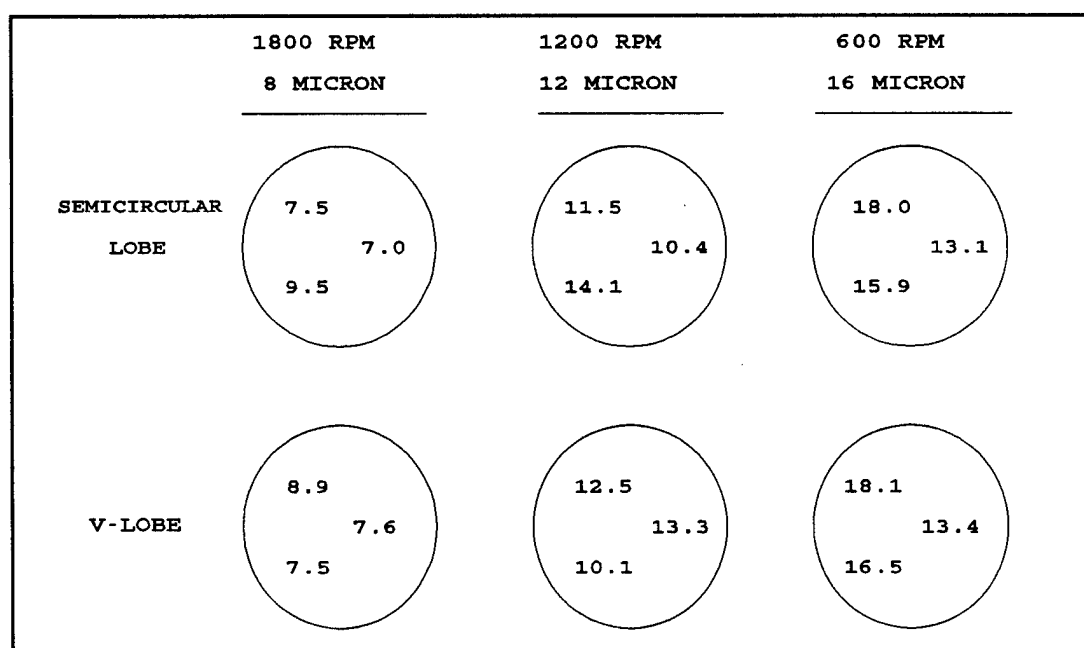


Figure 37 Typical Clearances at Various Stator Locations

The thermocouples also read slightly different values, namely the fluid was warmer in the inside of the pump than on the outside. This is because as the fluid is sheared across the lobe, it is heated. An average of the two temperatures was used to represent the oil temperature. This average value was selected to be 31.5°C and a 0.5°C fluctuation about this value was allowed. For the test cases investigated, the process fluid (mineral oil) would experience a temperature rise ranging from about 1°C for the 600 rpm, $16\text{ }\mu\text{m}$ case to about 3°C for the 1800 rpm, $8\text{ }\mu\text{m}$ case. Concerning the motor, once steady state was reached, the pump reliably supplied a constant speed. The rotameter reading is suspect to error since this measurement was taken with the human eye by reading the location of the top of a ball in the meter relative to scale on the meter. Also, the rotameter may not have been exactly vertical, though this error is small because it is described by only a cosine dependence on the angle of misalignment.

Of course, the accuracy of all calibrations (rotameter, pressure transducer amplifier gain, proximity probe, proximity probe signal amplification) as well as the measured properties of the oil must be recognized as being subject to some error. In spite of these error sources, reliable and repeatable data was taken. For each of the nine test cases run for each lobe design, the experiments were repeated two to three times to ensure that the data taken was repeatable.

5.1.2.1 Occurrences In Experiment Not Accounted For In Theory Effects exist in the experiments that were not accounted for in the analysis and help to

explain differences between the analytical and experimental results.

The Rayleigh step mentioned above generates a localized pressure field at large radii where the lobes are in contact which is not accounted for in the analysis. Another condition which would alter the pressure field but was not accounted for in the analysis is a squeeze film effect. This is created by the rotor and stator moving relative to each other (described above by the time varying clearance) in the experiments. Although the squeeze film term exists in the Reynolds equation, it was not included in the solution to the Reynolds equation. Also, since the Reynolds equation neglects the radial acceleration terms, any centrifugal acceleration effects that exist are not accounted for in the analyses.

Also, the lobes are very close to each other at the outer edges of the stator. There may not be sufficient room for the fluid to enter the center of the pump at radii slightly less than R_o , where the lobes almost touch. Since it is at the large radii that the inward pumping (Couette component) is most effective, the experiments may not be able to produce exactly the results suggested by the Couette component equation. In the experiments run at high speeds, it was noticed that there was some cavitation (most likely air bubbles, but possibly vapor). This problem was augmented by the fact that at these maximum pumping conditions, the pump suction pressure was not great enough to provide an adequate supply of oil to the pump. Pressurizing the oil inlet could help to alleviate this problem. Again, this cavitation was not accounted for in the analysis.

In the analysis, the fluid was assumed to be Newtonian. The fluid used in the experiment was a mineral oil with a very small percentage ($< 1\%$) of polymer additives. Since this is a slightly pseudoplastic fluid, some shear thinning effects are possible, but are probably negligible.

CHAPTER VI

CONCLUSIONS AND RECOMMENDATIONS

Both a semicircular lobe and a new V-lobe viscous pump have been analytically and experimentally investigated. The analysis and the experiments prove that the V-lobe design is superior to the semicircular lobe design.

The analysis was performed using several approaches. The solution for the semicircular lobe is exact (it is based on closed form integration) (Etsion and Yaier, 1988). For the V-lobe, however, a closed form solution does not exist. An analytical model is still provided based on reasonable approximations. The approximations are validated using shape factors and finite element models. For both lobe designs, pump geometry is optimized for maximum pumping capacity. The results of the optimization show that the V-lobes produces a superior pumping mechanism to the semicircular lobe. The optimization is based on a pump having ideal (insulated) boundary conditions.

The V-lobes have two major advantages over the semicircular lobe. This first is that simply making the lobes straight, as opposed to being curved, reduces the pumping losses. The second and most important advantage is that the radial extent of the lobes and the number of lobes is not limited by geometry constraints such as the tangency requirement of the semicircular lobes. For the semicircular lobe design,

once the number of lobes have been determined for a particular R_o , R_i is a derived (dependent) value. This constraint does not exist for the V-lobes. The V-lobes can go as deep, theoretically, as the radius of the pump (from the center to the outer radius of the pump) such that R_i (which is determined by the angle α) is zero. The angle α (and, therefore, R_i) must be greater than zero in practice to allow room for the fluid to exit the pump. As α increases, however, the maximum flow capacity of the V-lobe pump decreases. If α increases to a value such that the corresponding R_i is equivalent to the R_i in the semicircular lobe, the pumping capacity of the two lobe designs is about the same for the same number of lobes. Still, the V-lobe is slightly better than the semicircular lobe because of the reduced pumping losses. For a given R_o , however, the V-lobe design is not restricted to any particular number of lobes as is the case with the semicircular lobe design. The V-lobe pump can have any number of lobes, and we have seen that pumping capacity increases as the number of lobes increases. The only reason that R_i would need to be prescribed would be if this were the radius of the fluid exit hole. For given R_i and R_o , the V-lobe is only slightly superior to the semicircular lobe for the same number of lobes. For the V-lobe design, however, the number of lobes can be increased to further improve pumping capacity relative to the semicircular lobe.

It is important to emphasize that the optimization was performed on the basis of maximizing the flow rate, Q . Once $Q=0$, the optimization is moot, and the V-lobe design does not necessarily have a higher pressure than the semicircular lobe design.

An alternate optimization could have been performed to maximize the pressure. In such case, the optimization would be moot when $p=0$. The optimization was done with S' as a given parameter and the optimized lobe designs were compared to each other for a given value of S' . For $Q=0$, all optimized designs will yield the same pressure if S' is the same and all other parameters defining S' are the same. The optimization based on maximizing Q for a given S' maximizes the flow at zero pressure while the pressure at zero flow is defined by S' . The pump performance curve is linear and includes these two points.

A test rig was devised and the two lobe designs were tested using a real time data acquisition system. Based on the experimental results, it was confirmed that the V-lobe pump was more efficient than the semicircular lobe pump. The analysis showed good agreement with experimental results, though some deviation was found at relatively low flow rates and high pressures. This deviation was explained by considering alternate boundary conditions in the analysis.

The analysis on which the optimization was based was for a pump with ideal boundary conditions (insulated lobe leg ends). These insulated boundary conditions, however, do not exist in the pump used in the experiments. The actual test pump has physical boundary conditions which are less than ideal (fluid can flow across the lobe leg ends). The analysis using boundary conditions more appropriate to the test pump, namely $p=0$ along the lobe leg ends ($FEM_{p=0}$), shows excellent agreement with the experimental results.

A more efficient pump could be built by incorporating insulated lobe leg ends, as demonstrated by the analysis. This could be accomplished by providing a physical barrier to the flow at the end of the lobe legs. This option realizes a better pump than the current pump since the losses are reduced. An alternative to altering the physical pump would be to optimize equations which use the boundary conditions in existence in the test pump. The equations used to optimize lobe geometry for the test pump were based on ideal boundary conditions. An improved pump could be designed if more appropriate equations were used in the optimization process. The analysis using the $FEM_{p=0}$ model (which used $p=0$ for the boundary condition at the lobe leg ends) showed excellent agreement with the experimental results. Since the FEM models can only be solved on a case by case basis, it would not be practical to use them to find optimal geometry. Equations could be developed which take into account the boundary conditions that the $FEM_{p=0}$ model uses. This could be done by assuming that the fluid leaves the center of the pump (from the $p=P$ region to the $p=0$ region) across the portion of the lobe that had the shortest distance. This means that the fluid flows in a direction where there is the largest pressure gradient. These equations, which better take into account what is actually going on in the pump, could be optimized to solve for the geometry which would provide the largest pumping capacity.

Additional design modifications can be made to the existing design to improve the accuracy of the pump. Currently, the rotor is rigidly mounted. Because of this,

the stator has difficulty tracking the rotor when hydrodynamic balancing forces are small (at low speeds and large clearances). If the rotor were flexibly mounted, the stator and rotor would do a better job of tracking each other and a more consistent clearance between the rotor and stator could be maintained.

Increased pumping capacity could be realized by locating the rotor between two stators. This is equivalent to operating two pumps in parallel. The rotor could contain a magnet and be externally driven by a magnetic field.

Further improvements could probably be made on the lobe leg configuration. These improvements would be based on modifications of the V-lobe design and include options such as variable lobe width and step height along the length of the lobe legs. Modifications of this nature, however, would be made at the cost of increased machining complexity for the lobes.

APPENDIX A

Derivation of Straight Lobe Equations

A.1 Symmetric V-lobe

The derivation of the equations for the symmetric V-lobe is based on the geometric variable definitions in Figure 36. First, the relevant geometric relations will be shown and then these relations will be incorporated in the equations for Couette and Poiseuille flow. The total flow is assumed to be a superposition of these two components.

The variables in the geometry are α , β , δ , and $s=C-c$; R_o is a given operating conditions parameter. All other labels will be defined in terms of these fundamental

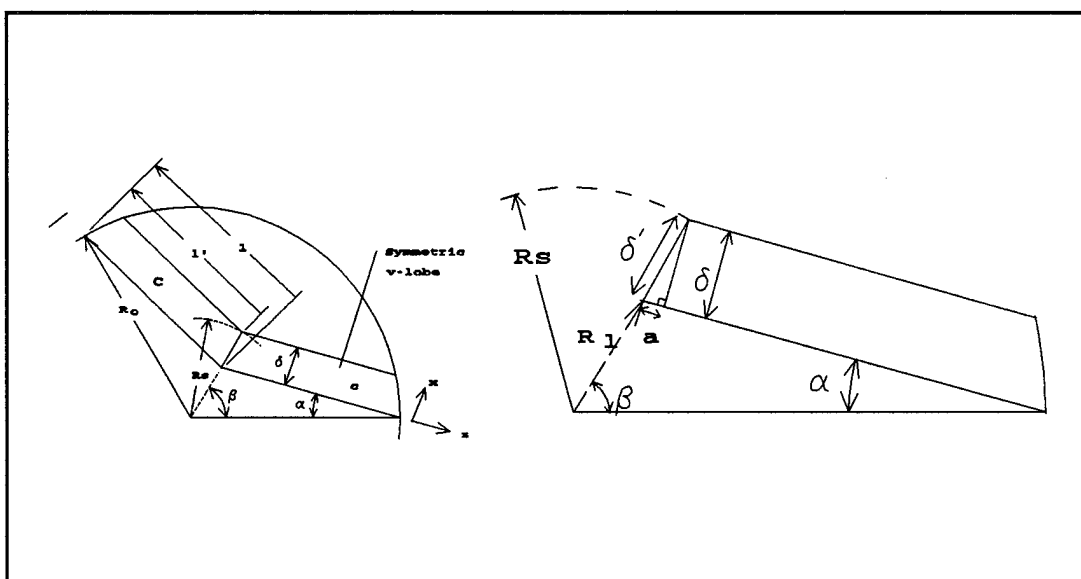


Figure 38 Symmetric V-lobe Geometry

variables. The important relations are as follows:

$$\frac{R_l}{\sin \alpha} = \frac{R_o}{\sin[\pi - (\alpha + \beta)]} = \frac{R_o}{\sin(\alpha + \beta)} \quad (65)$$

$$\frac{\delta}{\delta'} = \sin(\alpha + \beta) \quad (66)$$

Using Equations (65) and (66), R_s is expressed as

$$R_s = R_l + \delta' = \frac{R_o \sin \alpha}{\sin(\alpha + \beta)} + \frac{\delta}{\sin(\alpha + \beta)} = \frac{R_o \sin \alpha + \delta}{\sin(\alpha + \beta)} \quad (67)$$

The length l is found using the following relations:

$$\frac{l}{\sin \beta} = \frac{R_o}{\sin(\alpha + \beta)} \quad (68)$$

Hence,

$$l = \frac{R_o \sin \beta}{\sin(\alpha + \beta)} \quad (69)$$

The distance a is

$$a = \delta \tan(\alpha + \beta) \quad (70)$$

Using Equations (69) and (70), the length $l' = l - a$ is

$$l' = \frac{R_o \sin \beta - \delta \cos(\alpha + \beta)}{\sin(\alpha + \beta)} \quad (71)$$

The shear induced flow is found using the equation for Couette flow per unit length:

$$q_s = \frac{\omega r h}{2} \quad (72)$$

This equation is applied to the c-leg ($h=c$) and the C-leg ($h=C$) of Figure 36. The net Couette flow (net inward flow) occurs from R_s to R_o through the gap, $s=C-c$.

This is expressed as

$$Q_s = \int_{R_s}^{R_o} \frac{\omega s r}{2} dr = \frac{\omega s r^2}{4} \Big|_{R_s}^{R_o} \quad (73)$$

Using the equation for R_s (Equation (67)), this is rewritten as

$$Q_s = \frac{\omega s}{4} \left\{ R_o^2 - \left[\frac{R_o \sin \alpha + \delta}{\sin(\alpha + \beta)} \right]^2 \right\} \quad (74)$$

The pressure-gradient induced flow is found using the equation for Poiseuille flow per unit length:

$$q_p = -\frac{h^3}{12\mu} \frac{\partial p}{\partial x} \quad (75)$$

A conservative estimate for the pump losses (i.e., large Poiseuille flow) is to assume that $\partial p / \partial x$ is a constant value equal to P / δ over the length, l . The Poiseuille flow is then

$$Q_p = \int_0^l \frac{C^3}{12\mu} \frac{\partial p}{\partial x} dz + \int_0^l \frac{c^3}{12\mu} \frac{\partial p}{\partial x} dz \quad (76)$$

A less conservative, though probably more accurate, length to use is the length l' (instead of l) of Equation (71) in Equation (76). The result of the integration of Equation (76) is

$$Q_p = -\frac{P(C^3+c^3)}{12\mu\delta} \frac{R_o \sin\beta}{\sin(\alpha+\beta)} \quad (77)$$

when using the length l , and

$$Q_p = -\frac{P(C^3+c^3)}{12\mu\delta} \frac{R_o \sin\beta - \delta \cos(\alpha+\beta)}{\sin(\alpha+\beta)} \quad (78)$$

when using the length l' .

As mentioned earlier, the total flow is a linear superposition of the Couette and Poiseuille flow ($Q_s + Q_p$) and is written for n lobes as

$$Q = n \left\{ \frac{\omega s}{4} \left[R_o^2 - \left(\frac{R_o \sin\alpha + \delta}{\sin(\alpha+\beta)} \right)^2 \right] - \frac{P(C^3+c^3)R_o \sin\beta}{12\mu\delta \sin(\alpha+\beta)} \right\} \quad (79)$$

when using the length l , and

$$Q = n \left\{ \frac{\omega s}{4} \left[R_o^2 - \left(\frac{R_o \sin \alpha + \delta}{\sin(\alpha + \beta)} \right)^2 \right] - \frac{P(C^3 + c^3)(R_o \sin \beta - \delta \cos(\alpha + \beta))}{12 \mu \delta \sin(\alpha + \beta)} \right\} \quad (80)$$

when using the length l' .

A dimensionless equation for flow, Q' , is obtained using

$$Q = \frac{1}{2} \omega c R_o^2 Q' \quad (81)$$

and

$$\xi = \frac{\delta}{R_o} ; \quad \sigma = \frac{s}{c} ; \quad S' = \frac{\pi}{12} \frac{P}{\mu \omega} \left(\frac{c}{R_o} \right)^2 \quad (82)$$

where S' is an operating conditions parameter. Substituting these relations (Equations (81) and (82)) into Equations (79) and (80) yields

$$Q' = n \left\{ \frac{\sigma}{2} \left[1 - \left(\frac{\sin \alpha + \xi}{\sin(\alpha + \beta)} \right)^2 \right] - 2S' \frac{[(1 + \sigma)^3 + 1] \sin \beta}{\pi \xi \sin(\alpha + \beta)} \right\} \quad (83)$$

when using the length l , and

$$Q' = n \left[\frac{\sigma}{2} \left(1 - \left(\frac{\sin \alpha + \xi}{\sin(\alpha + \beta)} \right)^2 \right) - 2S' \frac{[(1 + \sigma)^3 + 1] (\sin \beta - \delta \cos(\alpha + \beta))}{\pi \xi \sin(\alpha + \beta)} \right] \quad (84)$$

when using the length l' .

A.2 Nonsymmetric V-lobe

The geometry for the nonsymmetric V-lobe is shown in Figure 37. The development of the nonsymmetric V-lobe equations follows the same format as that outlined above for the symmetric V-lobe equations. The variables in the geometry are α , β , δ and $s=C-c$; R_o is a given operating conditions parameter. All other labels will be defined in terms of these fundamental variables. First, the angle ψ is found as follows:

$$\frac{\delta}{\delta'} = \tan \psi_1 = \tan \psi_2 \quad (85)$$

OR

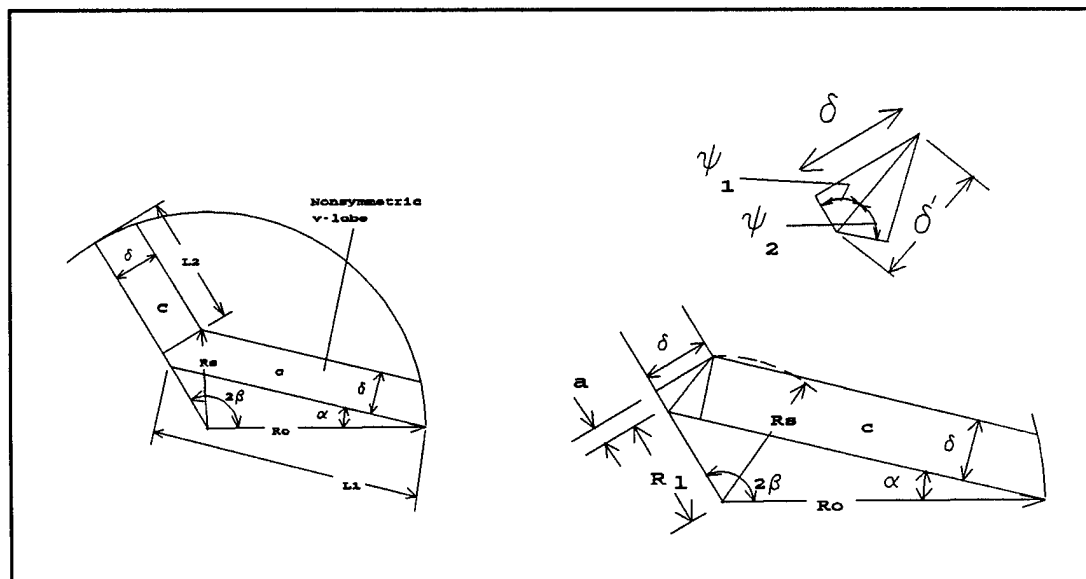


Figure 39 Nonsymmetric V-lobe Geometry

$$\psi_1 = \psi_2 = \psi = \frac{\alpha + 2\beta}{2} \quad (86)$$

Using this relation, it is seen that the distance a is

$$a = \frac{\delta}{\tan \psi} = \frac{\delta}{\tan\left(\frac{\alpha + 2\beta}{2}\right)} \quad (87)$$

R_l is related to the geometry as follows:

$$\frac{R_l}{\sin \alpha} = \frac{R_o}{\sin[\pi - (\alpha + 2\beta)]} = \frac{R_o}{\sin(\alpha + 2\beta)} \quad (88)$$

The radius R_s is found from

$$R_s^2 = \delta^2 + (R_l + a)^2 = \delta^2 + \left[\frac{R_o \sin \alpha}{\sin(\alpha + 2\beta)} + \frac{\delta}{\tan\left(\frac{\alpha + 2\beta}{2}\right)} \right]^2 \quad (89)$$

Another important length is $L1$ and is found as follows:

$$\frac{L1}{\sin 2\beta} = \frac{R_o}{\sin[\pi - (\alpha + 2\beta)]} = \frac{R_o}{\sin(\alpha + 2\beta)} \quad (90)$$

Hence,

$$L1 = \frac{R_o \sin 2\beta}{\sin(\alpha + 2\beta)} \quad (91)$$

The length L_2 is

$$L_2 = R_o - a - R_i = R_o - \frac{\delta}{\tan\left(\frac{\alpha+2\beta}{2}\right)} - \frac{R_o \sin \alpha}{\sin(\alpha+2\beta)} \quad (92)$$

The Couette component of flow is found by applying Equation (72) and (73) to this geometry. The result is

$$Q_s = \frac{\omega s}{4} \left\{ R_o^2 - \delta^2 - \left[\frac{R_o \sin \alpha}{\sin(\alpha+\beta)} + \frac{\delta}{\tan\left(\frac{\alpha+2\beta}{2}\right)} \right]^2 \right\} \quad (93)$$

The Poiseuille flow is found using Equation (75) and performing the following integration:

$$Q_p = \int_0^{L_2} \frac{C^3}{12\mu} \frac{\partial p}{\partial x} dz + \int_0^{L_1} \frac{c^3}{12\mu} \frac{\partial p}{\partial x} dz \quad (94)$$

By approximating $\partial p / \partial x$ as P / δ over the lengths L_1 and L_2 , the result of the integration is

$$Q_p = -\frac{C^3 P}{12\mu \delta} \left(R_o - \frac{\delta}{\tan \psi} - \frac{R_o \sin \alpha}{\sin(\alpha+2\beta)} \right) - \frac{c^3 P}{12\mu \delta} \left(\frac{R_o \sin 2\beta}{\sin(\alpha+2\beta)} \right) \quad (95)$$

The superposition of the Couette and Poiseuille (Equations (93) and (95)) yields the

total flow for n lobes:

$$Q = \frac{n\omega s}{4} \left(R_o^2 - \left\{ \delta^2 + \left[\frac{R_o \sin \alpha}{\sin(\alpha + \beta)} + \frac{\delta}{\tan\left(\frac{\alpha + 2\beta}{2}\right)} \right]^2 \right\} \right) - \frac{nP}{12\mu\delta} \left\{ C^3 \left[R_o - \frac{\delta}{\tan \psi} - \frac{\sin \alpha}{\sin(\alpha + 2\beta)} \right] + c^3 \left[\frac{R_o \sin 2\beta}{\sin(\alpha + 2\beta)} \right] \right\} \quad (99)$$

Using the relations in Equations (81) and (82), the dimensionless flow, Q' , is found to be

$$Q' = n \left\{ \frac{\sigma}{2} \left[1 - \xi^2 - \left(\frac{\sin \alpha}{\sin(\alpha + 2\beta)} + \frac{\xi}{\tan \psi} \right)^2 \right] - \frac{2S'}{\xi \pi} \left[(1 + \sigma^3) \left(1 - \frac{\xi}{\tan \psi} - \frac{\sin \alpha}{\sin(\alpha + 2\beta)} \right) + \frac{\sin(2\beta)}{\sin(\alpha + 2\beta)} \right] \right\} \quad (100)$$

APPENDIX B

SHAPE FACTORS

The solution to the Laplace equation ($\nabla^2 \phi = 0$) takes on the form $\Delta\phi = QR'$ where ϕ is the potential, Q represents a flow and R' is the resistance. For example, when a portion of the boundaries are insulated (no flow) and the remaining boundaries have Dirichlet boundary condition, the flow can be rewritten as

$$Q = K S \Delta\phi \quad (101)$$

where K is the conductivity and S is a shape factor. Although a closed form solution to the Laplace equation is possible for simple geometries, an exact solution is not always possible for more complex geometries. For the more complex geometries, expressions for the upper and lower bounds for the flow over the geometry being considered may be helpful. Although the Laplace equation could be solved using finite difference or finite elements on a case by case basis, equations more useful to use when optimizing geometry or making initial design calculations.

Equations will be developed here which will provide upper and lower bounds to the flow across the V-lobes used for the pump. The generalized results will provide a methodology for calculating bounds for flow across any type of geometry. Electrical and heat transfer analogies will be made to gain a mental grasp of how the bounds work.

Consider the circuit in Figure 38(a). The potential equals the flow (current) multiplied by the resistance as follows:

$$V = I(a+b) \quad ; \quad V = J(c+d) \quad (102)$$

The total flow is $Q=I+J$. A theorem is now proposed that if a

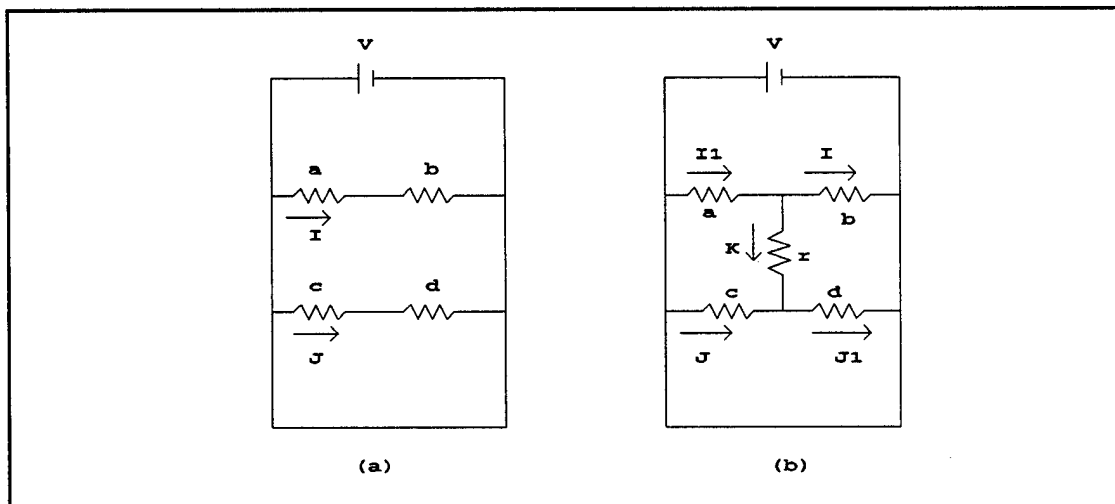


Figure 40 Electrical Circuits For Determining Current Bounds

resistance, r , is added to the circuit as in Figure 38(b), the total current, Q , can only increase. For this circuit, the total current is $Q=I+J+K$. The solution of this circuit yields the following:

$$Q = I+J+K = V \left[\frac{1}{a+b} + \frac{1}{c+d} + \frac{\left(\frac{c}{c+d} - \frac{a}{a+b}\right)^2}{a - \frac{a^2}{a+b} + \frac{cd}{c+d} + r} \right] \quad (103)$$

If r is infinite, the circuit in Figure 38 (b) reduces to the circuit in Figure 38(a) and the total flow, Q , is a minimum. If r takes on a finite value, the flow increases, and when $r=0$, the flow is a maximum.

A heat transfer analogy can be made here by considering Figure 39. In this figure, the outer walls are insulated and the materials are designated as types A, B

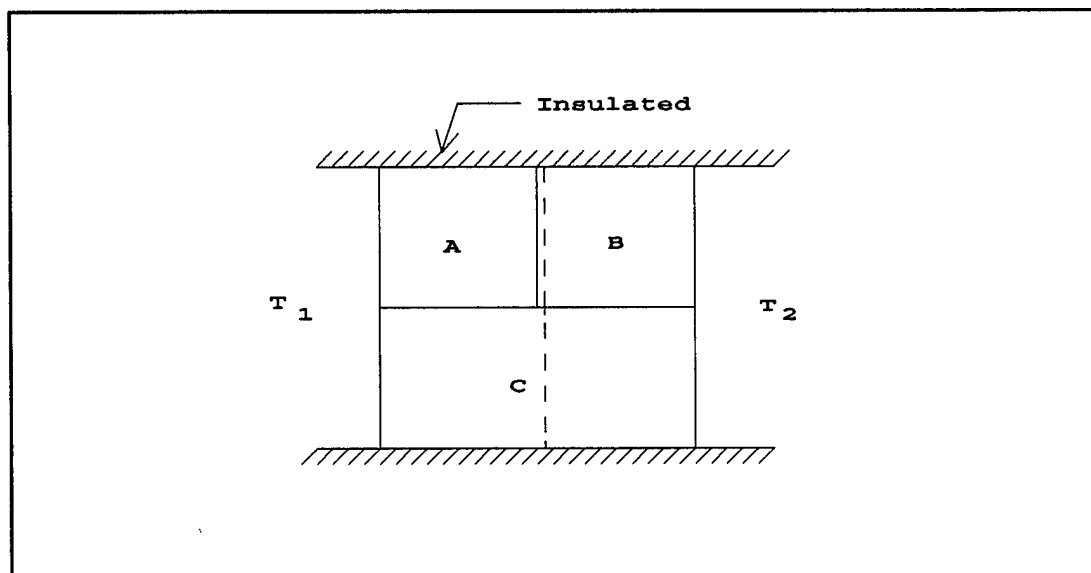


Figure 41 Heat Transfer Analogy of Electric Circuits

and C. If the assumption is made that the wall separating material C from materials A and B is insulated (adiabatic), then the problem reduces to the circuit in Figure 38(a) (or, equivalently, the circuit of Figure 38(b) for $r \rightarrow \infty$). For this case, the heat flow is a minimum, corresponding to a lower bound. The heat flow travels along insulated lines parallel to the insulated walls. Conversely, if it is assumed that the dashed line is an isotherm (as if a plane of infinite conductivity is inserted between

materials A and B and cuts through C), then the problem reduces to the electrical circuit problem in Figure 38 (b) where $r=0$. This means that the flow is a maximum and represents an upper bound.

Consider the problem in Figure 40. Although this is a simple geometry, it will

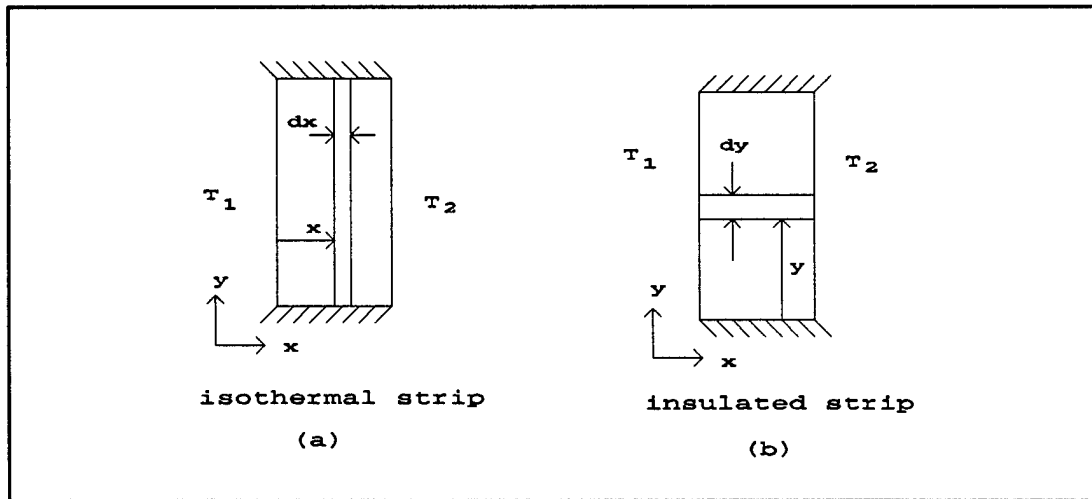


Figure 42 Simple Geometry For Calculating Shape Factors (a) Isotherms - Upper Bound (b) Insulated Strips - Lower Bound

be used to illustrate the concept of lower and upper bounds for shape factors. The equation for flow is:

$$Q = \int_0^L -K \frac{\partial T}{\partial x} dy = K \frac{L}{D} (T_2 - T_1) \quad (104)$$

since K and $\partial T / \partial x$ are independent of z . Comparing this equation to Equation (101), we see that the shape factor is $S = L/D$ and the flow is $Q = KS(T_2 - T_1)$. S represents an integrated average of the length to width ratio.

This shape factor can be calculated by assuming the horizontal lines are isotherms (this will provide an upper bound for the flow) as in Figure 40(a). The resistance, R , is defined to be $1/S$. R is found by integrating the ratio of the differential width to the length of the isothermal strip over the width, D , as follows:

$$dR = \frac{dx}{L} \quad ; \quad R = \int_0^D \frac{dx}{L} = \frac{D}{L} \quad (105)$$

Since $S=1/R$, the upper bound shape factor (which is used to calculate the upper bound for the flow) is $S_u=L/D$.

The shape factor can also be calculated by assuming that vertical lines are insulated as in Figure 40(b). The shape factor is found by integrating the ratio of the differential length to the width over the length of the insulated strip as follows:

$$dS = \frac{dy}{D} \quad ; \quad S = \int_0^L \frac{dy}{D} = \frac{L}{D} \quad (106)$$

The lower bound shape factor is then $S_l=L/D$. Note that the shape factor in the exact solution equals the shape factors which provide the lower and upper bounds. This result is expected because the assumptions made for the two bounds are exact.

The next step is to consider more complex geometries where a closed form solution does not exist. The geometry in Figure 41 is one which has been solved in the literature with shape factors (Kreith and Bohn, 1986). This case will be explored to make an easy transition from showing how the shape factors are used in heat

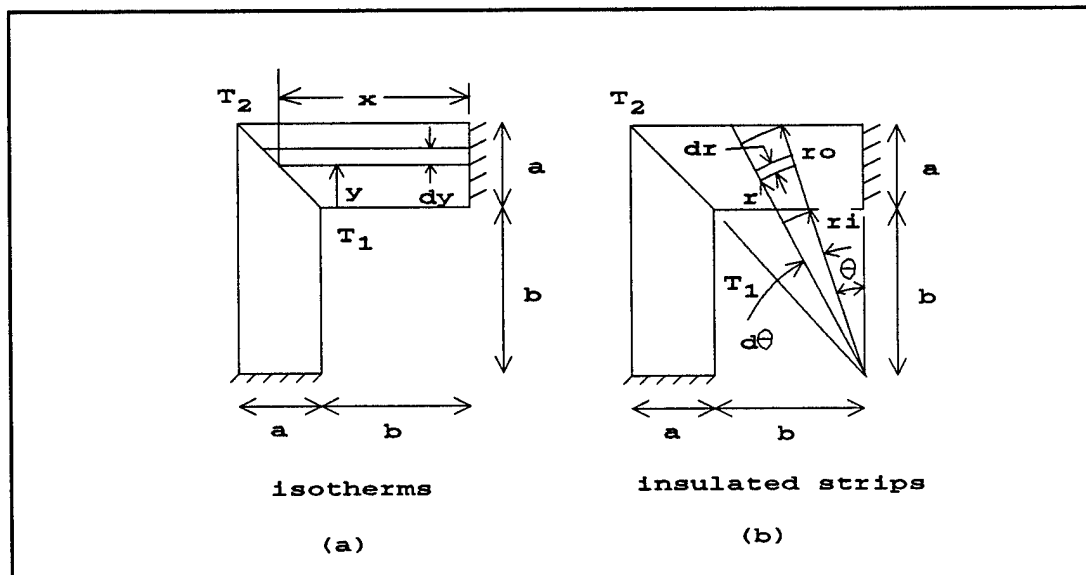


Figure 43 Corner Geometry For Calculating Shape Factors (a) Isotherms - Upper Bound (b) Insulated Strips - Lower Bound

transfer to how they can be used in lubrication problems. The general equation for heat flow is written as $Q=2SK(T_2-T_1)$. The factor of 2 is used since the problem is symmetric and S will only be calculated for half the geometry. The upper bound shape factor, S_u , is found by integrating the ratio of the differential width to the length of the isothermal strip shown in Figure 41(a) over the length as follows:

$$dR = \frac{dy}{b+y} \quad ; \quad R = \int_0^a \frac{dy}{b+y} = \ln \frac{b+a}{b} \quad (107)$$

Since $S=1/R$, the upper bound shape factor is $S_u=1/\ln[(b+a)/b]$.

The lower bound shape factor is found by assuming that the lines in Figure 41(b) are insulated. The insulated strip is approximated by a slice of an annular ring. The shape factor can be found as follows:

$$dR = \frac{dr}{r\Delta\theta} \quad ; \quad \Delta R = \frac{1}{\Delta\theta} \ln \frac{r_o}{r_i} \Big|_{r_o}^{r_i} = \frac{1}{\Delta\theta} \ln \frac{r_o}{r_i} \quad (108)$$

$$\Delta S_l = \frac{1}{\Delta R} \quad ; \quad S_l = \int_0^{\frac{\pi}{4}} \frac{d\theta}{\ln \frac{r_o}{r_i}} = \frac{\pi}{4} \frac{1}{\ln \frac{b+a}{b}} \quad (109)$$

Table 11 displays results for S_u , S_l and the S found in the literature ($S=b/a+0.27$) (Kreith and Bohn, 1986). This table shows that S_u and S_l provide legitimate bounds for the shape factor. The quality, $\delta\bar{S}$, is defined as $(S_{\text{literature}} - S_l)/(S_u - S_l)$. At large λ , ($\lambda=b/a$), the upper bound provides a good approximation of the true shape factor value. This makes sense since at large λ , the isothermal lines are an accurate

Table 11 Comparison of Bounds to Approximate Actual Value (Literature) for Corner Geometry

$\lambda = b/a$	S_l	$S_{\text{literature}}$	S_u	$\delta\bar{S}$
0.25	0.49	0.52	0.62	0.26
0.50	1.71	0.77	0.91	0.30
1.0	1.14	1.27	1.45	0.43
2.0	1.94	2.27	2.47	0.63
4.0	3.52	4.27	4.48	0.78
8.0	6.65	8.27	8.50	0.88

description of the physical phenomenon. Conversely, at small λ , the lower bound provides a good approximation of the true shape factor value. This is expected since at large λ , the insulated lines are an accurate description of the actual heat flow. The upper bound for flow can now be found by letting $S=S_u$ and the lower bound for flow can be found by letting $S=S_l$ for $Q=2SK(T_2-T_1)$.

As mentioned before, the heat transfer shape factor can also be used for lubrication problems. The field equation for two plates separated by a constant gap, h , is the Laplace equation where the potential is the pressure, P . The solution to the (Poiseuille) flow for this problem can, therefore, take on the form $Q=KS(P_2-P_1)$ where $K=h^3/12\mu$. The shape factors S_u and S_l are the same here as in the heat transfer case.

This problem was solved using the FEM model presented in the model. The FEM model, however, assumed a linear pressure gradient at the boundaries which are insulated (no flow) in this study. The two conditions are essentially equivalent at $\lambda \geq 1$. When $\lambda < 1$, the linear pressure gradient boundary condition used in the FEM model is not a good approximation of the insulated boundary condition. For these cases, an average of the flow across the upper and lower boundary was used to represent the flow. Table 12 shows that S_{FEM} is bounded by S_l and S_u .

The flow calculated using S_u provides an upper bound to the true flow and S_l provides a lower bound. These upper and lower bound shape factors can be applied to other geometries encountered in lubrication. In Section 3.3.4 (Verification of

Table 12 Comparison of Bounds to FEM Model For V-lobe Geometry

λ	S_l	S_{FEM}	S_u
0.1	0.66	0.82	0.83
0.2	0.88	1.01	1.12
0.5	1.43	1.62	1.82
1.0	2.27	2.62	2.89
2.0	3.87	4.64	4.93
5.0	8.62	10.68	10.97
10.0	16.48	20.75	20.98

Equations Using Shape Factors) of this text, the shape factors were applied to the V-lobe geometry. Note that for the V-lobe, each of the lobe legs had a different height, h . The procedure is to define shape factors for each of the legs, calculate the flows for each leg, and then add the flows from each leg together. This procedure assumes that legs do not influence each other even though their height is different.

Shape factors can be also be used for any other phenomena where the Laplace equations is the governing differential equation and the boundary conditions are of the form used above. The bounds are useful because they supply analytical expressions to problems where a closed form solution does not exist. These expressions can be used for preliminary design calculations or optimization.

APPENDIX C

FEM CODE

PROGRAM flofem

C...THIS PROGRAM IMPLEMENTS A FINITE ELEMENT FORMULATION
 C...(BASED ON GALERKINS METHOD) TO SOLVE FOR THE PRESSURE
 C...FIELD IN A FLUID REGION GOVERNED BY THE STEADY,
 C...INCOMPRESSIBLE REYNOLDS EQUATION. RESULTING LOAD
 C...CARRYING CAPACITY AND FLOW ARE CALCULATED.

```

      IMPLICIT REAL*8(A-H,O-Z)
      DOUBLE PRECISION LNODS(180,3),COORDS(119,2),IXEDP(60)
      DOUBLE PRECISION SS(119,119),node(119)
      DOUBLE PRECISION R(119),ar(180),nbigc(80),nsmallic(80)
      DOUBLE PRECISION RS(119),P(119),PRESS(119)
      DOUBLE PRECISION A(3),B(3),C(3)
      REAL*8 HAVG3,K(3,3),kel(180,3,3)

```

```

C...legflo CONTAINS BOUNDARY INFO FOR CALCULATING V-LOBE FLOW
      open(1,file='legflo',status='unknown')
C...flopem.out CONTAINS THE RESULTING PRESSURES
      OPEN(2,FILE='flopem.out',STATUS='UNKNOWN')
C...noel CONTAINS THE NUMBER OF NODES AND ELEMENTS
      open(3,file='noel',status='unknown')
C...mf CONTAINS THE NUMBER OF NODES WITH BOUNDARY CONDITIONS
      open(4,file='mf',status='unknown')
C...geom CONTAINS GEOMETRIC VARIABLES FOR THE V-LOBE GEOMETRY
      open(8,file='geom',status='unknown')
C...mesh CONTAINS NODE COORDINATES AND ELEMENT NODE NUMBERS
      OPEN(7,FILE='mesh',STATUS='UNKNOWN')
C...bc CONTAINS BOUNDARY CONDITION NODES AND THEIR BOUNDARY
C      CONDITIONS
      OPEN(9,FILE='bc',STATUS='UNKNOWN')
      read(3,*) maxnod,maxnel
      read(4,*) maxfix,kbig,ksmall
      read(8,*) loben,tlobe,zl,sl
      write(2,882)loben,tlobe,zl
      write(6,882)loben,tlobe,zl
      NPERL=3
      MAXVAR=MAXNOD
      882  format(1x,'n = ',i1,'  delta = ',f5.3,'  L = ',f5.3)

C..INITIALIZE VECTORS AND MATRICES
      DO 2 I=1,MAXFIX

```

```

        IXEDP(I)=0.D0
2      CONTINUE
        DO 4 I=1,MAXVAR
          RS(I)=0.D0
          P(I)=0.D0
          R(I)=0.D0
          DO 3 J=I,MAXVAR
            SS(I,J)=0.D0
3          CONTINUE
4        CONTINUE

C...READ IN NODAL COORDINATES
        DO 12 NOD=1,MAXNOD
          READ(7,*) COORDS(NOD,1),COORDS(NOD,2)
12      CONTINUE

C...READ IN ELEMENT DEFINITIONS
        DO 11 NEL=1,MAXNEL
          READ(7,*) (LNODS(NEL,I),I=1,3)
11      CONTINUE

C...READ IN APPLIED LOADS AND FIXITIES
        DO 14 J=1,MAXFIX
          READ(9,*) IXEDP(J),PRESS(J)
14      CONTINUE

C...SET UP STRUCTURAL STIFFNESS MATRIX
        DO 100 NEL=1,MAXNEL

C...SET UP ELEMENT GEOMETRY AND ELEMENT STIFFNESS MATRIX
        NIC1=LNODS(NEL,1)
        NIC2=LNODS(NEL,2)
        NIC3=LNODS(NEL,3)
        X1=COORDS(NIC1,1)
        Y1=COORDS(NIC1,2)
        X2=COORDS(NIC2,1)
        Y2=COORDS(NIC2,2)
        X3=COORDS(NIC3,1)
        Y3=COORDS(NIC3,2)
        A(1)=X2*Y3-X3*Y2
        A(2)=X3*Y1-X1*Y3
        A(3)=X1*Y2-X2*Y1
        B(1)=Y2-Y3
        B(2)=Y3-Y1
        B(3)=Y1-Y2
        C(1)=X3-X2
        C(2)=X1-X3

```

```

C(3)=X2-X1
AREA=.5D0*(C(3)*B(2)-C(2)*B(3))
ar(nel)=area

```

C...DESCRIBE HEIGHT OF FLUID FIELD

```

C   HAVG=(3.0D0+EPS*(DCOS(X1)+DCOS(X2)+DCOS(X3)))/3.0D0
C   H1=(1.0D0+EPS*DCOS(X1))**3
C   H2=(1.0D0+EPS*DCOS(X2))**3
C   H3=(1.0D0+EPS*DCOS(X3))**3
C   HAVG3=(H1+H2+H3)/3.0D0
C   HAVG3=(1.0d0)**3
    IF(X1.LE.(s1+.00001d0)) then
      H1=120.0D-6
    ELSE
      H1= 20.0D-6
    ENDIF
    IF(X2.LE.(s1+.00001d0)) then
      H2=120.0D-6
    ELSE
      H2= 20.0D-6
    ENDIF
    IF(X3.LE.(s1+.00001d0)) then
      H3=120.0D-6
    ELSE
      H3= 20.0D-6
    ENDIF
    HAVG3=(H1**3+H2**3+H3**3)/3.0D0
    COEF=HAVG3/(AREA*4.0D0)
    DO 105 I=1,NPERL
    DO 106 J=1,NPERL
      K(I,J)=COEF*(B(I)*B(J)+C(I)*C(J))
      kel(nel,i,j)=k(i,j)
106  CONTINUE
105  CONTINUE

```

C...ADD IN ELEMENT STIFFNESS INTO STRUCTURAL MATRIX

```

    DO 50 I=1,NPERL
      ISTRST= LNODS(NEL,I)
      IELEMT=I
      DO 48 J=1,NPERL
        JSTRST= LNODS(NEL,J)
        JELEMT=J
        SS(ISTRST,JSTRST)=SS(ISTRST,JSTRST)+K(IELEMT,JELEMT)
48  CONTINUE
50  CONTINUE

```

C...COMPUTE LOADING VECTOR

```

        DO 60 I=1,NPERL
          R(I)= 0.0D0
60      CONTINUE

C...PUT LOADING VECTOR INTO STRUCTURAL LOADING VECTOR
        DO 62 I=1,NPERL
          IS=LNODS(NEL,I)
          RS(IS)=RS(IS) + R(I)
62      CONTINUE
100     CONTINUE

C...APPLY BOUNDARY CONDITIONS
        DO 750 J=1,MAXFIX
          IK=IXEDP(J)
          DO 901 I=1,MAXNOD
            SS(IK,I)=0.0D0
            RS(I)=RS(I)-SS(I,IK)*PRESS(J)
            SS(I,IK)=0.0D0
901     CONTINUE
          SS(IK,IK)=1.0D0
          RS(IK)=PRESS(J)
750     CONTINUE

C...SOLVE FOR PRESSURES

C...CARRY OUT GAUSSIAN REDUCTION
        M1=MAXNOD
        M2=M1-1
        DO 300 I=1,M2
          II=I+1
          DO 290 KK=II,M1
            FACT=SS(KK,I)/SS(I,I)
            DO 280 J=II,M1
              SS(KK,J)=SS(KK,J)-FACT*SS(I,J)
280     CONTINUE
            SS(KK,I)=0.0D0
            RS(KK)=RS(KK)-FACT*RS(I)
290     CONTINUE
300     CONTINUE

C...BACK SUBSTITUTE
        DO 400 I=1,M1
          II=M1-I+1
          PIVOT=SS(II,II)
          SS(II,II)=0.0D0
          DO 350 J=II,M1
            RS(II)=RS(II)-SS(II,J)*P(J)
350     CONTINUE

```

```

      P(II)=RS(II)/PIVOT
400  CONTINUE

C...PRINT RESULTING PRESSURES
c    write(6,*) ' node      pressure'
c    write(2,*) ' node      pressure'
      DO 888 I=1,MAXNOD
c    WRITE(6,*) I,P(I)
c    WRITE(2,854) I,P(I)
854  FORMAT(2X,I3,4X,F16.2)
      888 CONTINUE

c...CALCULATE LOAD CARRYING CAPACITY
      do 404 i=1,maxnel
        avgp=( p(lnods(i,1))+p(lnods(i,2))+p(lnods(i,3)) )/3.0d0
        force=avgp*ar(i) + force
404  continue
        write(2,*) ' force = ',force
        write(6,*) ' force = ',force

c...CALCULATE THE FLOW OVER SPECIFIED BOUNDARIES
      icum=0
762  DO 914 J=1,MAXFIX
        if(press(j).gt.101320) then
          icum=icum+1
          node(icum)=ixedp(j)
        endif
914  CONTINUE
      call flowq(icum,maxnel,maxnod,lnods,node,kel,p)

      nbig=0
      nsmall=0
      ktot=kbig+ksmall
      do 630 i=1,ktot
        read(1,*) ite,npq
        if(ite.eq.120) then
          nbig=nbig+1
          nbigc(nbig)=npq
        endif
        if(ite.eq.20) then
          nsmall=nsmall+1
          nsmallc(nsmall)=npq
        endif
630  continue
      call flowq(nbig,maxnel,maxnod,lnods,nbigc,kel,p)
      call flowq(nsmall,maxnel,maxnod,lnods,nsmallc,kel,p)

```

c...CALCULATE FLOW OVER ANY BOUNDARY

```

997  write(6,*)'input number of nodes for flow calculation:
,
      read(5,*) mcum
      if (mcum.eq.0) goto 999
      write(6,*)'input node numbers for flow calculation:  '
      read(5,*) (node(i),i=1,mcum)

      call flowq(mcum,maxnel,maxnod,lnods,node,kel,p)
      goto 997
999  end

```

C....SUBROUTINE FLOWQ CALCULATES THE FLOW OVER A BOUNDARY

C....SPECIFIED BY THE NODES ALONG THE BOUNDARY

```

      subroutine flowq(nqcum,maxnel,maxnod,lnods,node,kel,p)
      double precision lnods(180,3),node(119)
      double precision p(119),q(180,3),flow(119)
      real*8 kel(180,3,3)
      qcum=0.0d0
      qmls=0.0
      do 10 i=1,maxnod
         flow(i)=0.0d0
10      continue
         do 60 nq=1,nqcum
            do 20 mk=1,maxnel
               do 20 i=1,3
                  q(mk,i)=0.0d0
20          continue
                  do 50 mk=1,maxnel
                     do 50 jz=1,3
                        if(lnods(mk,jz).eq.node(nq)) then
                           do 40 i=1,3
                              do 40 j=1,3
                                 q(mk,i)=q(mk,i) + kel(mk,i,j)*p(lnods(mk,j))
40          continue
                                 flow(node(nq))=flow(node(nq))+q(mk,jz)
                                 qmls=flow(node(nq))*1.0d6
                                 endif
50          continue
                                 qcum=qcum+qmls
60          continue
                                 write(6,730)qcum
                                 write(2,730)qcum
                                 do 80 j=1,nqcum
c          write(6,770) node(j)
c          write(2,770) node(j)
770      format(59x,i3)
80          continue

```

```
c 730 format(2x,'Cumulative flow = ',f13.8,' ml/s    for the
c      &following nodes:')
      730 format(2x,'Cumulative flow = ',f13.8,' ml/s')
          write(6,*)
          write(2,*)
          END
```

BIBLIOGRAPHY

- Blech, J.J., Green, I. and Kopelman, J., 1986, "Transient Temperature Distribution in Partially Filled Rotating Horizontal Cylinders," ASME Journal of Applied Mechanics, Vol. 53, No. 2.
- Cook, R.D, Malkus, D.S., and Plesha, M.E., 1989, Concepts and Applications of Finite Element Analysis, 3rd ed., New York: John Wiley & Sons.
- Booker, J.F. and Huebner, K.H., 1972, "Application of Finite Element Methods to Lubrication: An Engineering Approach," ASME Journal of Lubrication Technology, Vol.94, No.4, pp.313-323.
- Etsion, I., 1984, "A New Concept of Zero-Leakage Noncontacting Mechanical Face Seal," ASME Journal of Tribology, Vol.106, No.3, pp.338-343.
- Etsion, I. and Yaier, R., 1988, "Performance Analysis of a New Concept Viscous Pump," ASME Journal of Tribology, Vol.110, No.1, pp.93-99.
- Green, I., 1989, class notes, ME6383 Lubrication, Georgia Institute of Technology, Atlanta, Georgia.
- Green, I., Mainland, M. and Etsion, I., 1989, "Experimental Investigation of a New Concept Viscous Pump", submitted for publication to ASME Journal of Tribology.
- Gross, W.A, ed., 1980, Fluid Film Lubrication, New York: John Wiley & Sons, pp. 57-65.
- Hasinger, S.H. and Kehrt, L.G., 1963, "Investigation of a Shear-Force Pump," ASME Journal of Engineering for Power, Vol.85, pp.201-207.
- Hsing, F.C., 1972, "Formulation of a Generalized Narrow Groove Theory for Spiral Grooved Viscous Pumps," ASME Journal of Lubrication Technology, Vol.94, No.1, pp.81-85.
- Hsing, F.C., 1974, "Analytical Solutions for Incompressible Spiral Groove Viscous Pumps," ASME Journal of Lubrication Technology, Vol.96, No.3, pp.365-369.

- Kreith, F. and Bohn, M.S., 1986, Principles of Heat Transfer, 4th ed., New York: Harper and Row Publishers, pp. 89-94
- Manning, F.E. and Key, W.E., 1990, "A Novel Test Rig for Development of Mechanical Face Seals for Use in Hard Abrasive Slurries," STLE preprint 90-AM-8A-2.
- Missimer, J.R. and Johnson, W.S., 1982, "Flow Between a Smooth Stationary Disk and Grooved Rotating Disk," ASME Journal of Lubrication Technology, Vol.104, pp.248-254.
- Reddi, M.M., 1969, "Finite-Element Solutions of the Incompressible Lubrication Problem," ASME Journal of Lubrication Technology, Vol.91, No.3, pp.524-533.
- Schlichting, H., 1968, Boundary Layer Theory, New York: McGraw-Hill Book Company, Inc.
- Shigley, J.E. and Mitchell, L.D., 1983, Mechanical Engineering Design, 4th ed. New York: McGraw-Hill Book Company, Inc., pp. 532-536.
- Sato, Y., Ono, K. and Moriguchi, N., 1988, "Analysis of Viscous Pumps With Shrouded Rayleigh-Steps Using Compressible Fluid," ASME paper 88-Trib-44.
- Vohr, J.H. and Pan, C.H.T., 1968, "Gas-Lubricated Spin-Axis Bearings for Gyroscopes," MTI-68TR29, Mechanical Technology Incorporated, Latham, New York.
- Walowit, Jed A. and Pinkus, O., 1982, "Analysis of Face Seals With Shrouded Pockets," ASME Journal of Lubrication Technology, Vol.104, pp.262-270.